Title

Exploring the electronic, vibrational, and chemical sensing properties of graphene, nanotubes, nanoparticles, and other nanomaterials

Author

Sussman, Allen

Publication Date

2013

Peer reviewed|Thesis/dissertation

Exploring the electronic, vibrational, and chemical sensing properties of graphene, nanotubes, nanoparticles, and other nanomaterials

by

Allen Sussman

A dissertation submitted in partial satisfaction of the

requirements for the degree of

Doctor of Philosophy

in

Physics

in the

Graduate Division

of the

University of California, Berkeley

Committee in charge:

Professor Alex Zettl, Chair

Professor Michael Crommie

Professor Roya Maboudian

Fall 2013

Abstract

Exploring the electronic, vibrational, and chemical sensing properties of graphene, nanotubes, nanoparticles, and other nanomaterials

by

Allen Sussman

Doctor of Philosophy in Physics

University of California, Berkeley

Professor Alex Zettl, Chair

Some might view the "nano revolution" as one of the most important developments of our time, as nanomaterials have been and continue to be a seemingly endless source of new and exciting physics and have found application in almost every imaginable aspect of our lives. Carbon allotropes such as graphene, which is a single atomic layer of carbon atoms in a hexagonal lattice, carbon nanotubes (CNTs), which can be thought of as graphene sheets rolled up into cylinders, and graphene nanoribbons (GNRs) have garnered massive attention in recent years due to their remarkable properties and many potential uses. This work investigates the fundamental properties and applications of certain nanomaterials such as carbon allotropes, semiconducting metal oxide (SMO) nanoparticles, and others in the exciting fields of gas sensing, nanoelectromechanical oscillation, and optical near field enhancement. It also introduces a novel GNR synthesis technique.

Chapter 1 of this work is a brief introduction to the nanomaterials that will be investigated here. Chapter 2 presents experimental investigations into the interaction between gases and certain nanomaterials, including SMO nanoparticles, gold nanowires and thin films, CNTs, bare graphene, and graphene functionalized by a novel electrodeposition technique. New findings on the sensing mechanism of tungsten oxide nanoparticles for hydrogen sulfide gas are discussed. These findings suggest that previous models were incorrect or incomplete. Chapter 3 discusses sustained self-oscillations of a singly-clamped CNT under constant bias, a phenomenon which obviates the need for large external sources to drive nanomechanical oscillations. A model of the phenomenon is presented and used to guide scalable, top-down fabrication of self-oscillators. In chapter 4, a novel, clean technique for synthesizing GNRs with desired dimensions is demonstrated. It is shown that this method allows for transmission electron microscopy and electronic characterization of the GNRs during and after synthesis. A model of the underlying physical mechanism is proposed. In chapter 5, optical field enhancement near nanostructures, which has applications in optical antennae, photovoltaics, and near field optical microscopy, is modeled.

To Mom and Dad

Contents

List of Figures

Acknowledgments

First and foremost, I'd like to thank my advisor, Prof. Alex Zettl, for believing in a young graduate student with little experimental experience, and giving him the opportunity to work in world-class research facilities with co-workers of the highest caliber. To be able to study the natural world in this institution of unparalleled quality has been an unbelievable gift, and I owe it to you.

To Prof. Roya Maboudian, thank you for fostering great collaborations between members of your group and myself, and for serving on my qualifier and thesis committees. To Prof. Mike Crommie, thank you for chairing my qualifying exam and being a member of my thesis committee. Thanks also to Prof. Steven Louie for serving on my qualifying exam committee and for your amazing teaching, which accomplished the extraordinary task of making the incredibly complex seem simple.

Thank you to Dr. Willi Mickelson for the tremendous amount of guidance you've given me during my time in graduate school, despite your many other obligations. Big thanks to Dr. Qin Zhou, my most frequent collaborator, for your wit, incisive critiques, reliability, for being a team player, for knowing your stuff, for your crazy fab skills, and for good times at conferences. Thanks to my undergrads, Dennis Wang, Norman Wen, Andrew Siordia, and Jeffrey Dong, for all your help and for teaching me how to be a better mentor and communicator. To Benji Aleman, thank you for taking me under your wing during my early days in the lab, despite your busy life. Infectiously silly, unrealistically optimistic but highly effective, and full of vitality, curiosity, integrity, and compassion, there are few people I respect more. To Will Regan, my old desk neighbor, thanks for help and guidance, for being an ear, for many laughs, and for endless cat videos. To Will Gannett, thanks for certifying and advising me on half the equipment in the lab and for your quick wit. To Dr. Matthias Loster, thanks for your guidance early on. Thanks to Dr. Carlo Carraro for patiently helping with my XPS experiments. Thanks to Kwanpyo Kim and Dr. Albert Gutes for the good collaborations. Thanks, too, to everyone in my group for all their help, insightful conversation, and for fun times.

Thanks to Gee Gee Lang for dealing with miles of red tape and juggling a million tasks while maintaining availability and a great attitude. Thanks to Anne Takizawa and Donna Sakima, my makeshift physics moms, for dealing with all department-level issues, for always being available to talk, for genuinely caring, for their smiles and hard work.

Thanks also to the Center of Integrated Nanomechanical Systems, which is funded by the National Science Foundation, for supporting a large portion of my graduate work.

Thanks to Prof. Mike DeWeese for his patience and guidance in helping a new Ph.D. student start his graduate research career. Thanks to Mr. Esper, my high school AP Physics C teacher, who believed that high school seniors could be taught college honors-level introductory physics. The high level and rigor of your class

inspired me to become a physics major. Enjoy your retirement, you deserve it! Special thanks to Prof. Rich Galik, my undergraduate advisor, one of the brightest and most kind-hearted people I've ever met. The world has lost a paragon of human excellence.

I must acknowledge Tarzan, my partner in crime, Asher, my old friend, and A.N., for being a rock and believing in me in hard times.

Most of all, thank you to my parents, without whom I would simply not exist, for your endless love and support. Dad: thank you for introducing me to and developing my love of critical thinking and problem solving and always expressing your pride in me. Mom: thank you for always pushing me to be better. I love you both dearly.

Last but not least, thank you, the reader, for your attention. I hope this work serves as an interesting and useful look into the exciting world of nanomaterials.

Chapter 1

Introduction

As scientists began to study materials with smaller and smaller dimensions, they found that at the nanoscale, a host of new and amazing properties appeared. Even today, we continue to make new, exciting discoveries about nanoscale phenomena. These phenomena are extremely interesting in themselves, but they are also important because they give nanomaterials distinct advantages which have led to applications in almost every technological field. For example, graphene, a one-atom-thick sheet of sp^2-bonded carbon, has totally unique mechanical and electrical properties, which make it the strongest material ever studied,[108] with the highest room-temperature electrical conductivity.[15] This work describes investigations into the unique properties of nanomaterials, their ability to surpass current technology in certain applications, and new synthesis methods which allow for more studies.

This chapter is divided into three sections. The first summarizes the main properties of the carbon-based nanomaterials which will be investigated, the second discusses semiconducting metal oxides, and the third briefly outlines this work.

1.1 Carbon-Based Nanomaterials

Graphene (Fig. 1.1, top) can be considered the "mother" of all carbon-based nanomaterials. It is a one-atom-thick sheet of carbon atoms in a honeycomb lattice (Fig. 1.1, top). The carbon atoms form sp^2-hybridized orbitals. Graphite is composed of many layers of graphene. Graphene's band structure is shown in Fig. 1.2. It is a zero-bandgap semiconductor and near the Fermi level it has a linear dispersion relation, which means its carriers act as relativistic particles known as massless Dirac fermions.[146] Though graphene had been studied theoretically for over 60 years, it was not isolated until 2004.[147] Geim and Novoselov, who originally isolated it, went on to win the Nobel Prize in 2010.

Graphene has a number of amazing properties. At single-atom thickness, it is the thinnest possible material. Since every atom is on its surface, it has the highest

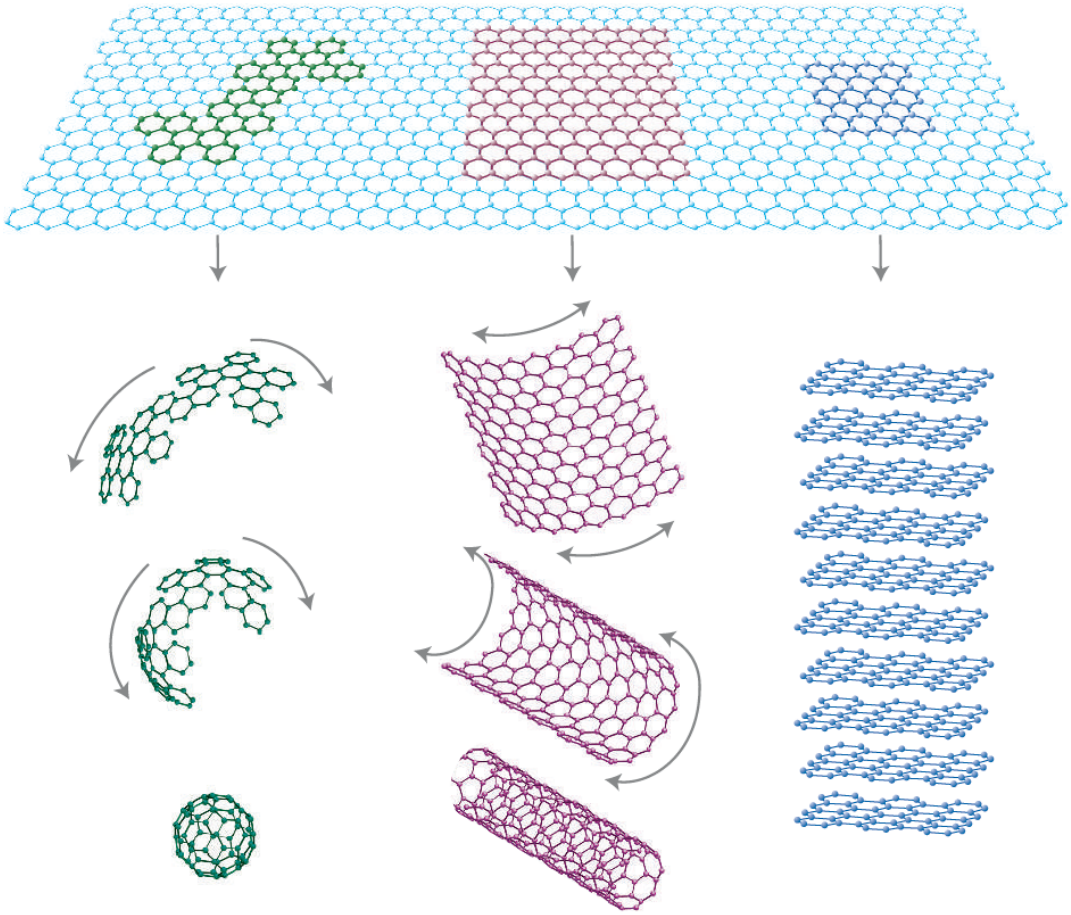

Figure 1.1: Carbon allotropes. (From [53])

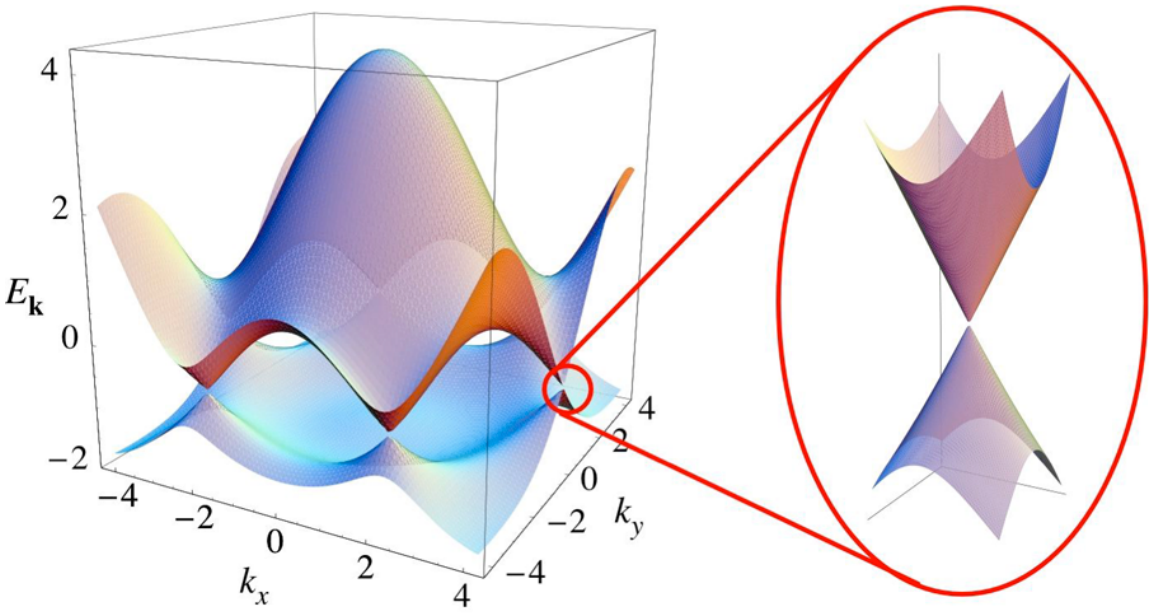

Figure 1.2: Graphene's band structure. (From [24])

possible surface-to-volume ratio. Due to its amazing electronic properties, it has the lowest recorded electrical resistivity at room temperature (10^6 Ωcm), highest current density at room temperature, and the highest room temperature mobility (200,000 $cm^2V^{-1}s^{-1}$).[15] Due to the robustness of its C-C bonds, it is the strongest and stiffest material ever studied, with a breaking strength that reaches the theoretical limit (40 N/m), and a Young's modulus reaching 1 TPa.[108] It has record thermal conductivity.[6] Since it is only an atomic monolayer, it has high optical transparency, adsorbing 2.3% of white light.[142] On the other hand, given that it is only a monolayer, this is remarkable highly adsorption. It also displays amazing behavior, including a negative thermal expansion coefficient,[8] conductivity in the limit of no carriers,[146] and an integer quantum Hall effect where the Hall conductivity plateaus are shifted by a half-integer.[207] As mentioned earlier, carriers in graphene act as massless Dirac fermions, and there has been much interest in using graphene as a platform for probing the behavior of such relativistic particles.

Graphene nanoribbons (GNRs) are thin strips of graphene, with widths on the nanoscale (Fig. 1.1, right). They are predicted to have many of graphene's unique properties, but in many cases their width causes a band gap to open up, allowing for application as semiconductors. Theoretical studies have largely treated the properties of zigzag or armchair nanoribbons (see Fig. 1.3) and have shown that the properties of the nanoribbons depend strongly on edge structure. It has been generally predicted that armchair nanoribbons are semiconducting.[173, 201] In the nonmagnetic approximation, zigzag nanoribbons are metallic, but if considering spin, zigzag

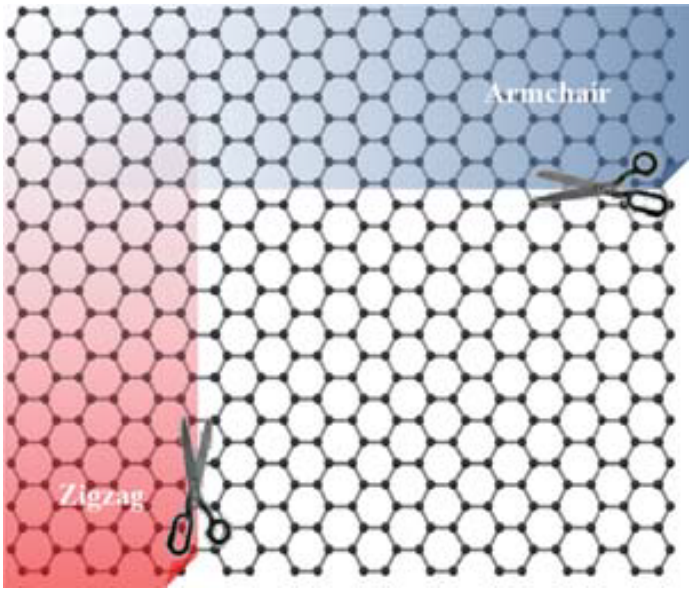

Figure 1.3: The theoretical cutting pattern which would create zigzag and armchair graphene nanoribbons. (From [43])

nanoribbons in their ground state have ferromagnetic coupling along each edge and antiferromagnetic coupling between edges and nearest neighbors.[50, 110, 149] Studies predict that if an electric field is applied along the cross ribbon width direction to a zigzag nanoribbon in its ground state, the amazing property of half-metallicity emerges, in which one spin channel is semiconducting and the other metallic.

Carbon nanotubes (CNTs) can be thought of as graphene which has been rolled up into cylinders (see Fig. 1.1, middle). They have been measured with aspect ratios higher than any other material (132,000,000:1),[192] diameters as small as 0.4 nm[155] and lengths as large as 18 cm (not simultaneously). Single-walled CNTs (SWCNTs) consist of one cylinder and multi-walled CNTs (MWCNTs) consist of many concentric cylinders. Depending on their chirality (e.g. how they are "rolled up"), SWCNTs can be semiconducting (with different band gaps) or metallic.[187] In MWCNTs, one of the individual tubes is usually metallic and the whole tube is therefore usually metallic. CNTs have extremely high strength[197] and stiffness[198] comparable to that of graphene. Individual shells can exhibit almost frictionless telescoping behavior, sliding between each other with ease. Thermal conductivity along the axis is second only to graphene, but due to quantum confinement, conductivity is extremely low perpendicular to the axis.[171] Due to CNTs' nanoscale diameter, they act as 1-D wires, with quantized limits on electrical[25] and thermal[165] conductance.

1.2 Semiconducting Metal Oxides

Semiconducting metal oxides are metal oxides with semiconducting behavior. This work explores the properties of a few semiconducting metal oxides, including tungsten oxide (WO_3), zinc oxide (ZnO), maghemite (γ-Fe_2O_3), and indium oxide (In_2O_3).

Tungsten oxide (WO_3) is found as a yellow powder in bulk form. Its hydrates occur naturally but rarely; most WO_3 is an intermediate in the production of tungsten from tungsten ores.[152] Techniques for synthesis of WO_3 began to be studied in the 17th century.[38] It is electrochromic and its crystal structure is temperature dependent, being triclinic from -50 to 170°C, monoclinic from 17 to 330°C (with an indirect bandgap of around 3 eV), orthorhombic from 330 to 740°C, and tetragonal above 740°C.[106, 160] It has many applications including electrochromic devices like smart windows,[60, 59, 67] gas sensors,[84, 118, 158] and pigments.[152]

Zinc oxide (ZnO) is an ionic crystal usually in the hexagonal wurzite structure, naturally n-type, and has a wide, direct bandgap of 3.3 eV. It has a number of interesting and useful properties, including high electron mobility, large heat capacity, high thermal conductivity, low thermal expansion, high melting temperature, high refractive index, strong room-temperature luminescence, thermochromicity, piezoelectricity, pyroelectricity, and deodorizing and antibacterial properties. It has been used for millenia in medicinal ointments and as a pigment in paints. Today it is largely used in rubber and ceramics production, but continues to be used in paint, ointments, and many other applications.[151, 193] Zinc oxide nanostructures have current and potential applications in UV protection, anti-bacterial agents,[161] field emission,[109] transparent electronics,[143, 164] sensing,[144, 159] and piezoelectric energy storage.[194]

Maghemite is an iron oxide, also known as γ-Fe_2O_3. It is cubic or tetrahedral[179] and occurs naturally in soil as yellow pi‘gment which is a weathering product of magnetite (Fe_3O_4) or as a product of heating other iron oxides. At approximately 400°C, it makes a transition to hematite (α-Fe_2O_3). Maghemite is ferrimagnetic at room temperature,[41] but particles under 10 nm in size are superparamagnetic[145] and aggregates can be superferromagnetic.[35] Nanoparticles can be synthesized in a number of different ways. Due to their magnetic properties and stability, maghemite particles are commonly used for recording and data storage.[169] They have received attention for biomedical applications such as drug delivery, due to their biocompatibility and superparamagnetism.[125, 145, 178] They are also frequently used as pigments because they are chemically resistant and can display a large range of colors.[104] They are used as catalysts and have been researched for their gas sensing properties.[83, 177, 191]

Indium Oxide (In_2O_3) is found as a yellow powder in bulk form,[128] has a band gap of around 3 eV,[95, 188] and a cubic crystal structure.[126] Indium compounds can be heated to form bulk indium oxide. Nanostructured indium oxide has been syn-

thesized by CVD,[202] hydro-thermal synthesis,[199, 200] and laser ablation.[1, 111] Indium oxide has found use as diffusion barriers,[98, 99] infrared mirrors, antireflective coatings, transparent electrodes,[105, 140, 185] and gas sensors,[11, 76, 176] among other applications.

1.3 Outline of this Work

This thesis is divided into four chapters. Each chapter explores different interesting studies in the phenomena, synthesis, and applications of nanomaterials.

Chapter 2 explores the nature of interactions between gases and nanomaterials. I discuss studies on bare and functionalized graphene, CNTs, SMOs, and various gold morphologies, including a revision of the commonly-held theory of the interaction of WO_3 and hydrogen sulfide.

In chapter 3, I introduce the newly-discovered phenomenon of sustained self-oscillations in CNTs, which allows for NEMS oscillations without the need for large external driving sources. I discuss the phenomenon's discovery and a model describing it. Guided by the model, scalable fabrication of CNT oscillators with desired qualities was performed, showing the model's correctness and that the fabrication of CNT self-oscillators is scalable.

Chapter 4 discusses a new, clean synthesis method for GNRs from CNTs which allows for TEM and transport characterization during and after the synthesis process, and a model describing it. The method involves driving current through a CNT in a TEM, causing electrical breakdown of the CNT along one side.

The enhancement of optical fields near nanostructures is explored in chapter 5. Specifically, I model the optical fields near silicon nanowires on and off resonance, showing that extremely large enhancement occurs during resonance. Such phenomena can be exploited in photovoltaics, LEDs, and optical microscopy.

Chapter 2

Effect of Gases on the Properties of Nanomaterials

2.1 Introduction

Work in this chapter was largely performed in collaboration with Dr. William Mickelson and Dr. Qin Zhou, with help from Dr. Jianhao Chen, Jeffrey Dong, Dennis Wang, Norman Wen, and Andrew Siordia.

Chemical sensors are of vital importance in modern society. Community gas monitors, for example, make sure the levels of various harmful (e.g. toxic, flammable, etc.) gases are within an acceptable range these monitors are especially necessary near industrial processes which produce such gases (e.g. oil and natural gas refining, landfills) and natural processes (e.g. swamps) but are also critical in detecting gas leaks and potential terrorist attacks, among other things. Sensors in our drinking water supply are obviously also essential in ensuring public safety. Personal monitoring equipment is crucial for workers in one of the many industries in which a colorless, odorless gas leak or large buildup of gases could spell doom for workers in contact with the gas, and perhaps others in the case of explosive gases.[7, 61, 103]

The three main types of gas sensors in use today are photoluminescent, electrochemical, and semiconducting metal oxide (SMO)-based. Sensors which operate on the principle of photoluminescence contain a light source which only emits light at a characteristic wavelength of the analyte to be detected.[102] If the analyte is present, it absorbs a portion of the light, decreasing the signal at the light detector. Photoluminescence-based sensors are an old, proven, versatile technology with low detection limits but are large, costly, and high-power, which, besides being general downsides, make them insufficient for large-scale use as personal monitors for industrial workers. Electrochemical sensors are electrochemical cells in which the working electrode is composed of a material which catalyzes a redox reaction of the analyte. When the analyte comes in contact with the working electrode, a redox reaction occurs, changing the potential of the electrode and thus driving a current. Due to

the lack of specificity of the sensing mechanism, electrochemical sensors often suffer from cross-sensitivity. Due to the use of an electrolyte, electrochemical sensors often suffer from sensitivity to temperature and humidity fluctuations. Also, the catalyst is used up over time, so the lifetime of electrochemical sensors is limited.[100]

SMO sensors are chemiresistive sensors in which SMOs (e.g. ZnO, SnO_2, WO_3, etc.) act as the sensing material. In ambient air, oxygen molecules or ions adsorb at the grain boundaries of SMOs. In the case of n-type SMOs, the adsorbed oxygen pulls electrons from the bulk, resulting in a depletion region near the grain boundary. Depending on the SMO used, when certain analytes are present they will adsorb on the grain boundary, either decreasing the width of this depletion layer and/or donating electrons to the bulk, both of which increase the conductance of the sensor. The specific mechanism by which the depletion width is changed or charge is donated depends on the type of metal-oxide and analyte.[97, 70]

SMO sensors have been the subject of much interest in recent years, as their performance can and has been improved significantly by shrinking their design down to the nanoscale. SMO sensors, for example, generally require temperatures in the hundreds of degrees Celsius to operate, and thus were relatively high-power. (A beneficial side-effect of their high-temperature operation is insensitivity to temperature fluctuation.) By shrinking the sensor down and using a low-power microhotplate, my colleagues and I operated such a device at less than 10 mW.[132] Decreasing the form factor can also be viewed as increasing response and recovery time for the same power usage (because this will result in a higher temperature).[23, 33, 46] Making the thickness of the sensor nanoscale decreases or effectively eliminates gas diffusion time, thus increasing response and recovery time. Using thin films, nanoparticles, or other nanoscale morphologies effectively reduces the grain boundary size, which increases the surface-to-bulk ratio, and thus increases sensitivity and/or lowers power usage. The small form factor and potential versatility of manufacturing methods, while improvements in themselves, also allow for simple multiplexing of different gas sensors, which can eliminate cross-sensitivities and allow for sensing of multiple analytes, on a single chip small enough to fit in a convenient personal monitoring device, such as a badge or card.[57, 117]

In addition, there has been much interest in various other kinds of nanostructures as gas sensors. Graphene and carbon nanotubes have recently been exciting prospects for gas sensing because all their atoms are exposed to the environment, they possess high carrier mobilities, are low noise, and have high quality crystal lattices, which makes their properties easier to model and to controllably modify through defect creation and functionalization.[122]

In order to effectively create and improve upon gas sensor designs, we must have a good understanding of the way in which gases interact with nanostructured materials. Despite their importance, much is still not known about the way in which this occurs. In SMO gas sensors, for example, there is still significant debate about the exact sensing mechanisms. The mainstream sensing mechanism is described above.

However, other sensing mechanisms have been proposed. Gurlo & Riedel,[63] for example, have claimed that there is no convincing evidence that oxygen ionosorption as described in the mainstream sensing mechanism actually occurs. They proposed that sensing responses are due to reduction of surface oxygen vacancies by reducing gases and re-oxidation by ambient oxygen. In addition, though the sensing mechanism described above is the most common dominant mechanism, other mechanisms dominate for certain gases and are often debated. The sensing mechanism of CO, for example, has been debated. Some claim that it is due to the main mechanism described above. Others claim it is due to reaction of CO with surface hydroxyl groups, producing atomic hydrogen which reacts with surface lattice oxygen to free electrons. Still others have proposed that it is due to direct absorption of CO^+.[34]

Additionally, understanding the effect of the presence of gases on nanomaterials improves our understanding of them in a more general sense. What types of molecules adsorb, and what compounds form, at the surface of nanomaterials in ambient air? What surface states form and what role do they play in the electronic properties of the nanomaterial? How does nanomaterial behavior change as the gaseous environment changes (humidity levels, for example, change significantly in ambient air)? All these questions and many others can be probed via exposure to gases, and all are important for the understanding of nanomaterials and fabrication of nanomaterials-based devices.

2.2 Theory of Interaction of Gases and Solids

This treatment is largely based on those in the chapter "Adsorption Phenomena" in Lalauze's *Chemical Sensors and Biosensors*[103] and the chapter "Electrical-Based Gas Sensing" in *Solid State Gas Sensing* by Comini et al.[34]

When a gas molecule comes in contact with a solid, there are two possible effects: the gas molecule adsorbs, which is a reversible reaction; the gas molecule adsorbs and creates a new compound on the solid surface, which is a non-reversible reaction. Adsorption can be further characterized as either physisorption or chemisorption. In physisorption, the gas molecule is bound to the solid with no electron exchange. Chemisorption involves electron transfer.

2.2.1 Interaction between Atoms or Molecules

The interaction between atoms or molecules is most simply approximated by the Leonard Jones Potential

$$\phi = \phi_0[2(\frac{r_0}{r})^6 - (\frac{r_0}{r})^{12}] \tag{2.1}$$

where the potential has a minimum at r_0 of value ϕ_0. The first term the attractive, long-range Van Der Waals term which is combination of three phenomena: Keesom's

potential, which only applies to molecules which have a permanent dipole moment, and originates from the attraction between the molecules' permanent dipoles; Debye's induction potential, the attraction between one molecule's permanent dipole moment and other's induced dipole moment; and London's dispersion potential, which comes from the molecules' instantaneous induced dipole moments. The third effect is often the most important. The second term is a result of the exchange force between the electron clouds and has been found empirically to be well-approximated by a r^{-12} term.

2.2.2 Interaction between Molecule and Solid

Imagine a crystal with N molecule per unit volume which extends infinitely in the x and y directions, ends at $z = 0$, and extends infinitely in the $-z$ direction. Imagine that there is a gas molecule at $z = Z$. If we assume this gas molecule interacts with every molecule in the solid by the Leonard Jones Potential, we can integrate the terms in (2.1) to find that the total attractive and repulsive potentials between the gas molecule and the solid are:

$$\Phi_a = \frac{\pi N \phi_0 r_0^6}{3Z^3} \tag{2.2}$$

$$\Phi_r = -\frac{\pi N \phi_0 r_0^{12}}{45Z^9} \tag{2.3}$$

2.2.3 Physisorption vs. Chemisorption

The potential that a physisorbed and a chemisorbed molecule see near the surface of a solid is shown in Fig. 2.2.3a. In the chemisorbed case, the molecule has already been giving a certain energy E_{dis} to dissociate the molecule into its constituents. We see that in physisorption the binding potential is significantly less than in chemisorption (1 Joule/mole instead of 5-6) and the equilibrium position is further out.

Adsorption proceeds from physisorption to chemisorption since after the molecule physisorbs, the energy E_a that is required to dissociate the molecule is smaller than E_{dis}, the energy required to dissociate the molecule if physisorption has not occurred.

Physisorption is a non-activated slightly exothermic process characterized by high coverage θ at low temperature and low coverage at high temperature. If the partial pressure is very low, Henry's Law applies and the amount physisorbed is simply proportional to the partial pressure.

Chemisorption and desorption require an energy $E_d = Q_{chem} + E_a$, so in contrast to physisorption, which is an inactivated process, chemisorption is an activated process. The activation energy can be supplied either thermally or by a non-equilibrium process such as illumination.

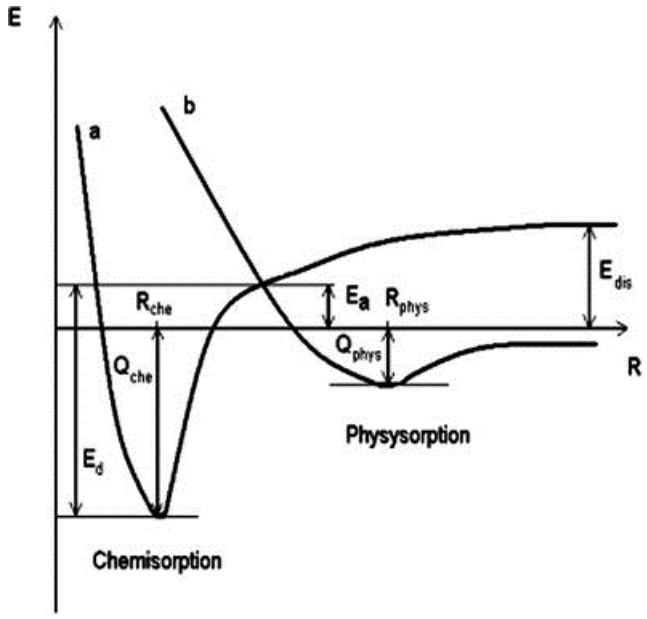

Figure 2.1: The potential between a gas molecule and a solid in the cases of physi- and chemisorption. (From [34])

2.2.4 Hill's Model of Physisorption

Experimentally, it has been found that the number of adsorbed molecules is a function of only pressure and temperature. This is a condition that all models should satisfy.

In 1946, Terrell L. Hill created the Hill equation for adsorption

$$\frac{p}{p_0} = \frac{1}{C}\frac{\theta}{1-\theta}exp(\frac{\theta}{1-\theta} - \alpha\theta) \tag{2.4}$$

where p is the vapor pressure of the adsorbed gas, p_0 is the gas pressure, C is a constant, and θ is the ratio of the total quantity of gas adsorbed to the monolayer adsorbed gas quantity.

2.2.5 Adsorbate Mobility

One can imagine two extremes of adsorbate mobility: complete mobility or localization at surface sites. These two extremes are related to the nature of the elements composing the solid. One simple model is that the surface sites alternate between lower energy E_1 and higher energy E_2. The difference between these two energies is the energy barrier for a molecule to move from the lower energy to the higher energy surface site. If $kT \gg E_2 - E1$, the layer is mobile, and if $kT \ll E_2 - E1$, the layer is localized.

2.2.6 Physisorption Isotherms in Mobile Monolayers

Hill assumed a perfectly mobile monolayer in his model, and we can therefore take the isotherm equation direct from his model

$$n_s = \alpha P \tag{2.5}$$

Note that this does not account for interaction between adsorbed molecules. In fact, the adsorbates are usually dilute enough that the thermodynamic models do not have to be used.

2.2.7 Physisorption Isotherms in Localized Monolayers

Assuming the surface is composed of identical and active surface sites, we can derive the Langmuir isotherm

$$\theta = \frac{KP}{1 + KP} \tag{2.6}$$

where θ is the fractional coverage of adsorbed molecules, P is pressure and K is the rate of adsorption given by

$$K = K_0 exp(-\frac{\Delta H^0}{RT}) \tag{2.7}$$

We can derive this equation is a slightly different way which can give us more insight into the phenomenon. Say adsorption occurs at a rate of V_F and desorption occurs at rate V_D.

V_F is proportional to the rate at which gas molecules impact the surface, υ, and number of unoccupied surface sites

$$V_F = \alpha \upsilon (1 - \theta) \tag{2.8}$$

Now

$$\upsilon = \frac{P}{\sqrt{2\pi m k T}} \tag{2.9}$$

Plugging this into (2.8),

$$V_F = \alpha' P (1 - \theta) \tag{2.10}$$

Meanwhile, V_D is proportional to the number of adsorbed molecules

$$V_D = \beta \theta \tag{2.11}$$

In equilibrium, $V_F = V_D$, so again we derive the Langmuir isotherm

$$\theta = \frac{KP}{1+KP} \tag{2.12}$$

this time with

$$K = \frac{\alpha'}{\beta} \tag{2.13}$$

2.2.8 Chemisorption Isotherms

In the case of chemisorption, adsorption heat varies with degree of coverage, so the Langmuir isotherm no longer applies. Coverage turns out to be given by the Temkin isotherm

$$\theta = (\frac{RT}{\Delta H_0 \beta}) \ln AP \tag{2.14}$$

where β and A are constants.

Chemisorption can be thought of as a combination of two phenomena: physisorption followed by electron transfer, during which time the molecule chemisorbs. In the case of adsorption, only the second stage has an activation energy and it is therefore the second stage which controls the kinetic process (see 2.2.3). As for desorption, both phenomena are activated, but the chemisorption again controls the kinetic process because its activation is much larger.

The net rate of chemisorption is given by

$$\frac{d\theta}{dt} = k_{ads} \exp(-\frac{E_a}{kT}) - k_{des}\theta \exp(-\frac{E_a + \Delta H_{chem}}{kT}) \tag{2.15}$$

At equilibrium,

$$\theta = \frac{k_{ads}}{k_{des}} \exp(\frac{\Delta H_{chem}}{kT}) \tag{2.16}$$

And θ decreases rapidly with increasing temperature

It turns out that heat of adsorption ΔH_{chem} decreases with coverage mainly because of heterogeneity of the surface – high energy sites will be occupied first and low-energy ones later. Activation energy E_a can be regarded as the difference in the electrochemical potential between the surface and the adsorbed molecule and therefore changes with coverage, as electrons are donated or accepted and the number of electrons on the surface changes.

The adsorption isobar, that is the volume adsorbed as a function of temperature at a constant pressure, is characterized at low temperature by physisorption and at high temperature by equilibrium chemisorption that decreases exponentially with temperature. In the intermediate region irreversible chemisorption takes place since the first term of (2.15) dominates.

2.2.9 Chemisorption of Diatomic Molecules

To model the chemisorption of a diatomic molecule X_2, we can divide the process into two stages: (a) the dissociation of the molecule into its constituent X ions and (b) electron transfer between those ions and the solid. In the first process,

$$K_1 = \frac{P_X^2}{P_{X_2}} \tag{2.17}$$

In the second process, we can solve the Langmuir isotherm to get

$$K_2 = \frac{\theta}{P_X(1-\theta)} \tag{2.18}$$

Combining these and solving for θ,

$$\theta = \frac{K_1\sqrt{K_1 P_{X_2}}}{1+\sqrt{K_1 P_{X_2}}} \tag{2.19}$$

2.2.10 Adsorption of Multiple Gases

Consider gases A and B. The fraction of sites available for binding is

$$1 - \theta_A - \theta_B \tag{2.20}$$

Going through the same derivation as for the Langmuir isotherm, we now find

$$K_A = \frac{\theta_A}{P_A(1-\theta_A-\theta_B)} \tag{2.21}$$

and

$$K_B = \frac{\theta_B}{P_B(1-\theta_A-\theta_B)} \tag{2.22}$$

Combining these, and solving for θ_A and θ_B, we find

$$\theta_A = \frac{K_A P_A}{1 - K_A P_A - K_B P_B} \tag{2.23}$$

and of course

$$\theta_B = \frac{K_B P_B}{1 - K_A P_A - K_B P_B} \tag{2.24}$$

Generally for a number of gases,

$$\theta_i = \frac{K_i P_i}{1 - \sum_{i=0}^{N} K_i P_i} \tag{2.25}$$

2.3 Gas Delivery System

To understand how the presence of gases affects the electronic properties of nanomaterials, we expose various nanomaterials to gases while monitoring their electronic characteristics.

Electrical control and measurement of the devices was achieved in the following way: Nanomaterials were deposited onto chips by various methods which will be described for each individual nanomaterial. Electrodes were patterned before or after deposition, and were wirebonded to the leads of a package (Fig. 2.2a). Often the gate of the chip was electrically connected to the floor of the package by means of silver paint, and the floor of the package was then also wirebonded to a lead. This allowed for gating of the device. These leads were then electrically connected (Fig. 2.2a and b) to a Keithley 2602A SourceMeter, which could then simultaneously control and measure the electrical characteristics of the material.

A number of gases were delivered to these devices. One was house air, which was dried by means of a pressure-swing absorption drier, and filtered through multiple filters. Hydrocarbons were also removed by means of a charcoal scrubber. Others gases came from cylinders and were often balanced in nitrogen. These gases could be mixed with each other and the house air (by a number of mass flow controllers (MFCs) to produce gas mixes of certain concentrations.

The gases were often humidified. When humidifying, deionized water flowed from a pressurized tank to a liquid flow controller (LFC) to a controlled evaporator mixer (CEM) which evaporated the water and mixed it with a gas stream to a specified humidity level.

There were multiple gas streams, each with its own concentrations of two different analytes, and each with its own humidity level. Valves determined which stream(s) were delivered to the sample and which to the exhaust. The existence of multiple streams allowed one to deliver a stream with certain properties to the device, meanwhile "priming" the other stream by setting it to the desired concentration and humidity level. Then when one switched streams, one could switch directly from the conditions in stream A to the conditions in stream B. (If one only used one stream, there would be a certain "lag" time, during which dead space in the lines was flushed.) See Fig. 2.3 for pictures of the gas delivery system.

A manifold was then screwed onto the sample (with a gasket between the sample and manifold), with an gas inlet and outlet above the device. The desired gas was delivered to the sample through the gas inlet. This provided good isolation from ambient air while delivering the desired gas to the sample.

LabVIEW was used to control and measure gas delivery. One LabVIEW program interfaced with the MFCs, LFCs, CEMs, and valves (Fig. 2.4). A user could input into this program the desired concentrations, humidity level, and flow rate of each stream, and which stream(s) were delivered to the sample. A user could also write "gas profiles," instructions to configure the streams in a certain way (i.e. concentra-

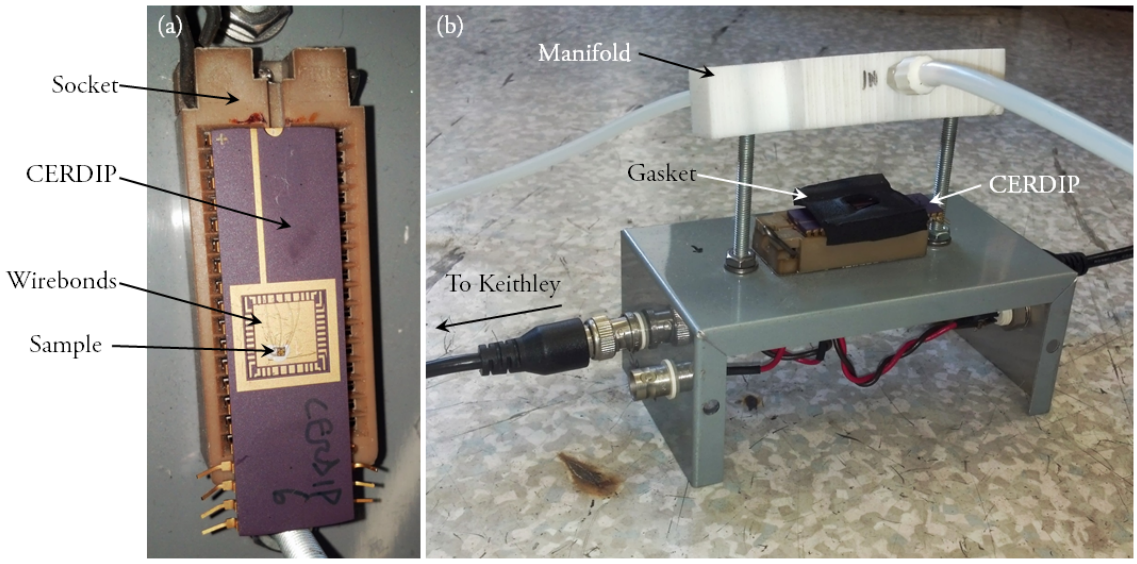

Figure 2.2: Pictures of one of the schemes used to electronically characterize a device while delivering gas to it. (a) A device on a CERamic Dual-Inline Package (CERDIP). The device is affixed by silver paint and wirebonded to pads on the CERDIP, each of which is electrically connected to a pin of the CERDIP. The CERDIP is inserted into a socket, and (b) wires have the been soldered between the pins of the socket and coaxial connectors, allowing for electrical characterization of the device. When in operation the manifold shown lies on the gasket. The gas input shown flows out of a small hole above the sample, exposing the sample, and then is removed through an adjacent hole in the manifold. Other schemes were sometimes used to characterize devices but they all had a manifold, gasket, and a device wirebonded to pads which were electrically connected, through a series of connections, to coaxial connectors.

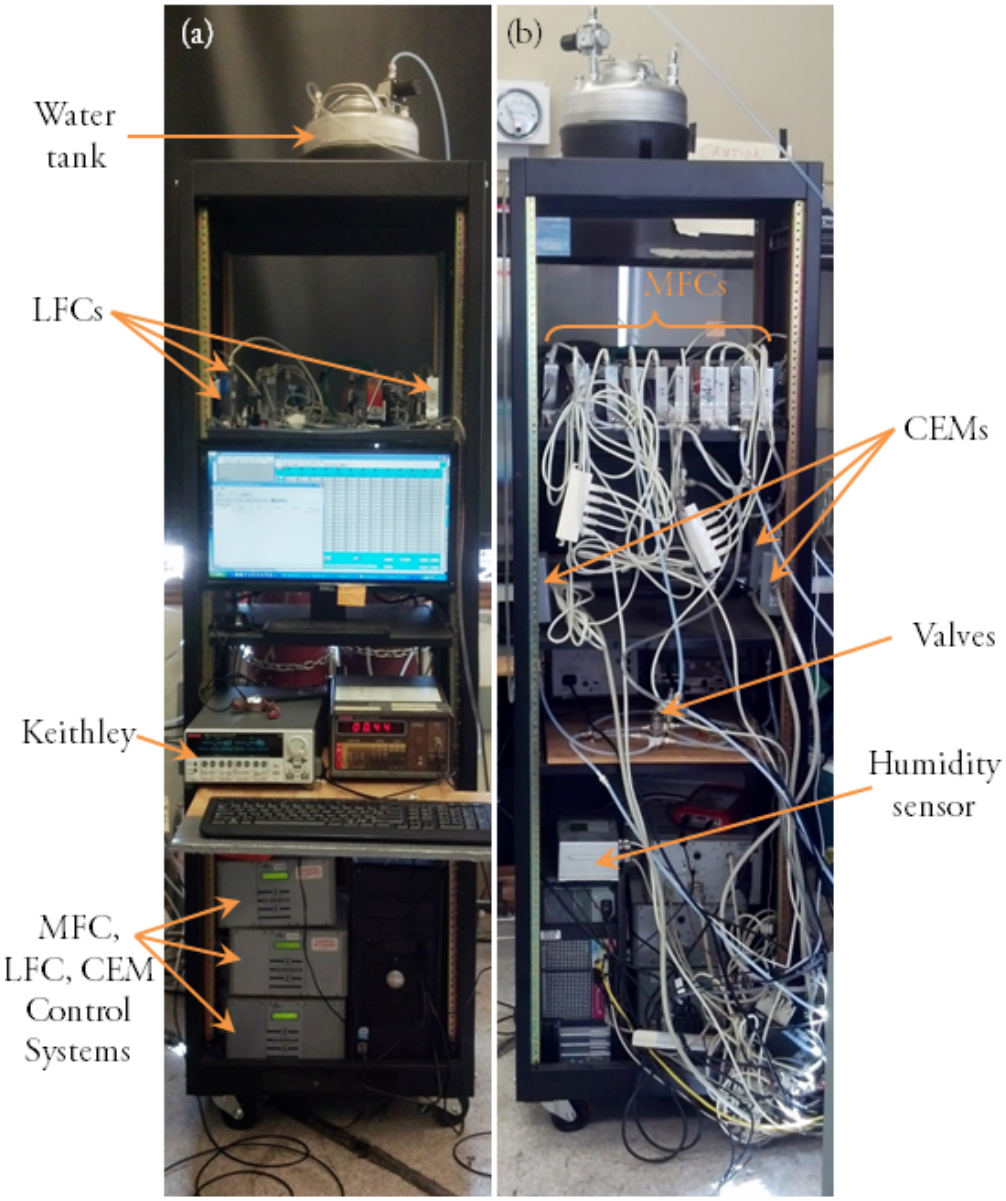

Figure 2.3: Pictures of the (a) front and (b) back of the gas delivery system, including water tank, liquid flow controllers (LFCs), and controlled evaporator mixers (CEMs) for injecting humidity, mass flow controllers (MFCs), Bronkhorst™ Digital Readout and Control Systems for controlling the MFCs, LFCs, and CEMs, gas flow valves, Vaisala™ HMT337 humidity and temperature transmitter, Keithley 2602A SYSTEM SourceMeter™, and computer.

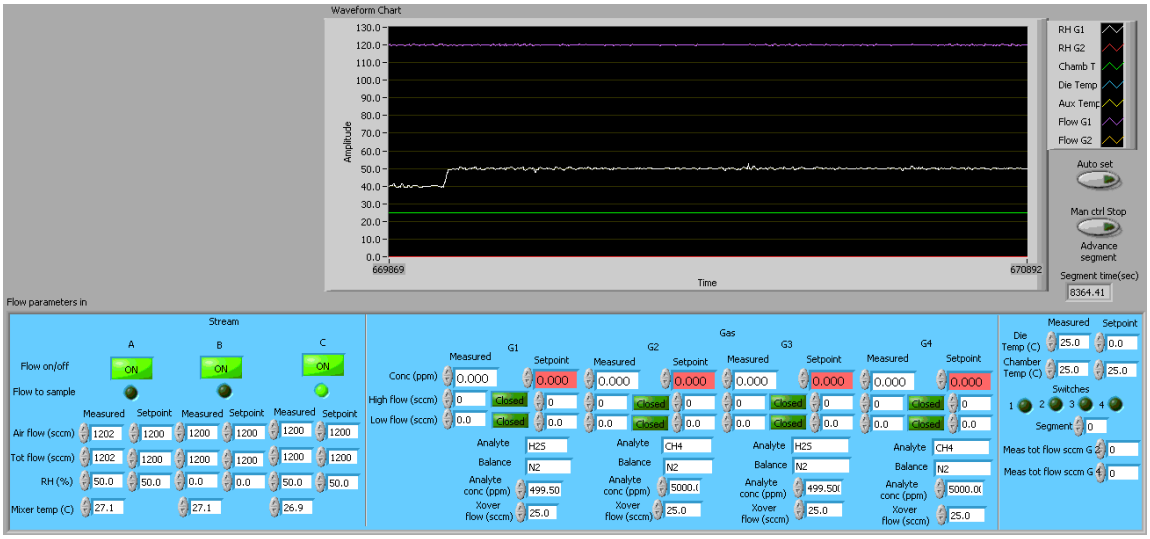

Figure 2.4: Front panel of Set-Read, the LabVIEW program from which the gas delivery system can be manually controlled and observed. From here a user can control (see the "Stream" section of the blue panel) which streams are flowing to the sample, the total flow on each stream, the relative humidity in each stream, as well as (see the "Gas" section of the blue panel) the target concentrations of each gas, and (see the rightmost section of the blue panel) the temperature of the chamber. This panel also displays the "actual" values of these and other quantities, in the "measured" text boxes.

tions, humidity level, and flow rate on each stream and which are delivered to the sample) for a certain amount of time, then configure the streams in a different way for a certain amount of time, and so forth. These "gas profiles" were input into a program layered on top of the previously mentioned program (Fig. 2.5).

A Teledyne API 101E was often used to measure hydrogen sulfide (H_2S) levels. A Vaisala HMT337 was used to measure humidity levels.

A program called Zephyr controlled the Keithley and collected all measurements (including from the MFCs, LFCs, CEMs, and valves, which it did by interfacing with the LabVIEW software). It output one data file which contained all the measurements at each measurement time.

2.4 Micro- and Nanoheaters

2.4.1 Introduction

In initial experiments, the device was heated using a temperature chamber, which took many minutes to reach its setpoint. We then moved on to Kapton heaters, which

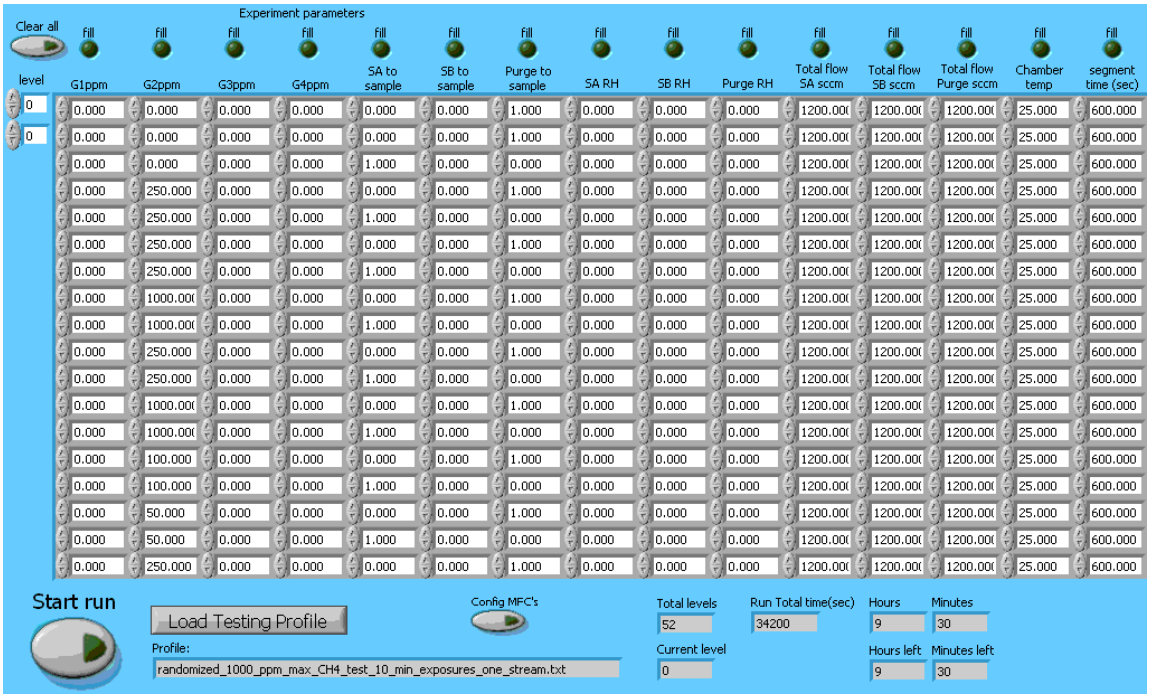

Figure 2.5: Front panel of Experiment Control, the LabVIEW program which calls on Set-Read (see Fig. 2.4) to run a gas profile. Each row is a specific configuration of the gas delivery system which is run for a specified amount of time.

heated the entire CERDIP and still took on the order of minutes to reach equilibrium. After this, we began using on-chip heaters, which brought the sample to the desired temperature extremely quickly (for some heaters, on the order of milliseconds), capitalizing on nanomaterials' low thermal mass.[167, 170] This allowed us to quickly probe the response to delivered gases at many temperatures and look at historetic effects in temperature change. From a sensing perspective, the ability to change temperature quickly allowed us to explore the change in conductance upon changing temperature as a measure of gas concentration. From an engineering perspective, on-chip heaters are much lower power than macro-sized heaters (in some cases, they operated in the milliwatts). And in our experiments, we found that we could operate our sensors in "pulsed-heating mode," heating the sensor at a low duty cycle, without decreasing response time, thus decreasing the average power consumption much further. "Pulsed-heating mode" was only possible because the on-chip heater and nanomaterials' low thermal mass allowed for fast temperature switching. For more information on our used of pulsed heating, see Mickelson et al.[132]

In addition, quickly cycling through different temperatures effectively creates multiple sensors. This is because the response of any nanomaterial to different gases varies with temperature. For example, at temperature A, the nanomaterial's response to gas 1 may be greater than to gas 2, but at temperature B that may be reversed. By quickly cycling through temperatures A and B, we are effectively measuring at both temperatures, and then can deconvolve the data in order to determine the concentration of both gas 1 and 2. By cycling through more temperatures, we can measure the concentrations of more gases (assuming the nanomaterial is responsive to the gases in the first place).[58, 75, 107, 150]

The following sections give descriptions of the various on-chip heaters we fabricated and/or used, in chronological order. I describe the fabrication process, device architecture, properties if tested, benefits of the heater, and the problems we encountered with it that led us to other on-chip heaters.

2.4.2 Gold Nanoheater on SiO_2

One of our first attempts at nanoheaters is shown in Fig. 2.6a. The nanoheaters are 500 nm wide, are made of electron-beam evaporated gold with a few-nm chromium sticking layer, and have been patterned on SiO_2. As discussed in later sections, the sensor in this case was a nanowire, 100 nm wide, fabricated alongside the heaters. Each heater was 500 nm from the edge of the nanowire. Driving current through the heaters causes them to heat up, thus heating up their surroundings, including the nanowire. Though the device shown in Fig. 2.6a looks functional, most devices had liftoff issues during the fabrication process (see Fig. 2.6b). For this reason, this design was replaced by a new one using a two-step fabrication process, as described in the next section.

2.4.3 Palladium Nanoheater on SiO_2

The subsequent and improved nanoheater design is shown in Fig. 2.6c. To avoid the liftoff problems we had previously, the nanoheaters and nanowires were fabricated in separate steps. (This required an alignment step in between.) This allowed us to bring the nanoheaters closer to the nanowire; whereas previously nanoheaters which were 500 nm from the nanowire still had liftoff problems, now the minimum heater-wire distance we attempted, 250 nm (as shown in Fig. 2.6c), had no liftoff problems. A smaller heater-wire distance is beneficial as it more effectively couples heater and wire temperature. In addition, having two fabrication steps allowed us to use different materials for the heater and wire. While previously we made the heater out of gold, this time we made it out of 10 nm palladium (with a 3 nm chromium sticking layer) because palladium is less susceptible to electromigration than gold.

2.4.4 Line Nanoheater on a SiN_x Membrane

In the previous design, the device was patterned on the substrate and so a significant amount of heat was lost to it, and the device could not reach a high temperature. To remedy this, our next design patterned the device on a silicon nitride (SiN_x) membrane, significantly reducing thermal coupling to the substrate.

The silicon nitride membrane fabrication was performed by Dr. Gavi Begtrup and is described in Fig. 2.7. Calibration devices (Fig. 2.8a) and sensor devices (Fig. 2.8b) were fabricated. Calibration devices consisted of nanoheaters and a resistive temperature detector (RTD). When the RTD heats up, its resistance changes and this resistance change can be used to determine its temperature. The RTD is serpentine in order to maximize its resistance (and thus the signal, which is resistance change) by minimizing its channel width and maximizing its length, and also so that it effectively measures the average temperature over the whole area it spans. Sensor devices have an IDE instead of an RTD. Sensing material can be deposited on the IDE to create a sensor. The IDE is in approximately the same place as the RTD, so the average temperature of the RTD should be approximately that of the active sensing area as well. Nanoheaters, IDEs, and RTDs all consisted of 15 nm palladium with a 5 nm chromium sticking layer.

These heaters were eventually abandoned because we realized that electromigration of the heaters occurred before they reached a high enough temperature.

2.4.5 Suspended Microhotplate

Another microheater we used were suspended microhotplates which heated up when current was driven through them (Fig. 2.9).[167, 170] These microhotplates were fabricated by Dr. Qin Zhou. More information about them can be found in Zhou, et al.[210] The microhotplate fabrication process is shown in Fig. 2.10.

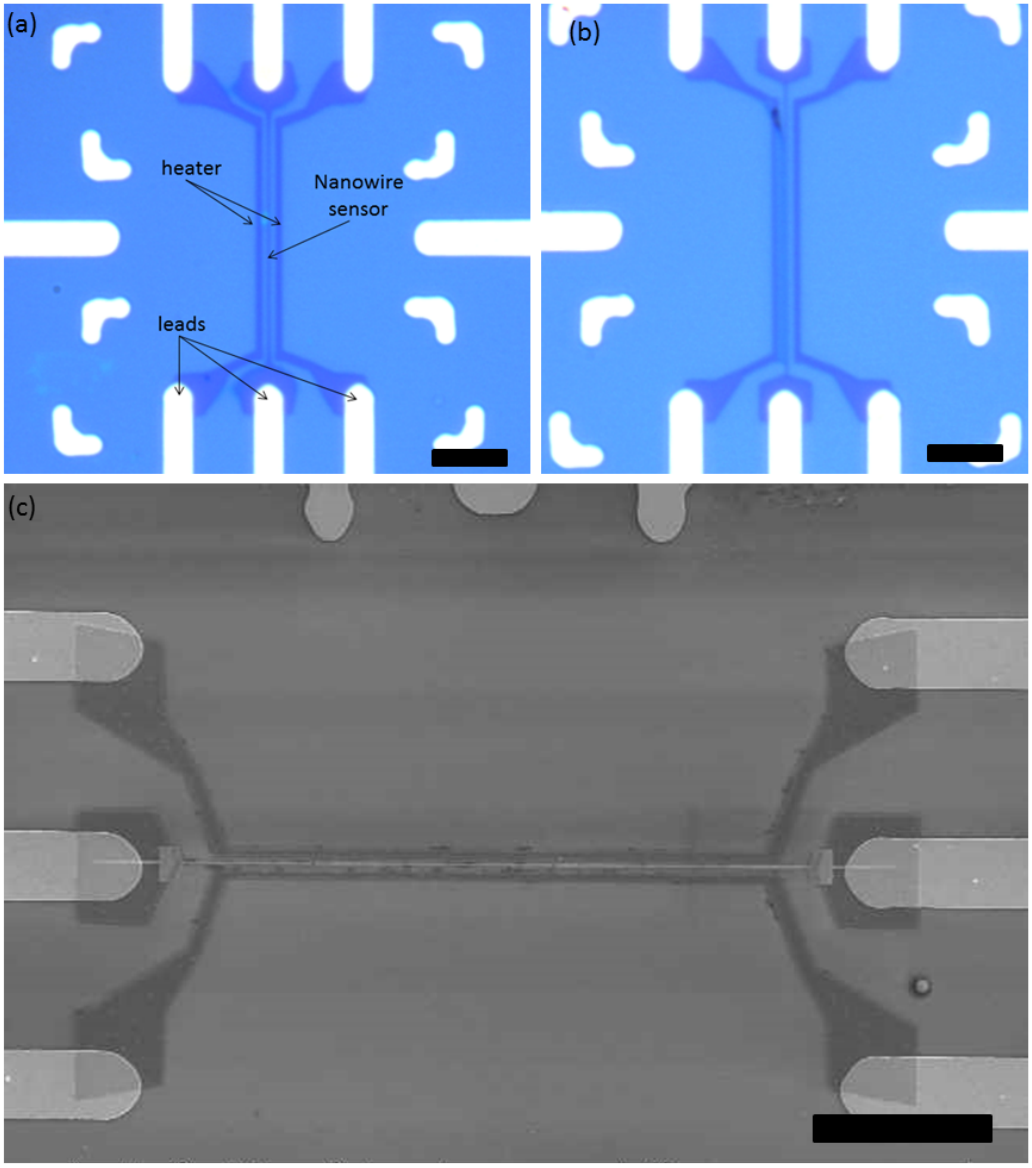

Figure 2.6: Nanoheaters on SiO_2. All scale bars are 10 μm. (a) Two gold nanoheaters and gold nanowire sensor. Fabrication was successful. (b) Another device with the same design. Gold between the left heater and the nanowire did not liftoff during the fabrication process. This was a common issue in making these devices. (c) SEM image of subsequent nanoheater/nanowire design. The design is the same as before, but nanoheaters are composed of 10 nm of thermally-evaporated palladium (with a 3 nm chromium sticking layer).

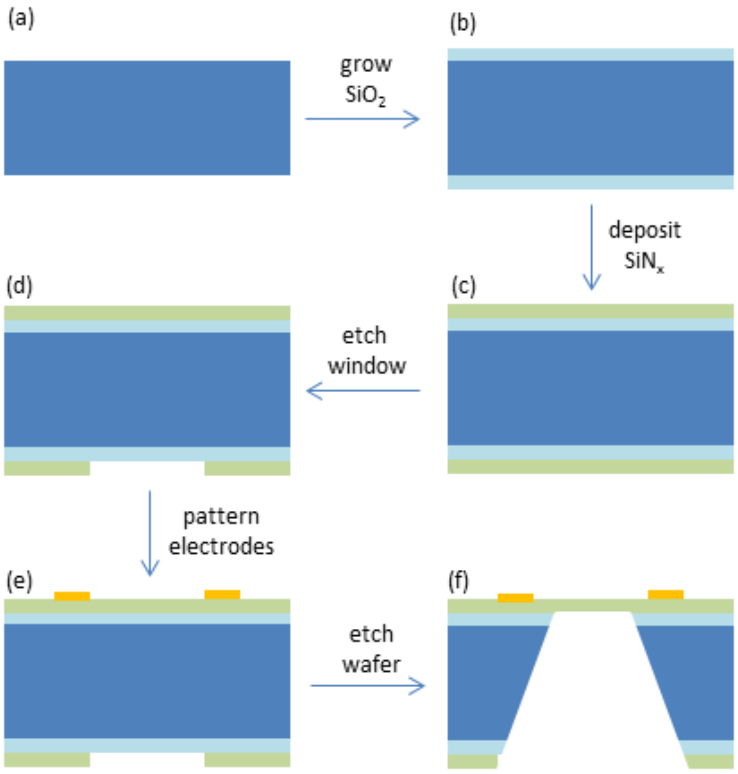

Figure 2.7: The fabrication process for silicon nitride membranes. (a) Begin with a wafer of polished silicon. (b) Grow 200 nm silicon dioxide on it. (c) Deposit silicon nitride conformally. (d) Etch windows into one side of the wafer. (e) Pattern electrodes around the future location of the membrane. (f) Etch through the wafer to produce a membrane.

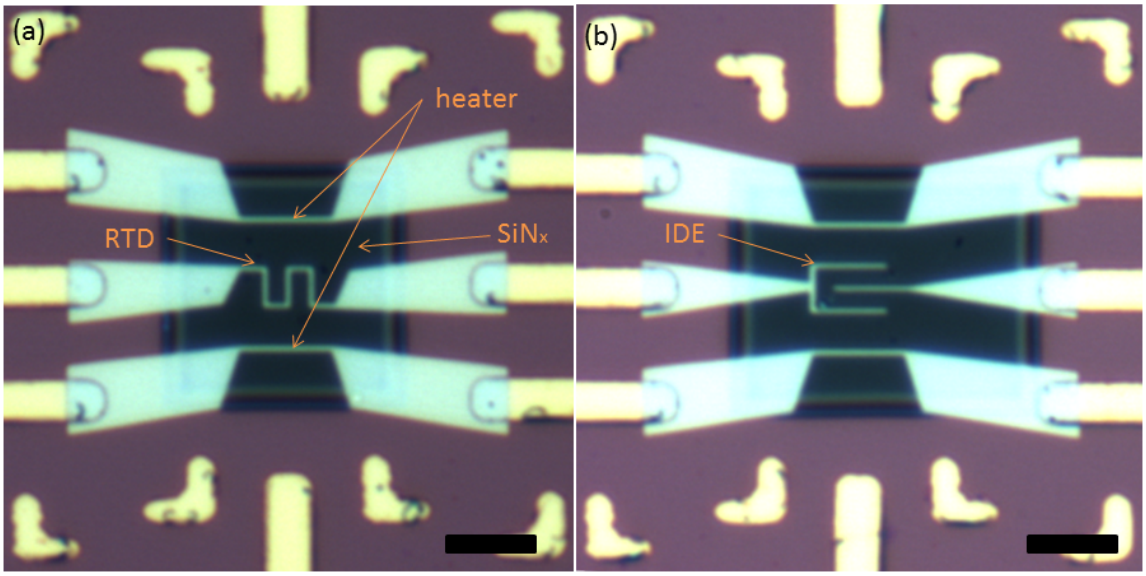

Figure 2.8: Devices with nanoheaters on SiN_x membranes for higher thermal isolation. Scale bars are 10 μm. (a) Calibration device. A resistive temperature detector (RTD) lies between the heater. The resistance of the RTD can be measured to determine its temperature. (b) Sensor device. Interdigitated electrodes (IDEs) lie between the heater. Sensing material can be deposited between the electrodes.

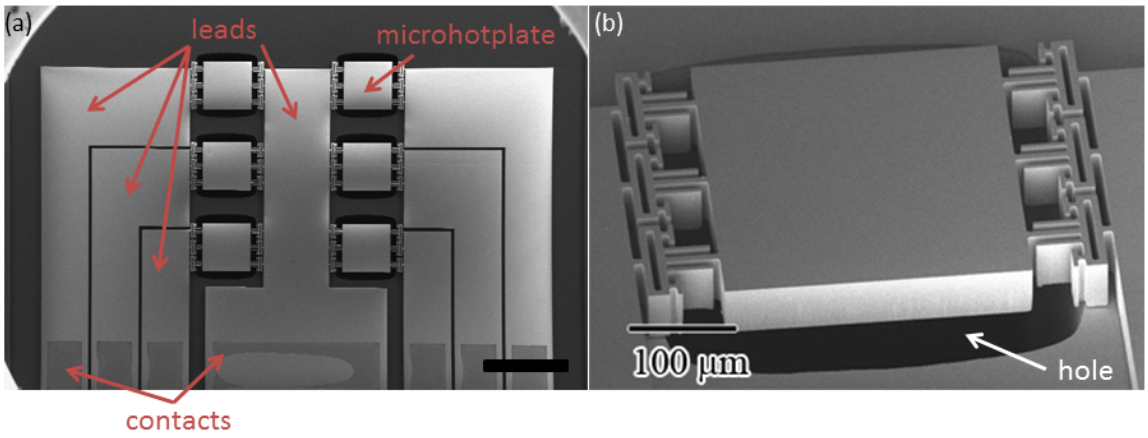

Figure 2.9: SEM images of the suspended microhotplates. (a) All the microhotplates on one chip (scale bar is 500 μm). The leads to the hotplates on the left are labeled. The center (horizontally) lead is the ground lead of all hotplates on the chip. The contacts to the upper left hotplate are labeled. In the corners of the image are the edges of the SEM electron gun. The leads, contacts, and microhotplates lie on a silicon substrate, where the substrate has been etched away under the microhotplates. (b) A microhotplate. Notice the hole where the silicon has been etched away under the microhotplate. ((b) is from [210])

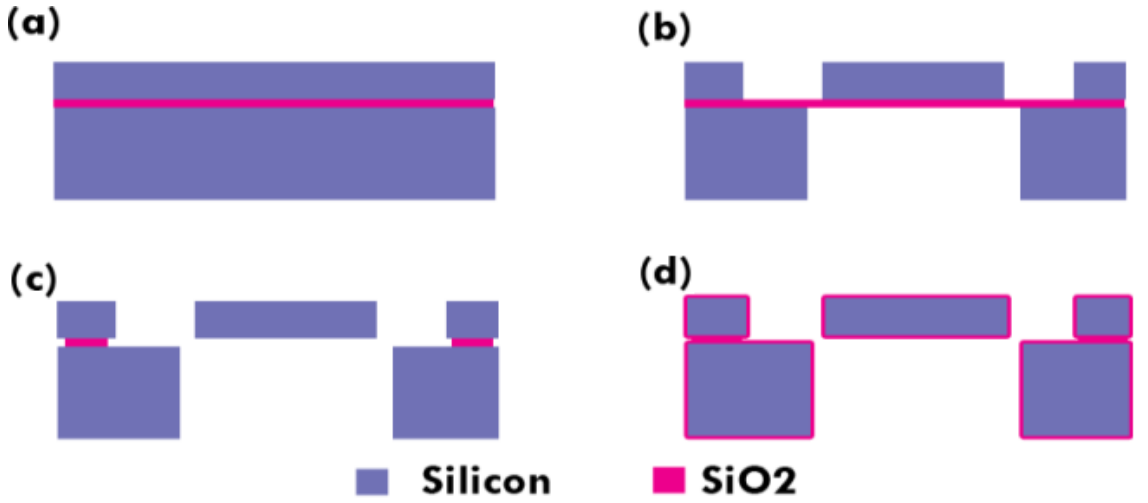

Figure 2.10: Fabrication process for suspended microhotplates. (a) Begin with a silicon-on-insulator (SOI) wafer with 50-μm-thick heavily-doped silicon as the top layer. (b) From the top, the area around the hotplate, supporting beams, and leads are etched away by through-hole deep reactive ion etching (DRIE). From the bottom, the hole under the microhotplate is also etched away by DRIE. (c) Insulator is removed by buffered HF. (d) Silicon dioxide is grown everywhere. (From [210])

In order to use these heaters, we had to pattern sensors on them, as shown in Fig. 2.11. Fig. 2.11a shows the Nanometer Pattern Generation System (NPGS) pattern for devices which we patterned on the microhotplates. The areas enclosed by the overlayed lines indicate where chrome/gold was to be deposited. The yellow lines on the bottom microhotplate are IDEs. The upper two microhotplates had nanowires patterned on them in a subsequent step. Note that, in case of the IDEs for example, a continuous path exists because the gold is deposited on the beams supporting the microhotplate.

In the end, though, there were bad liftoff problems associated with the sensor fabrication. Fig. 2.11b shows the bottom microhotplate, right after attempted liftoff. No gold had come off the microhotplate, thus shorting the IDEs. No gold came off the other microhotplates as well. There are clearly other areas where the gold did not liftoff either. After physically scratching through some excess gold and sonicating, the hotplates looked as shown in Fig. Fig. 2.11c. Though they look better, there is still much excess gold. A close look at the edge of the microhotplate revealed a thin strip of gold along the outline of the microhotplate, which sometimes continued to short the device (See Fig. 2.11d). We believe all these issues were due to the fact that the resist did not coat the edge of the microhotplates. This issue was not remedied by changing the resist.

In addition, these devices often had shorting between the sensor and heater. Upon

inspection with the SEM, we found multiple pinholes in the hotplate, which could have been the culprit (see Fig. 2.11e)

2.4.6 Serpentine Nanoheater on SiN_x Membrane

We had significantly more luck with microhotplates produced by the Kebaili Corporation (model #KMHP-100). These microhotplates are very low power (reaching 300°C at about 42 mW, as opposed to the previous heaters described, which reached the same temperature at about 4 W) and have a small form factor (each chip is about 1 mm x 1 mm x 0.5 mm). These properties made them very desirable for use in portable gas sensing applications.

A cross section of these microhotplates is shown in Fig. 2.12a, and a birds-eye view in Fig. 2.12b. Since the fabrication process is proprietary, it remains somewhat of a mystery. Temperature as a function of voltage and power were provided by the manufacturer;[88] temperature as a function of power is shown in Fig. 2.12c. Notice that the microhotplate can reach 300 C at around 43 mW.

These microhotplates were not without their problems. One problem was that the silicon nitride was deposited conformally on top of the heater, leading to sharp height changes on the surface of the silicon nitride. This made patterning devices between the electrodes difficult, as there would sometimes be discontinuities in the device where the height changed. It also made it difficult to deposit thin films of sensing material, as they would often have this problem of discontinuity as well.

Another problem with these microhotplates were large "flaps" of gold at the edge of the electrodes. These flaps were a result of the fabrication process – somehow, during liftoff, flaps of gold remain on the edge of the electrodes. These edges of these flaps seemed to be suspended well above the silicon nitride surface. This meant that when attempting to deposit continuous thin films or nanoparticle thin films, there would often be discontinuities, or intermittent contact, at the flap edge. We attempted to anneal the microhotplates, hoping heating them would relax the flaps and cause them to lay down, but had limited success. For this reason, we looked to other types of microhotplates for our applications.

2.4.7 Suspended Beam Microheaters

Another much-used microheater was a thin few-micron-wide suspended polysilicon beam, fabricated by Dr. Qin Zhou. The microheaters did not have the issues described earlier about the microhotplates produced by the Kebaili Corporation. They also had much lower power consumption (a few mW to reach 300°C). As will be discussed later, one strategy used to decrease power further was to operate our microheaters in "pulsed heating mode," only turning them on for x seconds every y seconds, where x is some small fraction of y. These new microheaters allowed us to achieve much shorter pulse widths than the Kebaili microhotplates due to their

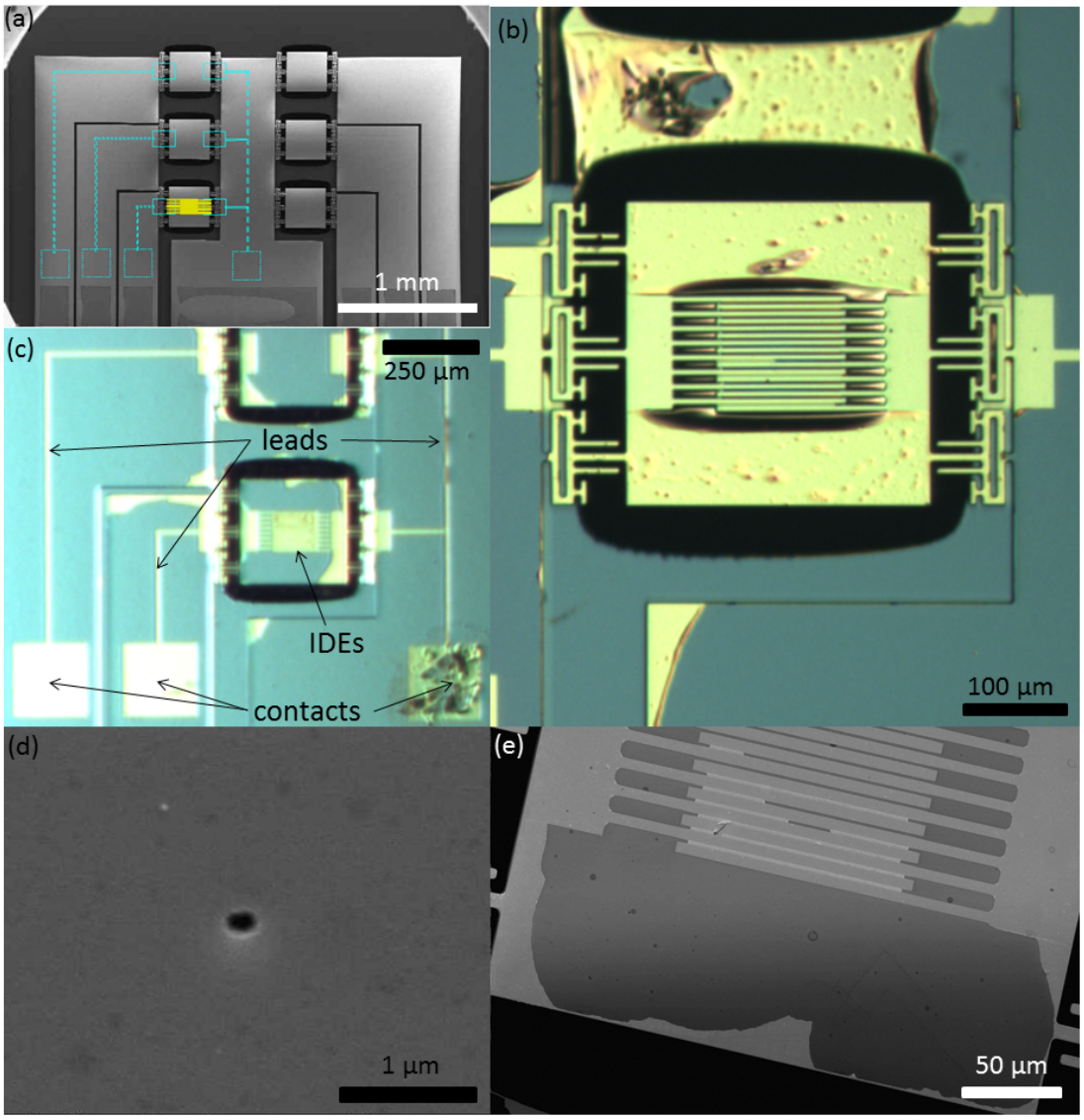

Figure 2.11: Patterning on microhotplates. (a) Nanometer Pattern Generation System (NPGS) pattern for devices. Areas within the overlayed lines will have gold deposited in them. In the case of the top two microhotplates, a nanowire will be deposited on them in a subsequent step. (b) Devices right after attempted liftoff. Gold has not lifted off at all on the microhotplates, as well as in other places. (c) Devices after scratching off leftover gold and sonicating. Much unwanted gold remains. (d) A pinhole in the hotplate, which could have caused shorting between the sensor and heater. (e) A thin gold line along the edge of the hotplate shorts the IDEs.

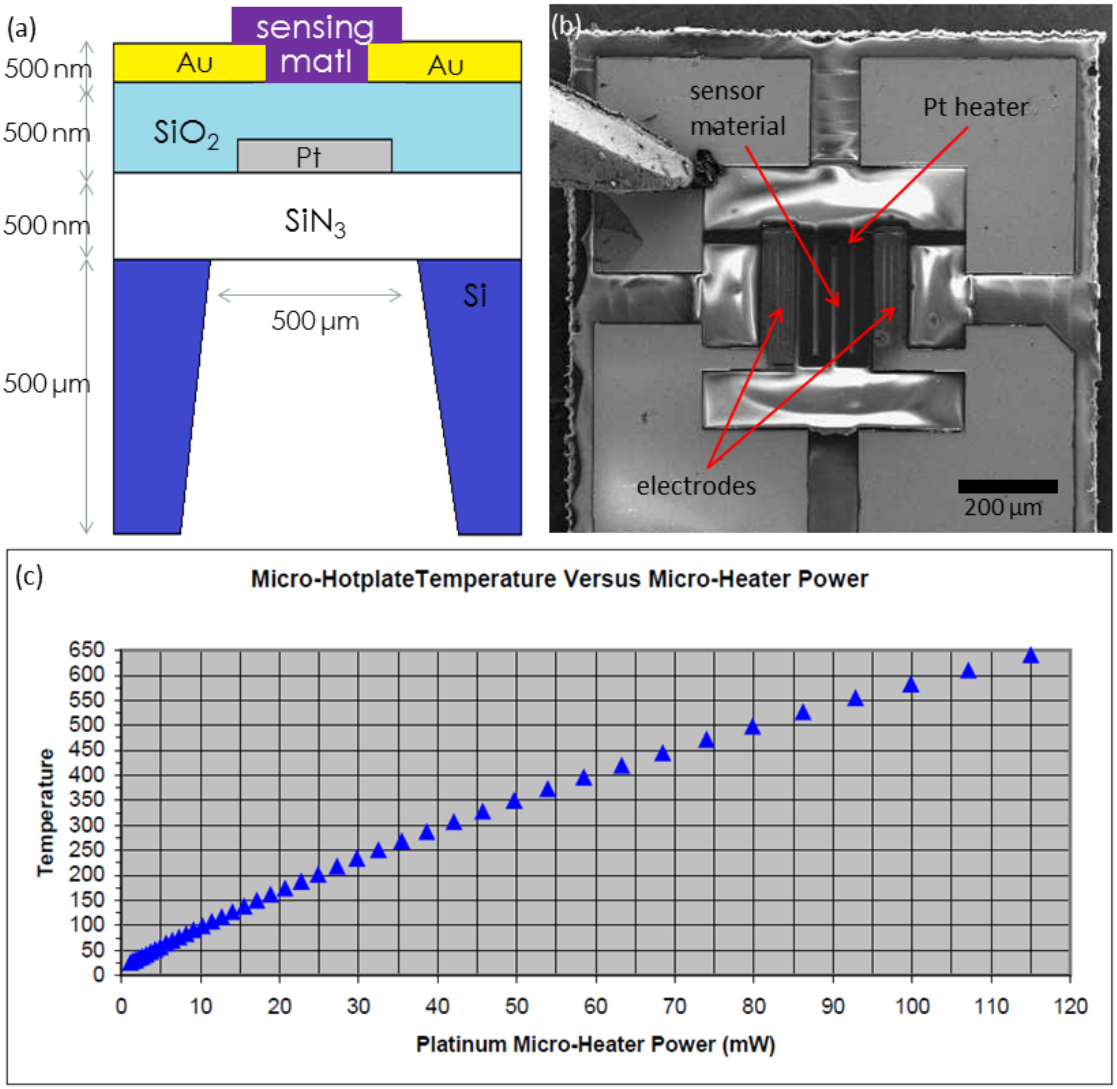

Figure 2.12: Microhotplates made by the Kebaili Corporation. (a) Cross section schematic and (b) Birds-eye view SEM image of microhotplate. A serpentine platinum heater lies on a square 500 μm x 500 μm silicon nitride membrane. Silicon dioxide has been deposited on the heater, and gold electrodes on top of that. A sensing material can be deposited between the electrodes. (The microhotplates do not come with sensing material.) The silicon dioxide electrically isolates the electrodes from the heater. In the upper left hand corner of the SEM image, a clip holds down the device. (c) Temperature versus power for the microhotplate. (Panel (c) is from [88].)

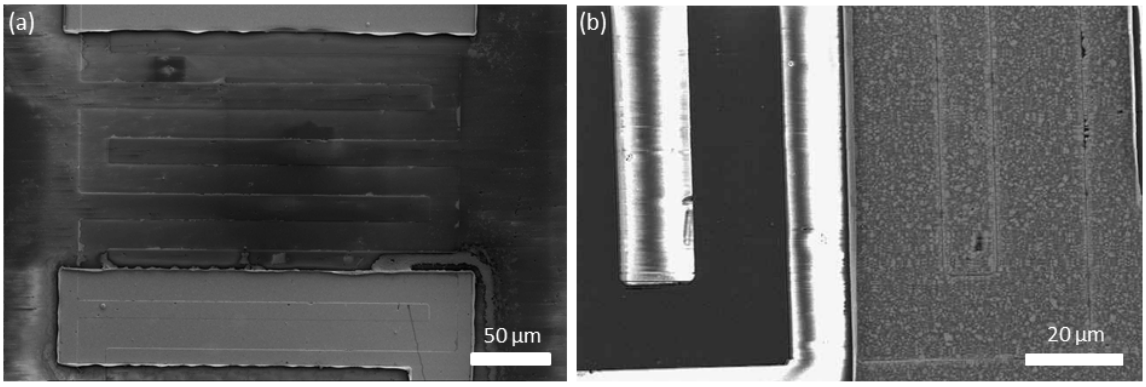

Figure 2.13: "Flaps" on the edge of the electrodes on Kebaili's microhotplates. (a) A device before annealing. Note that device has a small amount of tungsten oxide nanoparticles in places. (b) A device after annealing at 600°C for 30 min in 4% hydrogen in argon. Flaps have folded back, but only in some regions.

faster thermal response time (about 25 μs). Also, as opposed to the microhotplates produced by the Kebaili Corporation, which had only one device per chip, this design many microheaters per chip (72 in the first generation, 12 in the second), allowing for multiplexing of sensors. Each microheater could have a different sensing material deposited on it, or could be operated at a different temperature – in the presence of a gas, each sensor would give a different signal and an analysis could be done to determine the levels of many different gases. This would be a method of circumventing the issue of cross-sensitivity that most individual sensors have.

There were many different variations of the design; one particular design is shown in Fig. 2.14. Fig. 2.14a shows a birds-eye view SEM image of a device and Fig. 2.14c shows a cross-section of the device along the line shown in Fig. 2.14a. The microheater consists of a polysilicon beam suspended over a trench. The polysilicon beam is insulated by silicon nitride. On top of the beam are two electrodes between which sensing material can be deposited. In this case, there is also a thermocouple on the beam. The heater, sensor, and thermocouple are contacted via contacts on the top and bottom of Fig. 2.14a. The heater contacts have been etched through to the polysilicon in order to contact the heater.

The fabrication of the microheaters is shown in Fig. 2.15. The process begins with a silicon wafer. 100 nm of silicon-rich low-stress nitride (LSN), followed by 100 nm of undoped polysilicon, and finally 2 μm of boron-doped silicon dioxide was deposited. The wafer was heated to 1050°C to enable film stress release and dopant diffusion into the polysilicon layer. The wafer was then etched in a buffered hydrogen fluoride bath to remove the oxide (Fig. 2.15a). The heater was then patterned in the following way: 1-μm Fujifilm OiR 897 photoresist was spun onto the wafer. Photolithography was used to pattern the photoresist (Fig. 2.15b). Using

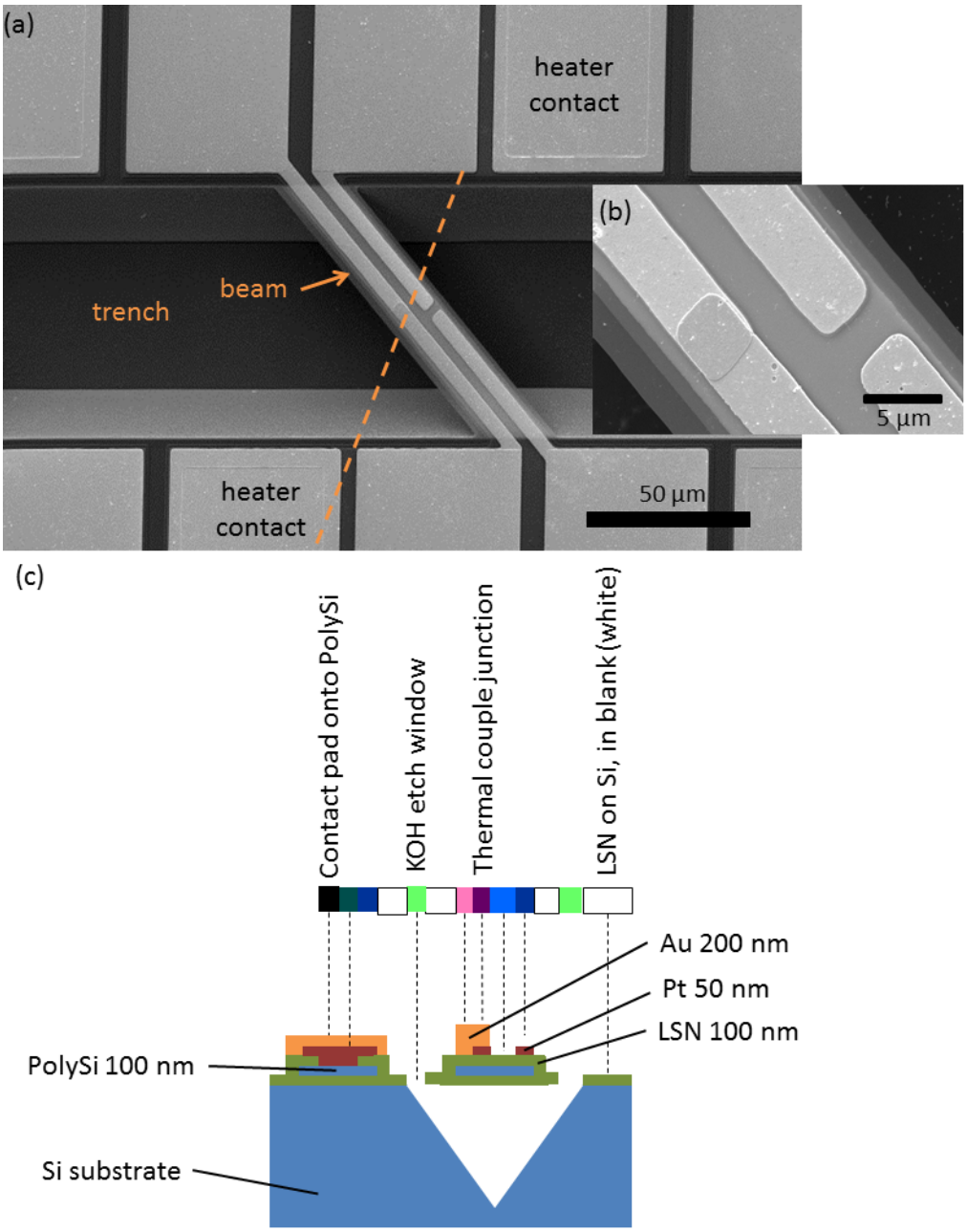

Figure 2.14: Design of a first-generation suspended-beam microheater. (a) SEM image of device. (b) SEM image of active area of device. (c) Cross-section along dotted line in (a) (not to scale). (LSN is low-stress nitride.) (Courtesy of Dr. Qin Zhou.)

the photoresist as an etching mask, the polysilicon and LSN were plasma etched. The photoresist was striped with acetone, and the wafer was then piranha etched (Fig. 2.15c). After patterning the heater, 100 nm of LSN was deposited (Fig. 2.15d) and patterned with a similar technique as was used for the heaters (Fig. 2.15e). The platinum was then patterned in the following way: photoresist was spun on and patterned using photolithography. 10 nm of chromium and then 60 nm of platinum were deposited on the wafer by electron-beam evaporation. Liftoff was performed in acetone. The wafer was ultrasonicated in a bath (Fig. 2.15f). It was then annealed in nitrogen at 350°C for 1 hour to release platinum film stress. After patterning the platinum, a similar process to patterning the platinum was used to pattern 100 nm of gold (with a sticking layer of 10 nm chromium) (Fig. 2.15g). The wafer was then diced and released in a potassium hydroxide bath (Fig. 2.15h).

A number of methods, involving simulation, theoretical analysis, and experiment, were employed by Dr. Qin Zhou to estimate the voltage/power at which they reach 300°C.

An ANSYS® simulation was performed for a polysilicon beam of thickness 200 nm, width 4 μm, and length 100 μm in air. Fig. 2.16a shows the temperature profile along the beam, and Fig. 2.16b through the air. It was found that when the center of the beam reached 343.52°C, 1.2 mW was lost through beam conduction and 1.3 mW through air conduction, for a total power consumption of 2.5 mW. (Radiation and convection were ignored – radiation is insignificant in this temperature range, and convection is unimportant at these length scales.)

These microheaters had significantly fewer problems than the other ones we dealt with, but were not without their own problems. In the first generation of suspended beam microheaters, the contact pads were very small and close to each other and the microheater, which made it very hard to wirebond to the pads without shorting the contacts or damaging the microheater. This was solved by the second-generation microheaters, which had a different chip design in which the pads were larger and far from the heaters but which had significantly fewer devices per chip (twelve, as opposed to the first generation which had seventy two).

2.5 Nanomaterials

2.5.1 Semiconducting Metal Oxides: Sensing Mechanism

The following is a concise summary of the general sensing mechanism of semiconducting metal oxides and a few specific cases. For more information, we direct the reader to the excellent review in the chapter "Electrical-Based Gas Sensing" in *Solid State Gas Sensing* by Comini et al.[34] as well as many other resources.[4, 57, 70, 82, 97, 103, 120, 137, 168]

Let us first consider the case of a bulk n-type semiconducting metal oxide (SMO)

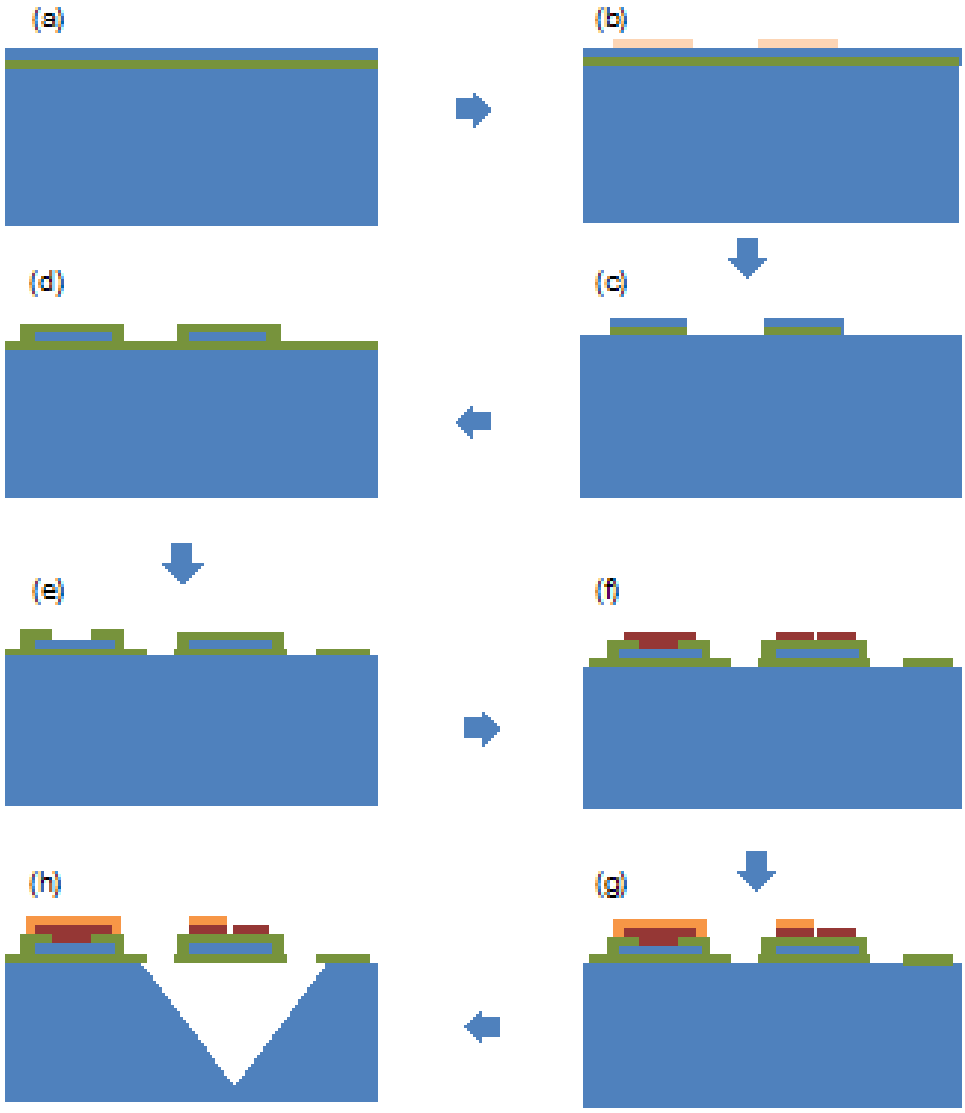

Figure 2.15: Fabrication process for suspended-beam microheaters. (See text for a detailed description of process.) (a) Poly-Si on a low-stress nitride (LSN) on a Si wafer. (b) Photoresist spincoated and patterned. (c) Poly-Si and LSN plasma etched to form heaters. Photoresist removed. (d) More LSN deposited. (e) Using photolithography, heater contacts and etch windows plasma etched. (f) Using photolithography, Pt e-beam evaporated to form leads, electrodes, and thermometers. Wafer cleaned and annealed for Pt stress release. (g) Au similarly patterned. (h) Trench etched in KOH bath. (Courtesy of Dr. Qin Zhou.)

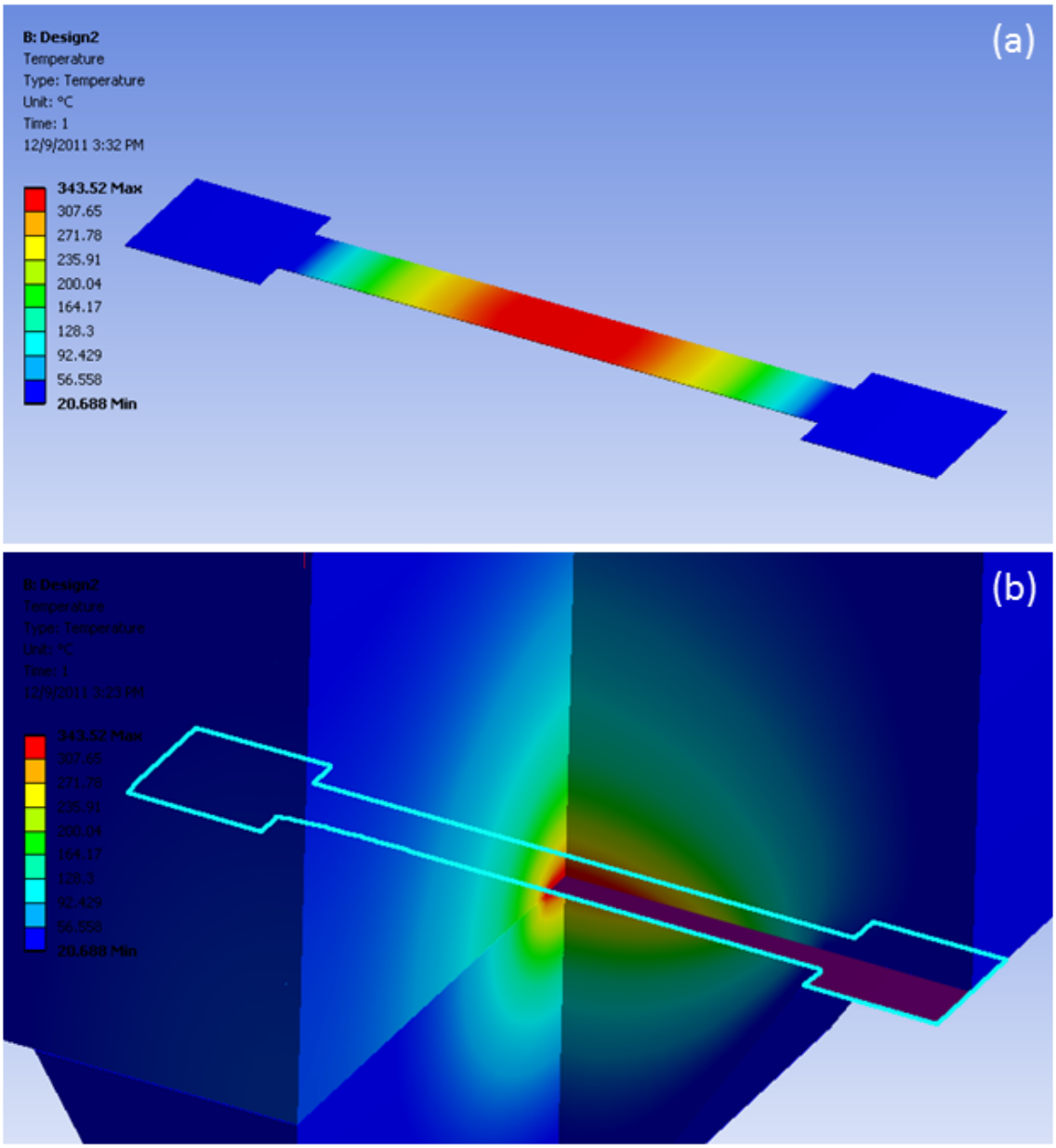

Figure 2.16: ANSYS® simulation of a suspended beam. (a) Temperature profile along beam and (b) in air. (Courtesy of Dr. Qin Zhou.)

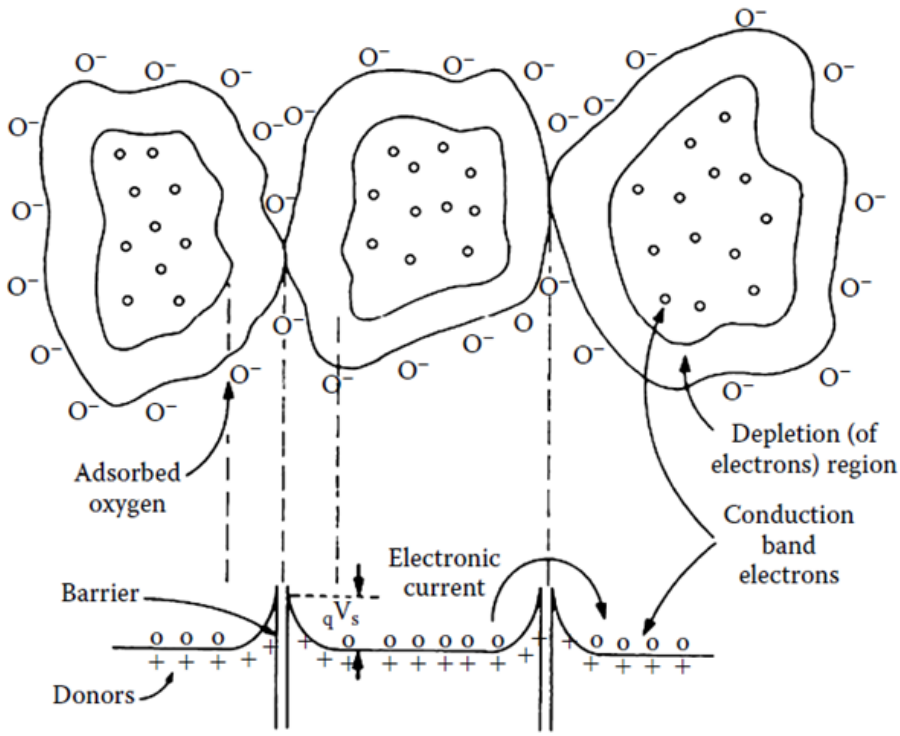

Figure 2.17: A schematic of SMO in an oxygen-containing environment. Oxygen ions adsorb on the surface of the SMOs, creating depletion regions, which serve as barriers to electron transport. (From [70])

sample with many grains. In vacuum, during electron transport through the sample, electrons must hop across grain boundaries, and this hopping dominates the conductance of the sample.

In an oxygen-containing environment (such as ambient air), oxygen ions adsorb on the surface of SMOs in a process called ionosorption (Fig. 2.17). In the case of bulk SMOs, the adsorbates diffuse along grain boundaries and adsorb there. For an n-type semiconductor, these oxygen ions remove electrons from the bulk, forming a depletion region near the surface of the SMO. These depletion regions increase the barrier in inter-grain hopping, thus decreasing conductance compared to vacuum.

The sensing mechanism of particular n-type bulk SMOs for particular reducing gases differs, but the sensing mechanism that is generally accepted to be the most common is as follows: the gas reduces adsorbed oxygen, releasing electrons back to the bulk, which increases the carrier concentration, and decreases the depletion width. As the depletion layer gets thinner, electrons can hop more easily between grains, and conductance increases.

If the reducing gas is in an oxygen-containing environment (such as ambient air), the reducing gas continuously removes oxygen from the surface, but oxygen ions

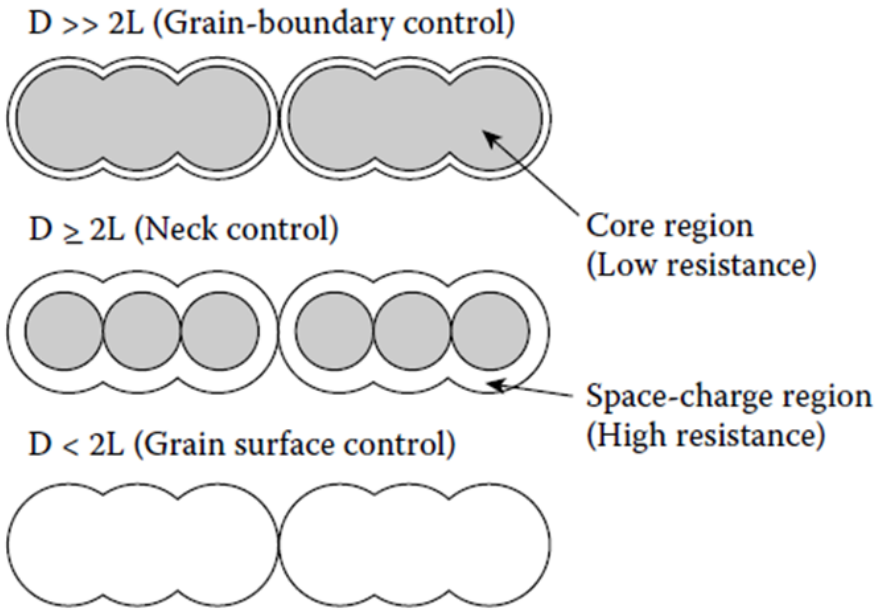

Figure 2.18: Effect of grain size on conduction. When grain size, D, is much larger $2L$ (where L is the space charge depth), depletion regions form on the surface of grains. (top) When D is larger than but on the same order as $2L$, barriers to electron transport may form at "necks" in the grains. (middle) When D is less than $2L$, the whole grain is depleted of electrons and conduction is on the surface. (bottom) (From [70])

continuously adsorb on the surface, so the degree of reduction is proportional to the ratio of the amount of reducing gas to the amount of oxygen.

Consider now the case of a network of SMO nanostructures (such as nanoparticles), which are each the same size as the grains in the previous case. The model above applies, but to nanoparticles instead of grains. Electrons travel across the sample, hopping between nanoparticles. In ambient air, oxygen ions adsorb on each nanoparticle, forming depletion layers at the surface of each nanoparticle, decreasing conductance compared to in vacuum. Reducing gas removes adsorbed oxygen from the surface of each nanoparticle, decreasing depletion width and increasing conductance.

If we decrease nanoparticle size, though, the depletion region takes up more and more of each nanoparticle (Fig. 2.18). Eventually, the depletion region takes up the whole nanoparticle – the entire nanoparticle has been depleted of charge carriers (Fig. 2.18, bottom). In this case, all electron transport is along the nanoparticle surfaces. Since the depletion width is generally on the order of 100 nm in ambient air, this is the case for most nanoparticles, temperatures, and reducing gas concentrations.

The model considered so far applies to reducing gases and n-type SMOs. When

an n-type SMO is exposed to an oxidizing gas, the general effect is for the gas to adsorb and further remove electrons from the sample. Since n-type SMOs tend to already be very resistive (for the reasons previously outlined), this change is hard to measure, so n-type SMOs are generally not used to detect oxidizing gases. Typically, a full monolayer of oxygen ions adsorbs on a p-type SMO because the metal ions of the lattice can be oxidized to a higher oxidation state.[97] In this case, ionosorption is hole donating, increasing conductance, and no space charge layer is formed. Exposure to reducing gases simply removes holes, decreasing conductance.[4] Exposure to oxidizing gases produces little effect, since a full monolayer of oxygen ions is already adsorbed.

There is some debate, however, over whether this model correctly describes the interaction of any SMOs and redox gases. Gurlo & Riedel[63] claim that there is no convincing evidence of oxygen ionosorption and put forth a different model, in which conductance modulation comes about as a result of the oxidation and reduction of surface lattice oxygen vacancies, not adsorption and reduction of ionosorbed oxygen. The model is as follows. N-type SMOs are generally n-type because they have oxygen vacancies which act as electron donors. In an oxygen-containing environment, some of those surface lattice vacancies oxidize, removing electrons from the bulk and forming space charge regions. Reducing gases remove some surface lattice oxygen, freeing electrons and reducing the depletion width. It is possible that chemiresistive effects are generally also due to gas-induced modulation of electron mobility.[148, 168, 180]

In many cases, other effects dominate the sensing mechanism. Sometimes the gas reacts with the SMO itself to change its conductivity. Some have claimed this is the case for H_2S gas interacting with WO_3, as discussed in the following section. In some cases, the gas adsorbs on the SMO and direct charge transfer occurs.[103] Sometimes products of the initial reaction (such as water) will go on to modulate the conductivity of the SMO.[137] The specific cases of the gases H_2S, water, and methane will be treated in the following sections.

2.5.1.1 Hydrogen Sulfide and Tungsten Trioxide

It is generally believed that H_2S interacts with WO_3 by the standard ionosorption model outlined above. Some have claimed that the interaction takes place via a direct reaction of the H_2S with WO_3, namely[12, 44, 49]

$$3\,WO_3 + 7\,H_2S \longrightarrow 3\,WS_2 + SO_2 + 7\,H_2S \tag{2.26}$$

The WS_2 dopes the WO_3, acting as an electron donor.[9, 136]

2.5.1.2 Water

Most SMOs (and most solid state devices in general) are responsive to water, at least at low temperatures.[123] Tin dioxide, for example, is responsive to water up to

600°C.[130] Between 300 and 600°C, the response is reversible.[137] The overall effect of water adsorption is to increase surface conductance.[34] At low temperature, the response is due to physisorption[123] – as discussed earlier, physisorption dominates as the principle type of adsorption at low temperatures. At higher temperatures, the surface reactions are still debated and many mechanisms have been proposed. Morrison[135] has suggested that the polar H_2O molecule adsorbed adjacent to oxygen ions changes the energy level of the oxygen ion and its rate of electron injection and extraction, which leads to a loss in the density of adsorbed oxygen. Comini et al.[34] notes that chemisorption of water onto oxide can be from air can be very strong, forming an "hydroxylated surface," where the OH^- ion is bounded to the cation and the H^+ ion to the oxide anion.

2.5.1.3 Methane

Methane is example of a gas for which the sensing mechanism is quite complicated and involves a number of intermediate reactions. In the following analysis, which comes largely from Kohl's review,[97] the SMO is tin dioxide, which is often thought of as an archetypal SMO. The sensing mechanism is depicted schematically in Fig. 2.19. As shown, there are two channels. (There is actually a third that will be described as well.)

One channel, shown in Fig. 2.19d-g, involves reaction with lattice oxygen. First methane dissociates to a methyl group and hydrogen (Fig. 2.19d).

$$\mathrm{CH_{4gas}} \longleftrightarrow \mathrm{CH_{3ads}} + \mathrm{H_{ads}} \tag{2.27}$$

This reaction requires only the activation to break one of the four C−H bond and so can occur below 350 K. The two methyl groups form a rooted (i.e. containing lattice oxygen) ethoxy-like molecule (Fig. 2.19e)

$$\mathrm{CH_3} + \mathrm{CH_3} + \mathrm{O_{lat}} \longrightarrow \mathrm{CH_3CH_2O_{lat}} + \mathrm{H_{ads}} \tag{2.28}$$

At higher temperature the ethoxy-like species converts to an acetate-like species (Fig. 2.19f)

$$\mathrm{CH_3CH_2O_{lat}} + \mathrm{O_{lat}} \longrightarrow \mathrm{CH_3CO_{lat}O_{lat}} + 2\,\mathrm{H_{ads}} \tag{2.29}$$

Acetic acid and ketene desorb during this reaction. The acetate-like species is the most stable molecule in this reaction chain. Decomposition starts around 580 K and completes around 750 K. This means that at temperatures well below 700 K, the acetate-like species may block sites for further methane adsorption. The hydrogen produced from the previous reactions feeds the decay of the acetate-like species to a formate-like species (Fig. 2.19g)

$$\mathrm{CH_3CO_{lat}O_{lat}} + 2\,\mathrm{H_{ads}} \longrightarrow \mathrm{CH_{4gas}} + \mathrm{HCO_{lat}O_{lat}} \tag{2.30}$$

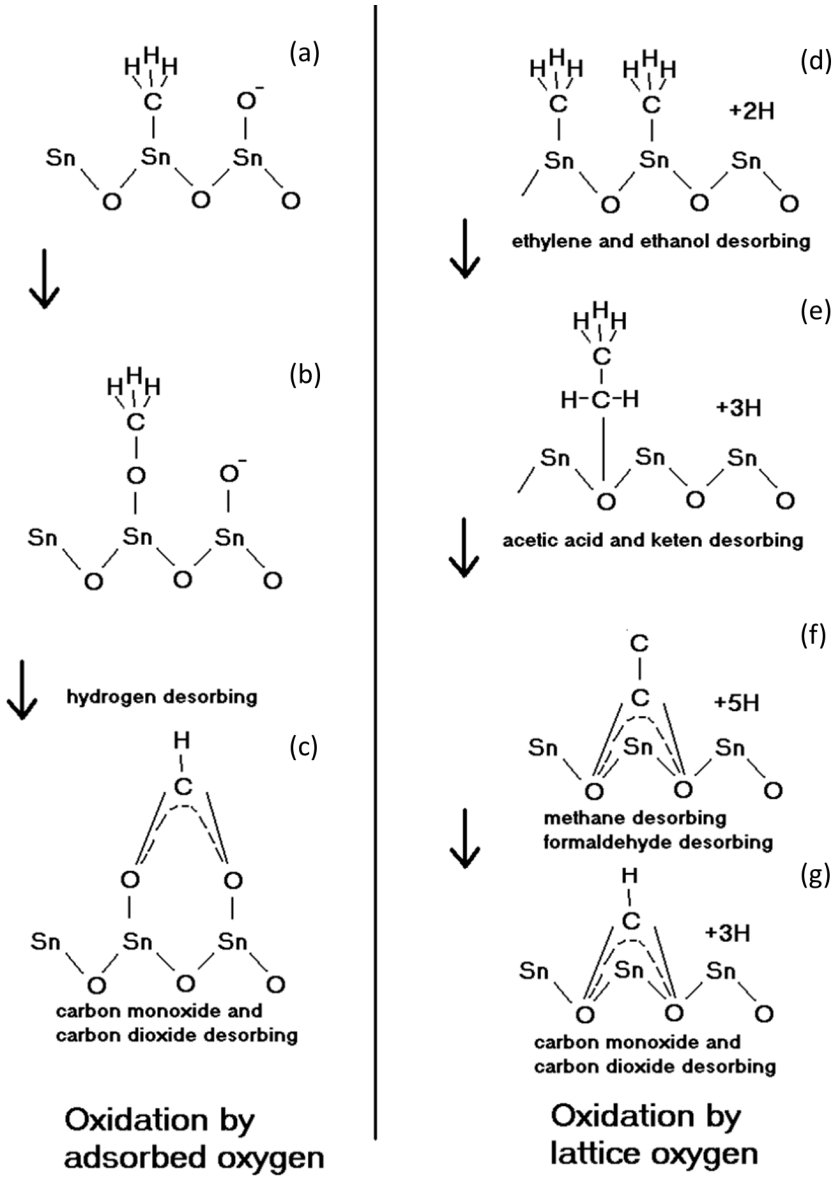

Figure 2.19: The two channels of the sensing mechanism of SnO_2 for methane. (From [97])

Methane and formaldehyde desorb during this reaction. The temperature to drive the previous reaction is 580-750 K, but the formate-like species is unstable above 500 K, so the formate-like species decomposes spontaneously via two channels

$$HCO_{lat}O_{lat} \longrightarrow CO_{2gas} + H_{ads} + 2\,V_0 \tag{2.31}$$

$$HCO_{lat}O_{lat} \longrightarrow CO_{gas} + O_{lat}H_{ads} + V_0 \tag{2.32}$$

where V_0 is an oxygen vacancy, which donates electrons to the lattice.

Another possible reaction channel exists in which methane is oxidized by adsorbed oxygen (Fig. 2.19a-c). As before, it begins with the formation of a methyl group on an Sn atom. (Fig. 2.19a). This methyl group can then form on top of adsorbed O^- to create a methoxy group, CH_3O^- (Fig. 2.19b). This methoxy group can convert to a formate group (Fig. 2.19c), which can decay, as before, to carbon monoxide, carbon dioxide, and hydrogen, this time consuming ionosorbed oxygen rather than lattice oxygen.

A third reaction route proceeds from eq. 2.28 (Fig. 2.19e) in which the water and ethylene are produced and desorb and a surface oxygen vacancy remains

$$CH_3CH_2O_{lat} + H_{ads} \longrightarrow H_2O_{lat} + C_2H_{4gas} \longrightarrow H_2O_{gas} + C_2H_{4gas} + V_0 \tag{2.33}$$

This reaction does not affect the SMO conductance, however. It is also the dominant mechanism over that shown in Fig. (2.19d-g) below 600 K.

2.5.2 Semiconducting Metal Oxides: Tungsten Oxide

Some studies have shown that tungsten oxide (WO_3) nanoparticles have low cross-sensitivity to gases other than H_2S.[46] This makes them both a good potential sensing material for H_2S and scientifically interesting: what is the sensing mechanism of WO_3 for H_2S?

As discussed in Sec. 2.5.1.1, a few competing theories exist as to the sensing mechanism of WO_3 for H_2S and there has been no definitive proof of any. One theory is that the H_2S affects WO_3 in the standard way that a reducing gas affects an SMO – it reduces adsorbed oxygen, decreasing the width of the space charge layer at the surface of the SMOs, thus decreasing the hopping barrier and increasing conductivity.[12, 44, 49] Another theory is that H_2S reacts with the WO_3 to form WS_2 (see Eq. 2.26), which acts as an electron donor.[9, 136]

Tungsten oxide nanoparticles were obtained in powder form from MKnano (product #MKN-WO3-090). They are 99.5% pure with an average diameter of 90 nm.

A number of experiments were done in an attempt to determine the sensing mechanism of WO_3 nanoparticles for H_2S.

2.5.2.1 Transmission Electron Microscopy

A transmission electron microscope (TEM) shoots high-energy (hundreds of keV) electrons at a sample and analyzes the scattered electrons (especially transmitted electrons) to reconstruct an image of the sample. In order to study transmitted electrons, the sample must be thin (ideally under 20 nanometers) and suspended on a TEM grid (a support structure with small holes) or thin membrane. They generally have some of the highest resolutions of microscopes (for good samples, on the order of angstrom), and, among other things, can image lattice fringes, lines which result from the interference of the electrons with the sample's crystal lattice.[196] In the case of this problem, we can image the sample before and after exposure to H_2S to see if there are nanometer-scale changes in surface morphology or lattice structure. Our TEM is a JOEL 2100.

In our first attempt to get WO_3 nanoparticles on TEM grids, the nanoparticles were placed in de-ionized water (from a Millipore Milli-Q Integral 5) at a concentration of 10 mg/ml and bath sonicated for 20 minutes. Holey SiO Transmission Electron Microscopy (TEM) grids were then dipped in and moved through the solution (Fig. 2.20). As shown, the nanoparticles would sometimes agglomerate in structures that hung over the holes in the SiO. The idea was that at the edge of these structures, single nanoparticles were suspended and could be imaged at high resolution. However, these grids charged up too much, causing vibrations, and lattice fringes could usually not be observed (Fig. 2.21).

To avoid this, 1-2 nm of platinum was sputtered on a TEM grid using an Anatech Hummer 6.2 Sputter System, which solved the charging problem. (The TEM grid used was an SPI Supplies® 50-nm-thick SiN_x membrane with perforated holes.) WO_3 nanoparticles were prepared and deposited similarly to previously (sonicated 1 hour rather than 20 minutes). The grid with nanoparticles deposited is shown in Fig. 2.22.

TEM images were taken before and after exposure to H_2S. WO_3 reaction with H_2S is very slow near room temperature but on the order of minutes for 50 ppm H_2S at 300°C, so the sample was brought to 300°C and exposed to 50 ppm H_2S for about 12 minutes. (Since a TEM grid has no on-chip heater, this was done by placing the sample in a quartz tube through which the delivered gases flow, which was heated by a block heater, machined to surround the tube exactly, surrounded by insulation – see Fig. 2.23.) If the sample were allowed to recover at 300°C, it would revert to its initial state within minutes, since recovery happens quickly at elevated temperatures. However, at room temperature, recovery takes much longer. To "lock" the sample into its exposed state so it can be observed in the TEM, the sample continued to be exposed to H_2S while its temperature was lowered, and was only removed from the H_2S when it reached room temperature. For consistency, before the first TEM session, the sample was brought through the same procedure but without H_2S delivered (only dry air).

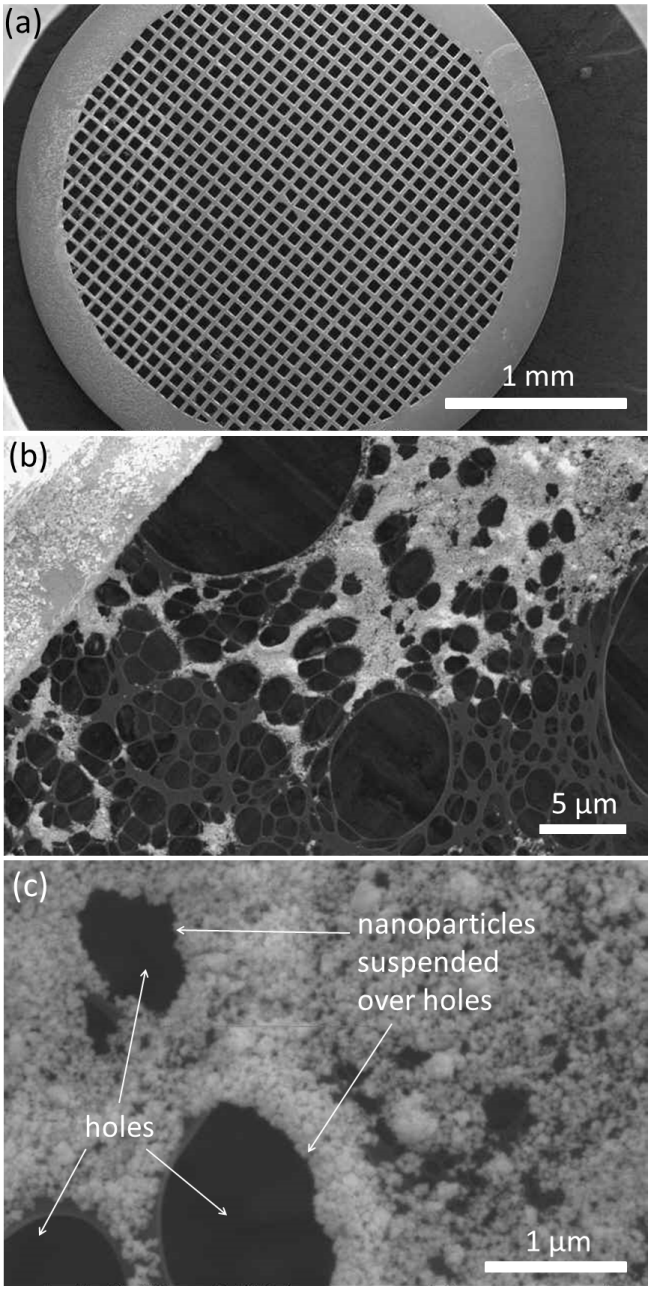

Figure 2.20: Holey SiO TEM grid after dipping in WO_3 nanoparticle solution (10 mg/ml, in de-ionized water, bath sonicated 20 minutes). (a) Whole grid. (b) WO_3 nanoparticles on holey SiO. Grid can be seen in upper left corners. (c) WO_3 nanoparticles on holey SiO. Some nanoparticles are suspended over the holes.

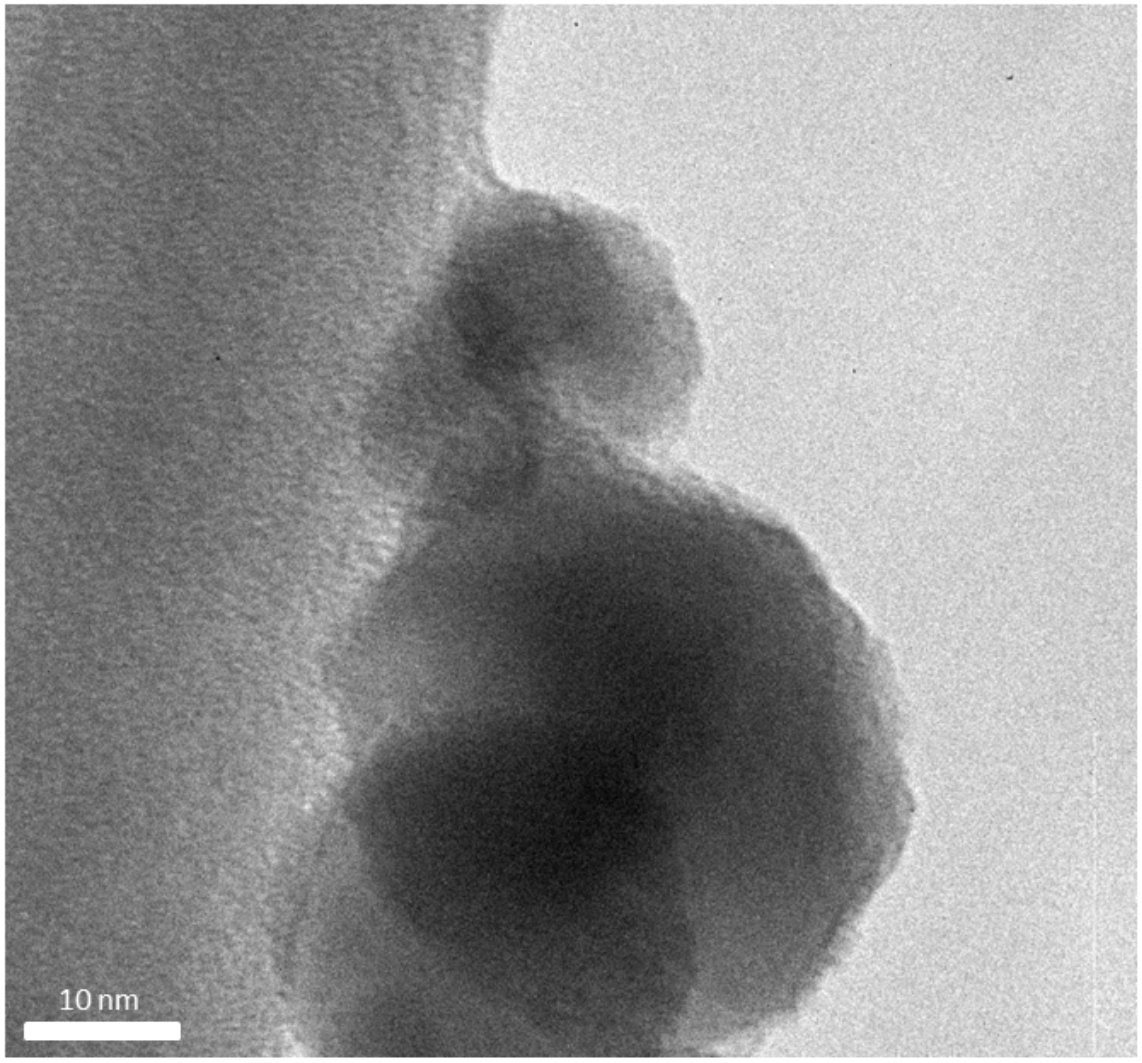

Figure 2.21: TEM image of same sample as Fig. 2.20. Lattice fringes can barely be made out in upper nanoparticle, but for the most part cannot be made out.

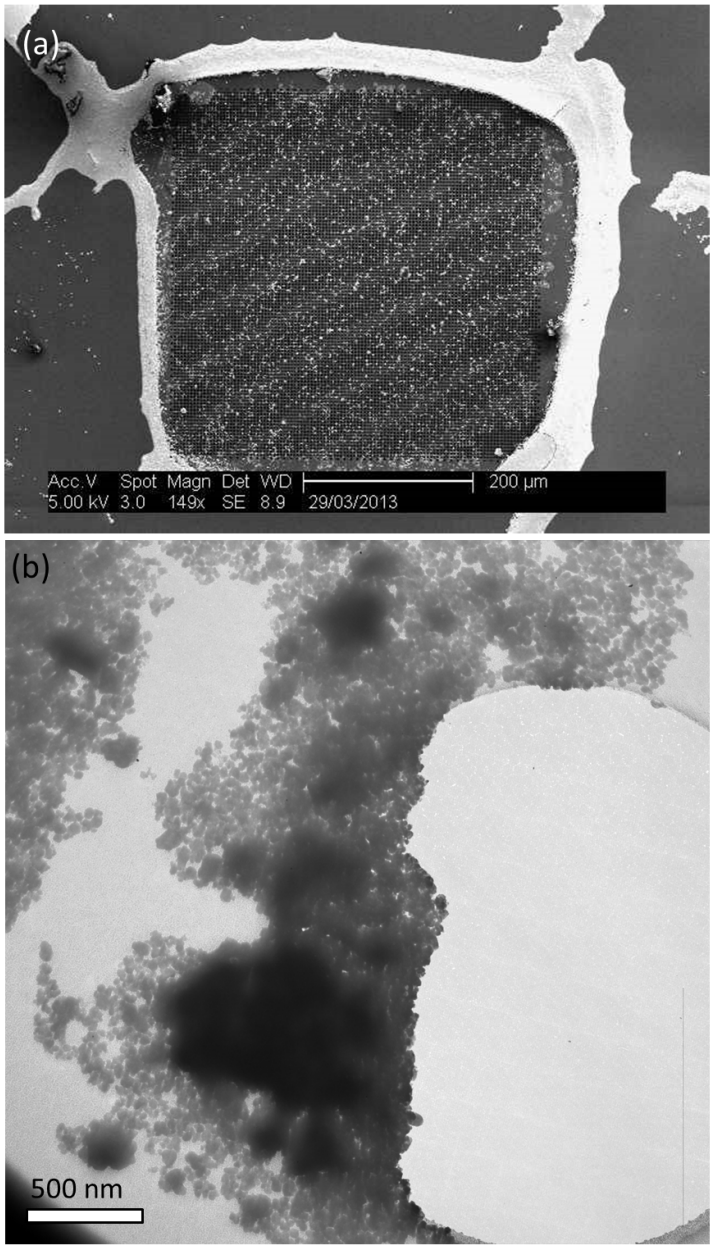

Figure 2.22: SPI Supplies® SiN_x membrane with 50-nm-wide perforated holes, after being dipped in WO_3 nanoparticle solution (10 mg/ml, in de-ionized water, bath sonicated 1 hour). (a) A film of nanoparticles outlines the membrane, and areas of nanoparticles (white) can be seen on the membrane. (b) Nanoparticles partially cover a hole in the SiN_x membrane.

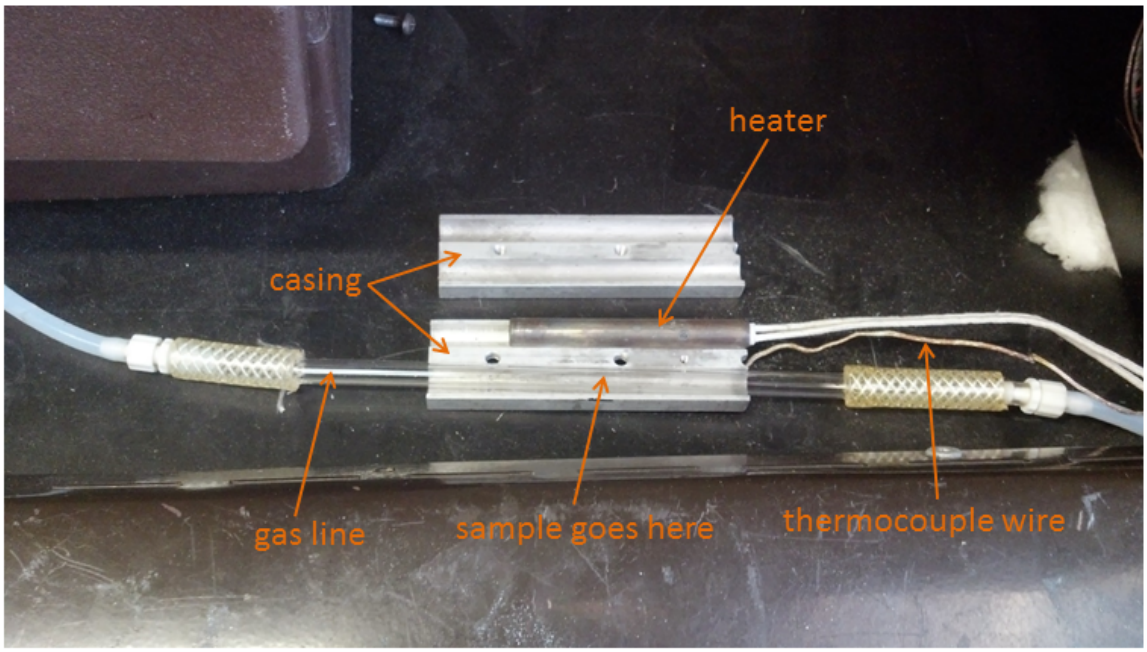

Figure 2.23: A block heater for preparing WO_3 samples for sensing mechanism studies. When in use, the aluminum casing is closed and the apparatus is surrounded by insulation. This apparatus allows the sample to be brought to room temperature in the presence of H_2S.

TEM images of the WO_3 nanoparticles before and after exposure are shown in Fig. 2.24. Though there is some restructuring of surfaces and nanoparticle positions, lattice fringe orientation and spacing appears unchanged. (Differences in the look of the surface are probably due to differences in focus, and not true differences in structure.)

2.5.2.2 X-Ray Photoelectron Spectroscopy

X-ray photoelectron spectroscopy (XPS) is a process in which x-rays are shown on a sample, kicking electrons out of atoms on the surface of a sample. By detecting the kinetic energy of an ejected electron, its original binding energy, and thus the element from which it came, can be determined. Since molecular bonds change electronic binding energies, often the molecular composition of the surface can be determined as well. XPS is a very useful technique for determining the material properties of surfaces. Here we use an Omicron EA 125 to determine the material composition of the WO_3 surface before and after exposure to H_2S.[68, 182]

Materials to be analyzed must be deposited on a substrate. If samples are thin or do not have full coverage of the substrate, a signal from the substrate will be observed during spectroscopy, so the substrate should be chosen so its signal does not interfere with any signals the experimenter hopes to see.[68, 182] For the equipment we used, if insulating materials are thick or on an insulating substrate, they will charge up during spectroscopy, so they must be thin and have sparse coverage and be on a conducting substrate so charge can be removed. For these reasons, we chose a substrate of platinum on a silicon chip. (The silicon chip has a few hundred nanometers of silicon dioxide on it before platinum is deposited.) Platinum was using instead of gold, for example, which forms a gold sulfide as discussed in Section 2.5.6. The platinum was deposited by sputtering with an Anatech Hummer 6.2 Sputter System. In order to reduce the size and density of WO_3 agglomerates (since large ones will charge up under the beam) while keeping coverage high (at least 10% for good signal-to-noise), I used the same technique used to achieve these same goals with In_2O_3 nanoparticles as discussed in Section 2.5.5, but only 50 drops were spincoated (see Fig. 2.25).

Two samples were prepared in the same manner. Both were heated to 300°C and exposed to dry air for 30 minutes using the same procedure as for the samples imaged in the TEM. Then one was exposed to 50 ppm H_2S for 10 minutes. Twenty minutes later, both samples were placed in the XPS.

During XPS, we observed, in both samples, peaks which can be associated with WO_3 and platinum (though in both samples the platinum peaks were shifted to slightly higher energies) and small peaks for water and carbon (impurities). Importantly, there was also a peak for sulfur in a sulfide in the sample exposed to H_2S and no corresponding peak in the sample exposed to only dry air. Also importantly, there was no peak in either for tungsten in tungsten sulfide.

These results rule out the proposed sensing mechanism in Eq. 2.26 that WS_2

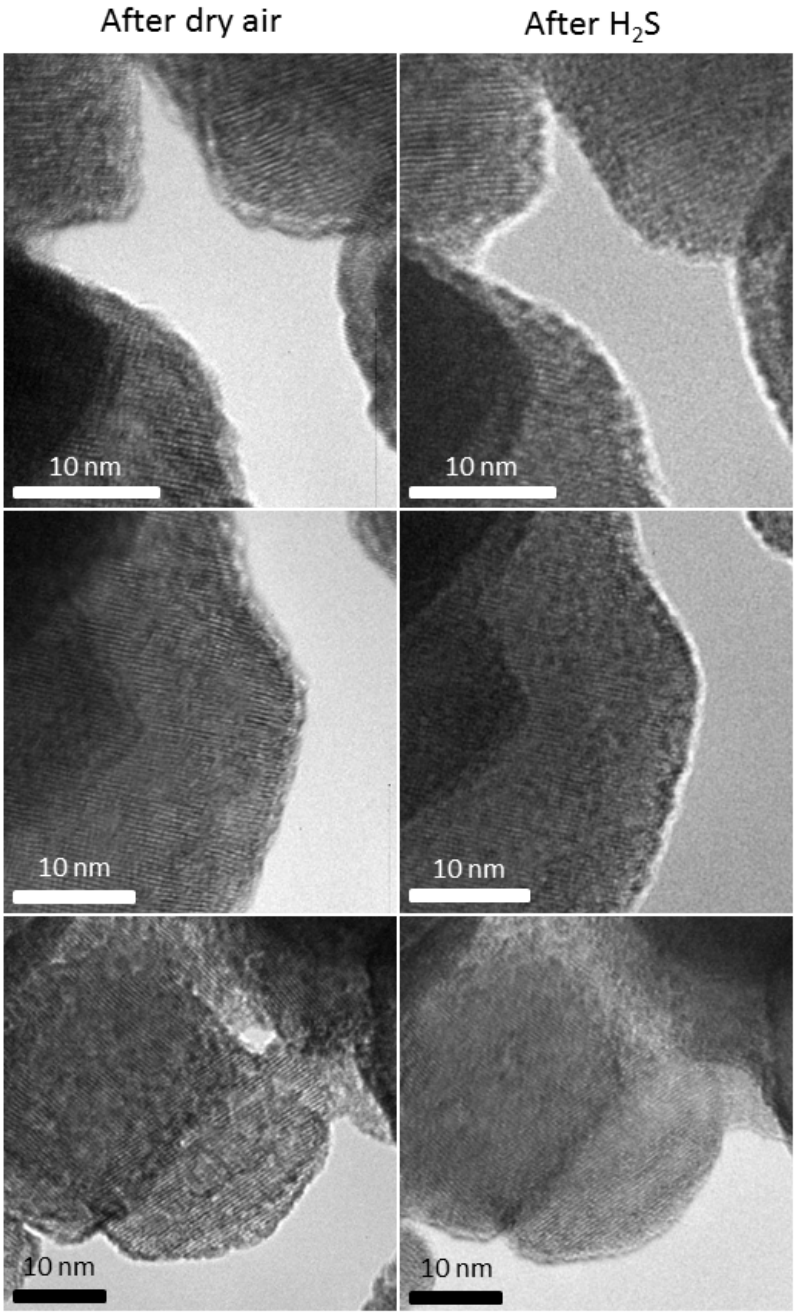

Figure 2.24: Various areas in WO_3 nanoparticle sample after heating to 300°C in dry air (left column) and after heating to 300°C in 50 ppm H_2S (right column)

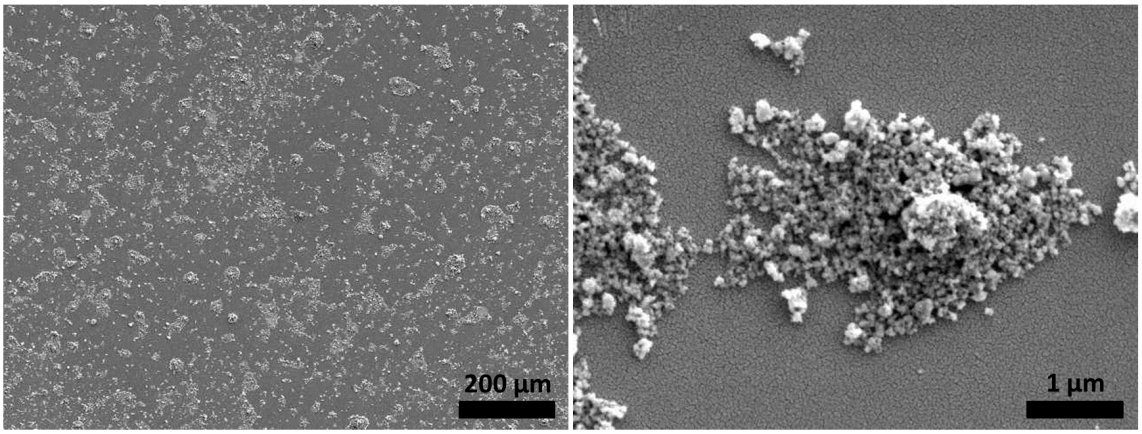

Figure 2.25: SEM images of WO_3 nanoparticles on platinum substrate. Platinum was sputtered on a silicon wafer with 300 nm silicon dioxide on it. We placed WO_3 nanoparticles in de-ionized water at 1 mg/ml, ultrasonicated the solution with a horn for 3 hours, let it sit for 1 hour, then spincoated 50 drops on the substrate at 5000 rpm. (a) Coverage is relatively high. (b) Nanoparticles are mostly less than a few layers.

is forming. Still, these results have a few possible interpretations: (a) H_2S is adsorbing on the WO_3, but irreversibly (even at high temperatures). If this process is occurring, the number of H_2S molecules adsorbed is not a function of the H_2S concentration delivered to the sample, so this process cannot be responsible for the sensing mechanism of WO_3 to H_2S. (b) H_2S is adsorbing on the WO_3, reversibly. If this is the case, this process may be part of the WO_3 sensing mechanism. (c) The platinum is forming a platinum sulfide. If this is the case, this process is obviously not a part of the WO_3 sensing mechanism. (d) Some combination of these.

(a) was ruled out by bringing the sample exposed to H_2S to 300°C and delivering dry air to allow the sample to recover. After this, the sample had no sulfur peak. This shows that the reaction is reversible.

(c) seems unlikely – the x-rays penetrate 10-20 nm into the platinum and the platinum sulfide would only form on the surface of the platinum, so XPS would produce two peaks or a broadened peak if platinum sulfide were forming.

Therefore, (b) is the most likely explanation for our observations – it appears that H_2S adsorbs on WO_3 in a way which is reversible at high temperature. In addition, we have already found that when the WO_3 is exposed to H_2S at high temperature, and H_2S continues to be delivered while lowering the temperature to room temperature, and the WO_3 is then removed from the H_2S, the H_2S comes off much more slowly than when the H_2S stops being delivered to the WO_3 at high temperature. This means that desorption is activated, which is characteristic of chemisorption and not physisorption. It is therefore likely that H_2S chemisorbs on WO_3 during exposure,

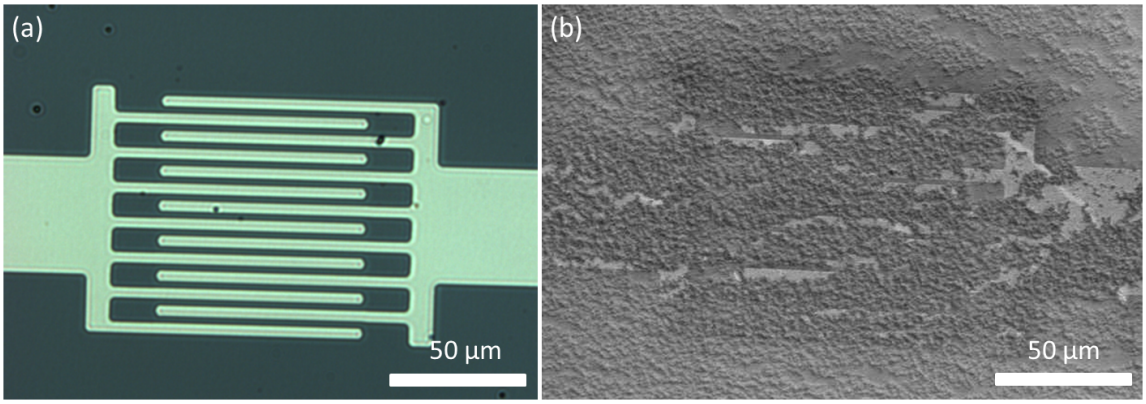

Figure 2.26: Platinum IDEs (a) before and (b) after deposition of Fe_2O_3 nanoparticles.

donating electrons to the WO_3, thus increasing its conductivity and thus taking part in the sensing mechanism of WO_3 to H_2S.

2.5.3 Semiconducting Metal Oxides: Maghemite Nanoparticles

Maghemite is an iron oxide, also known as γ-Fe_2O_3. Some basic information about maghemite was summarized in chapter 1. Maghemite has been studied for gas sensing,[83, 177, 191] but, to this author's knowledge, no studies of maghemite's response to H_2S has been performed.

Maghemite nanoparticles were prepared by Dr. Toby Sainsbury by the method described in van Ewijk, et al.[183] They were charge stabilized in distilled-deionized water, with an average diameter of 9.7 nm.

Five microliters of the solution was dropcast on interdigitated electrodes, as shown in Fig. 2.26. We placed the device at 70°C, delivered dry, filtered air to it, and then exposed it to various concentrations of H_2S for one minute every thirty minutes. Fig. 2.27a shows the smoothed response curves, after re-zeroing their initial times to zero. Responses are extremely slow (no sign of leveling off after the minute), as is expected since semiconducting metal oxides generally need to be at a few hundred degrees Celsius to have reasonable response times. (There are "bumps" in the curves at the beginning and end of each exposure – these may be due to electrical disturbances caused by the opening and closing of valves.) Fig. 2.27b shows the change in conductance of the device over the whole exposure versus the H_2S concentration exposed. The two are directly proportional, as is expected.

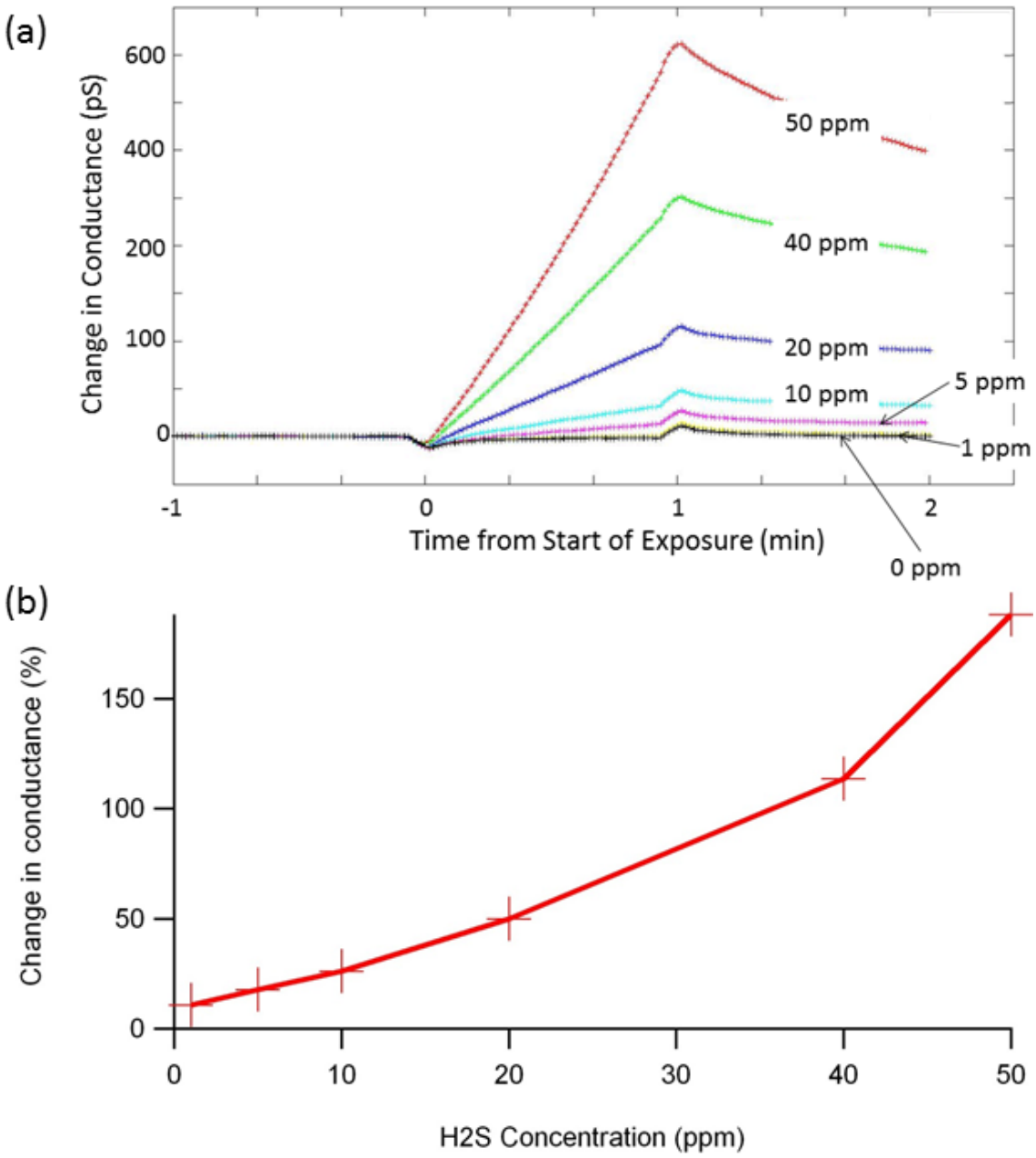

Figure 2.27: (a) Smoothed response curves of Fe_2O_3 nanoparticles at 70°C to various concentrations of H_2S (one minute exposures every 30 minutes). The starting time of each exposure was re-zeroed. (b) Change in conductance over each exposure vs. H_2S concentration exposed.

2.5.4 Semiconducting Metal Oxides: Zinc Oxide Nanoparticles

Zinc oxide (ZnO) is a white powder which occurs naturally in the mineral zincite, though most zinc oxide used today is synthesized via oxidation of zinc vapor.[96, 151] Basic information about zinc oxide was summarized in chapter 1. Zinc oxide has a number of properties that make it potentially useful for sensing, including low electrical noise, high temperature stability, and high breakdown voltage.[26, 62, 91, 115, 190] Additionally, it is tunable – its band gap may be tuned by alloying with MgO or CdO and its doping is tunable by addition of substitutional impurities.[14, 29, 133] With regard to H_2S, zinc oxide is known to react with H_2S in the following way:

$$ZnO + H_2S \longrightarrow ZnS + H_2O \tag{2.34}$$

This reaction is exploited in various applications to remove H_2S from air, for example in cigarette filters.[96, 151]

We made a solution of 1.25 mg/ml zinc oxide (ZnO) nanoparticles in isopropyl alcohol (IPA), then sonicated it for three hours and dropcast five microliters, but found no conductance. We then sonicated it for ten minutes and dropcast another five microliters, still finding no conductance. Lastly, we sonicated it for five minutes and dropcast one microliter, this time finding the network conducting. Keeping the voltage across the device constant, we delivered dry, filtered air, then one minute exposures to various H_2S concentrations every hour at room temperature, as shown in Fig. 2.28b. Similar to the Fe_2O_3, response is slow and directly proportional to H_2S concentration.

2.5.5 Semiconducting Metal Oxides: In_2O_3 Nanoparticles

Nanoparticles with no ligands usually agglomerate over time in solution.[69, 163] Separating these nanoparticles before deposition has a few benefits: (a) If they are not separated and there is only partial coverage of the surface by deposition, these large agglomerates will dominate the device characteristics, but their size and density will vary considerably between devices. Each device will look and behave differently, so each device will need to be considered differently in order to do an in-depth analysis of it. Also, reproducible manufacture is important for applications. (b) These agglomerates make gas diffusion more important in device behavior, since analytes need to diffuse through the outer layers of nanoparticles before adsorbing on inner nanoparticles. This complicates scientific analysis of results and decreases response time. For these reasons, we decided to make an effort to move towards deposition of partial nanoparticle monolayers. (Monolayers are not really necessary as long as there are considerable parallel channels through the nanoparticles between the electrodes.)

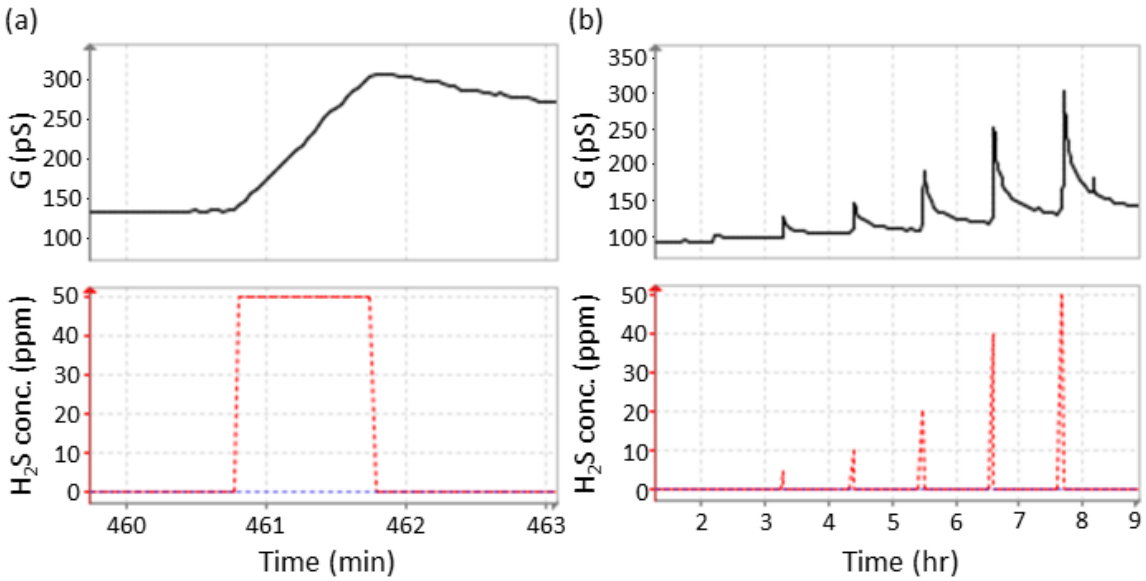

Figure 2.28: Conductance response (top) of ZnO nanoparticle network to (a) a one minute exposure of 50 ppm H_2S and (b) various concentrations of H_2S. Bottom graphs show target H_2S concentration vs. time.

Fig. 2.29 shows a deposition of nanoparticles on SiO_2, before any refinement of deposition method. The In_2O_3 nanoparticles were 99.99% purity and had a diameter distribution of 20-100 nm. They were placed in IPA at a concentration of 2 mg/ml, sonicated in a bath, and deposited immediately after sonication by successively spin-coating ten drops of solution. Notice the large agglomerates and large areas with no coverage. By exploring the parameter space of concentrations, solvent, sonication time and type (bath and ultrasonication with horn), acidity of water, number of drops, and waiting time before deposition, Dennis Wang, under my direction, developed a deposition technique onto SiO_2 that led to coverage much closer to a partial monolayer (1 mg/ml In_2O_3 nanoparticles in acetone, 3 hour horn sonication, with 1 hour waiting time before spincoating of 100 drops at 5000 rpm), as shown in Fig. 2.30a. (The waiting time allows for agglomerates remaining after sonication to settle out.) The same parameters were used to deposit onto IDEs, as shown in Fig. 2.30b.

A few devices were made from these nanoparticles, but response to H_2S was either non-existent or highly erratic. Response to methane was non-existent. Response to humidity, on the other hand, was reasonable, when the device was heated to 185°C using a Kapton® heater (Fig. 2.31). As shown, the humidity response shows no interference from H_2S.

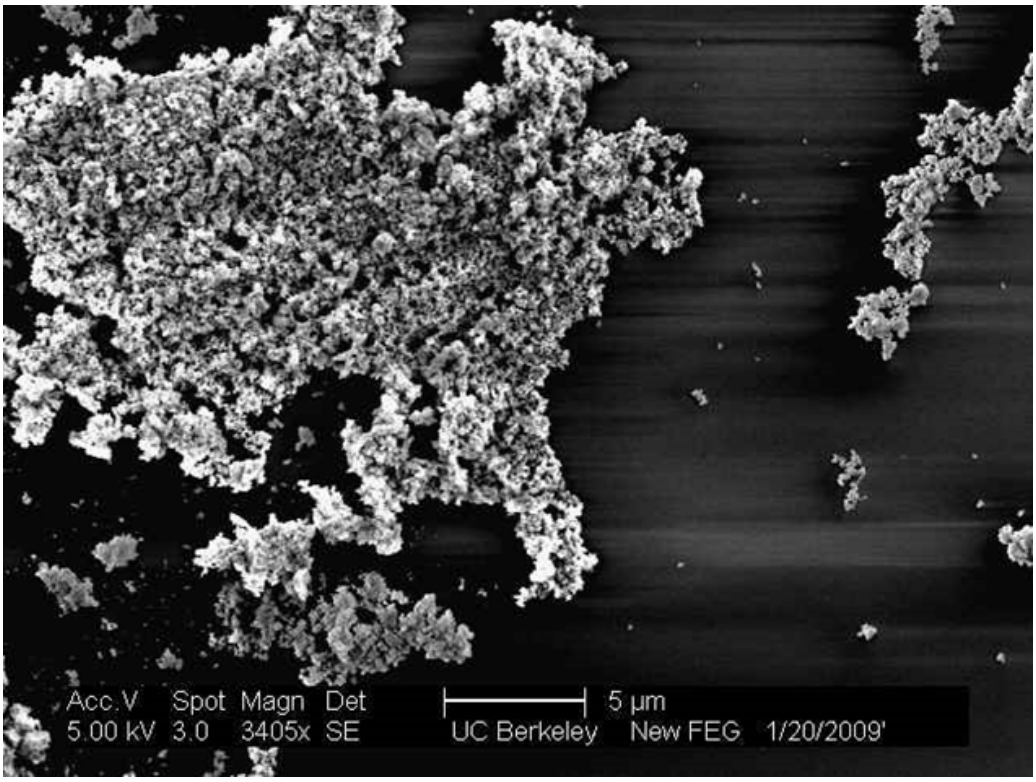

Figure 2.29: In_2O_3 nanoparticles deposited on SiO_2 before refinement of deposition process.

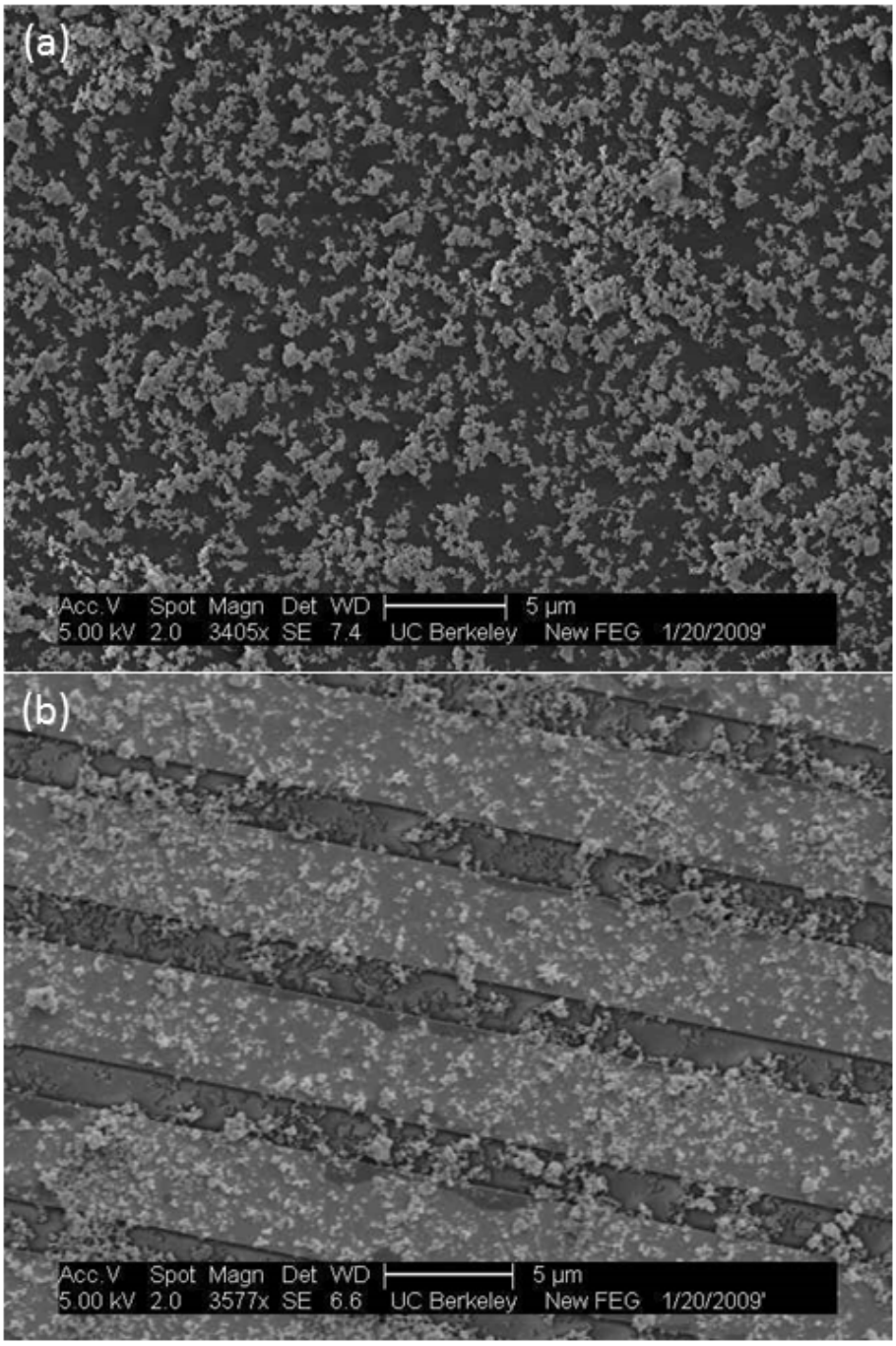

Figure 2.30: In_2O_3 nanoparticles deposited on (a) SiO_2 and (b) IDEs after refinement of deposition process.

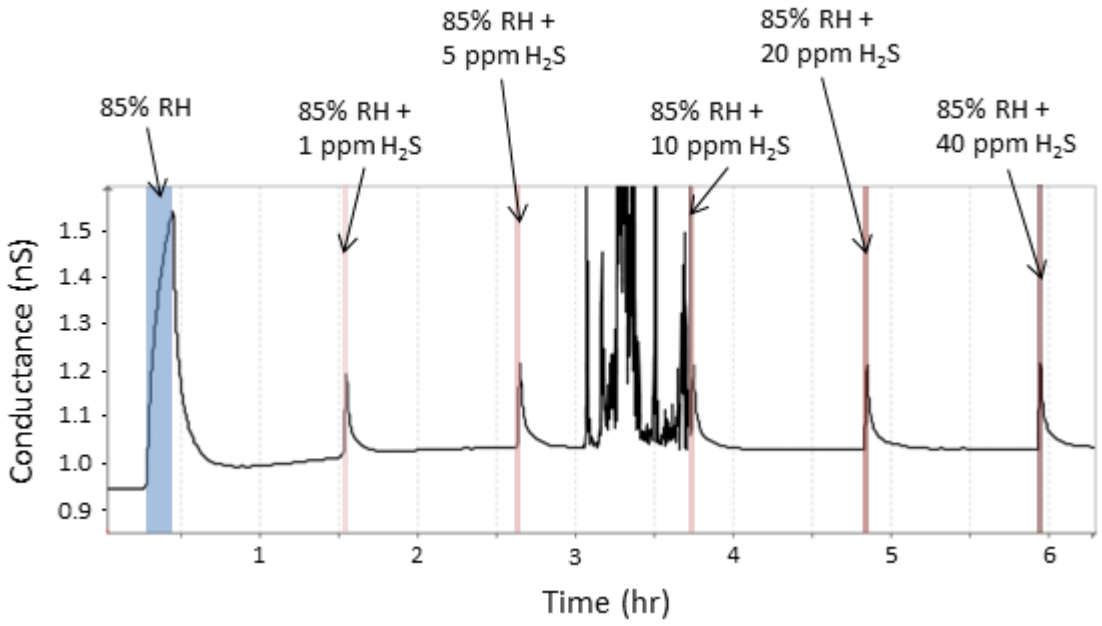

Figure 2.31: Response of a partial monolayer of In_2O_3 nanoparticles on IDEs to humidity and H_2S. Some electrical noise interrupts measurement between 13.5 and 14.3 hours.

2.5.6 Lithographically-Patterned Gold Nanowire

We studied the effects of hydrogen sulfide (H_2S) on lithographically-patterned gold nanowires, as shown in Fig. 2.32. These were 5-nm-thick layers of gold, about 100 nm wide, with a 3-nm-thick sticking layer of chromium. Electrodes (on the left and right sides of the figure) were fabricated by photolithography. The nanowires were then fabricated using standard electron beam lithography techniques. (The size and placement of the rectangles at the electrode-nanowire interface are important. If no rectangles had been patterned at the electrode-nanowire interface, there would be a high probability of lack of contact between the electrode and nanowire, due to the nanowire's thinness. Because, in the electron beam evaporator, the angle between the target and the substrate is constant throughout evaporation and never exactly 90°, if the rectangles had not surrounded the tips of the electrodes, it would be possible for the electrodes and nanowires to not make contact depending on the angle between the target and substrate.)

We placed a constant voltage across the nanowires and observed the change in resistance upon exposure to various gases. As shown in Fig. 2.33, we began by heating the sample to 70°C and delivering dry, filtered air to the sample and then delivered 10 ppm H_2S, which caused the conductance of the nanowire to drop. Further exposures to higher concentrations of H_2S had little effect.

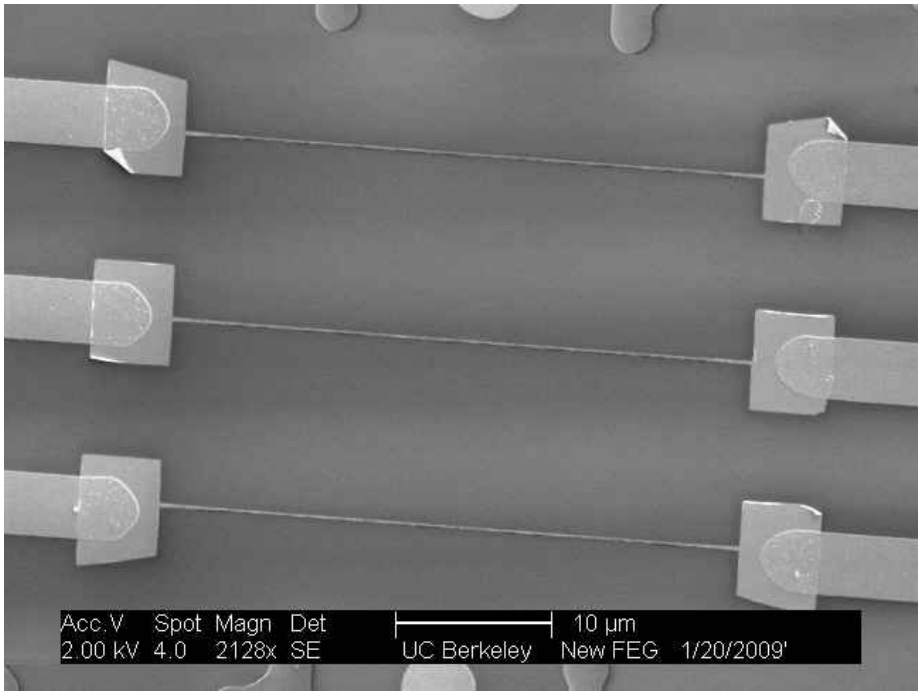

Figure 2.32: SEM image of lithographically-patterned gold nanowires.

Then, using a Kapton heater, we heated the sample (and the entire CERDIP it lay on) to 200°C between exposures, and found that under these conditions the sample recovered and responded to further exposures to H_2S (see Fig. 2.34).

We attribute this behavior to the conversion of gold to gold sulfide (AuS) in the presence of H_2S – the reverse reaction can only occur at elevated temperatures.[203]

$$Au + H_2S \longrightarrow AuS + H_2\uparrow \tag{2.35}$$

$$AuS + O_2 \xrightarrow{\text{heat}} Au + SO_2\uparrow \tag{2.36}$$

We also tested the response of the nanowire to H_2O at 70°C, as shown in Fig. 2.35. We see that the response of nanowire to humidified air alone is negligible, and the response to H_2S is not significantly changed by humidification. These results are consistent with the interpretation that the gold is converted to gold sulfide when exposed to H_2S. (Note that in this case, the nanowire continues to respond to H_2S exposures, but still doesn't recover, which is still consistent with our interpretation of the data.)

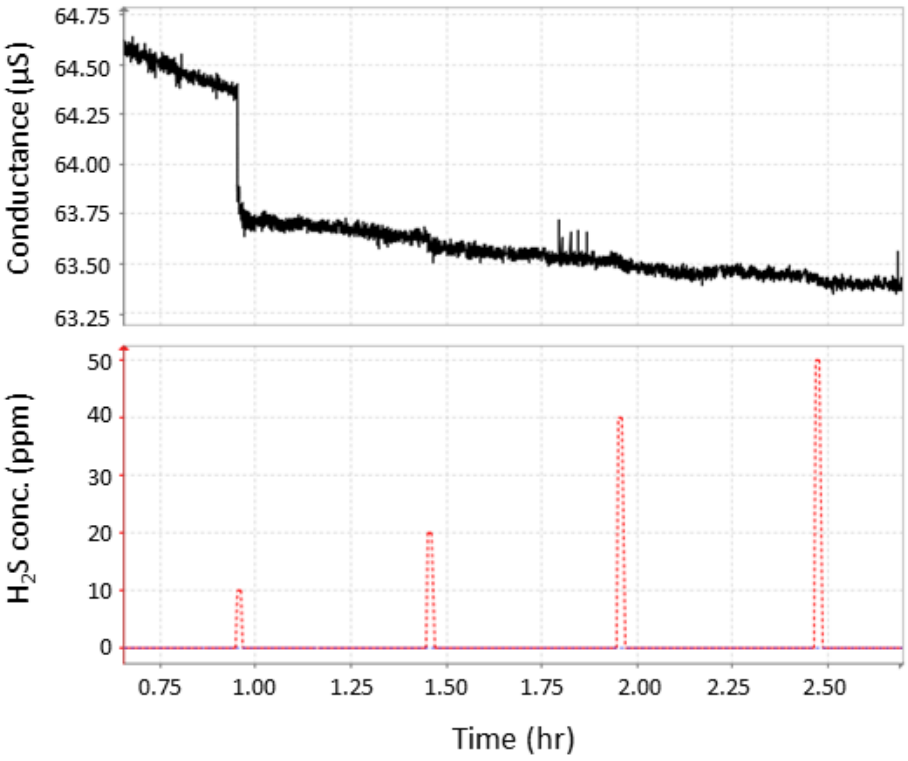

Figure 2.33: Response of lithographically-patterned nanowire to H_2S at 70°C. Bottom graph shows target H_2S concentration as a function of time.

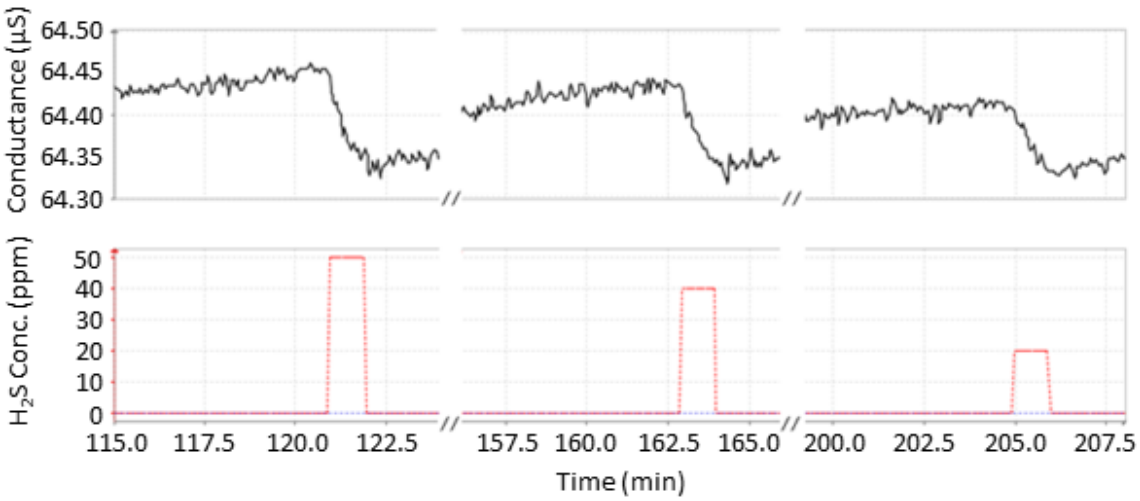

Figure 2.34: Response of lithographically-patterned nanowire to H_2S, when heating to 200°C between exposures. Bottom graph shows target H_2S concentrations as a function of time.

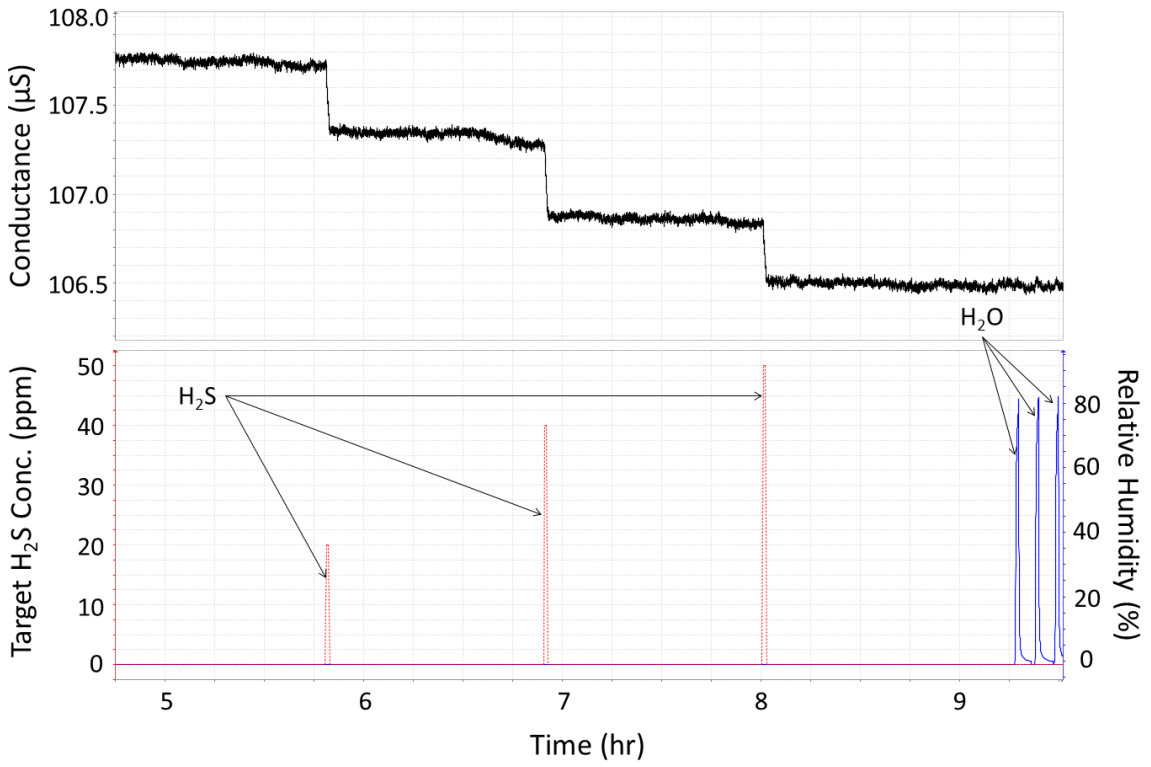

Figure 2.35: Response of lithographically-patterned nanowire to H_2S (red) and H_2O (blue).

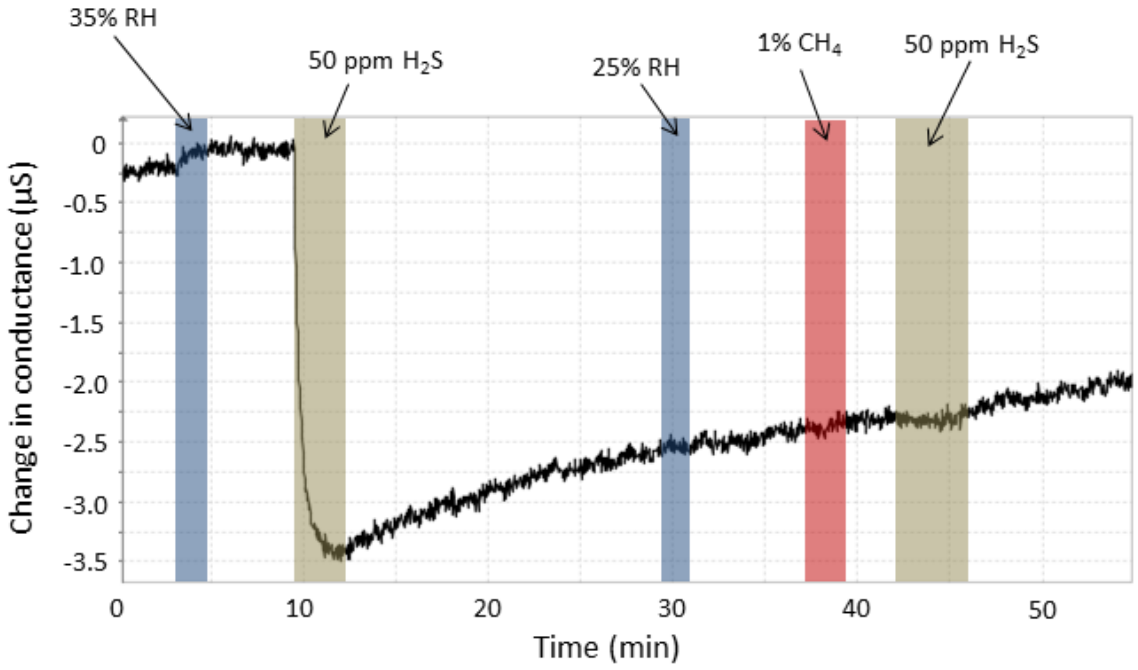

Figure 2.36: Response of "gold line" device to H_2S, H_2O, and CH_4. In the blue regions, the sample is exposed to 35% and 25% relative humidity, from left to right.

2.5.7 Gold Thin Film

As discussed in section 2.4.5, when trying to pattern devices on suspended microhotplates, we ended up with thin lines of gold along the the edge of the microhotplate (see Fig. 2.11). We took one of these "gold line" devices and tested its response under exposure to various gases (see Fig. 2.36). (Device is not shown – there were no patterned devices on this microhotplate.)

As shown in Fig. 2.36, the behavior with respect to H_2S is similar to that of the lithographically-patterned gold nanowire – the device conductance drops during its first exposure to H_2S, and response to subsequent exposures is very small. Similar to the nanowire, the "gold line" response to humidity is negligible. In this test we also exposed the device to 1% methane and found no response, which continues to support the claim that the response of a gold film to H_2S is due to an effect that is selective to H_2S.

2.5.8 Carbon Nanotube Network

2.5.8.1 Theory and Motivation

As discussed previously, graphene is a one-atom-thick sheet of carbon atoms in a hexagonal lattice.[147] Single-walled carbon nanotubes (SWCNTs) can be thought of

as graphene which has been rolled up into a cylinder. Multi-walled carbon nanotubes (MWCNTs) are a number of concentric SWCNTs. SWCNTs are generally around a nanometer in width and can be many microns long. Depending on their chirality (how the graphene is rolled up), they can be either semiconducting or metallic.[187] If one of the SWCNTs in a MWCNT is metallic, the whole MWCNT is metallic, so statistically MWCNTs are usually metallic.

SWCNTs have all their atoms exposed to the environment and can have incredibly high aspect ratios, making them extremely sensitive to gas exposures.[2, 47, 116, 139] Semiconducting CNTs, in particular, are much more electronically sensitive to gases than metallic CNTs due to their much lower carrier concentrations.[122]

Gases adsorb on CNTs both physically (e.g. carbon dioxide, oxygen) and chemically (e.g. ammonia adsorbs both physically and chemically).[120] Goldoni et al.[55] have found that some gases (oxygen, water, nitrogen) interact mainly with contaminants (e.g. Na, Ni) in the CNTs. When these contaminants are removed, the CNTs are no longer sensitive to these gases, leading the authors to conjecture that the gases only interact with pure CNTs via dispersion forces.

Gases can affect the conductivity of a CNT in two ways: (a) via charge transfer from the analyte to the nanotube. A semiconducting SWCNT is p-type in ambient air, so chemisorption of an electron-accepting analyte increases conductivity and chemisorption of an electron-donating analyte decreases it; (b) the adsorbed gas molecule can act as a scattering potential.[122]

In practice it is much easier to measure the conductance of a CNT network than a single CNT. Though the response of a single CNT is due to the two mechanisms given above, the response of the CNT network as a whole may be dominated by other effects. Li et al.[111] theorize that when SWCNTs are exposed to non-polar molecules, adsorption at the interstitial spaces forms SWNT-molecule-SWNT junctions which leads to intertube charge transfer and modulation of intertube transport. Varghese et al.[184] found an impedance change upon exposure of CNTs to humidity, ammonia, carbon monoxide, and carbon dioxide. They attribute this to the modulation of Schottky barriers between metallic and semiconducting CNTs.

The sensing mechanism of CNTs to various gases is obviously still in debate, and the purpose of this study was to try to shed light on this question.

2.5.8.2 Device

A device like the one tested is shown in Fig. 2.37. The device was fabricated by Nanomix, Inc. It consists of a network of SWCNTs, with IDEs patterned on top of it.

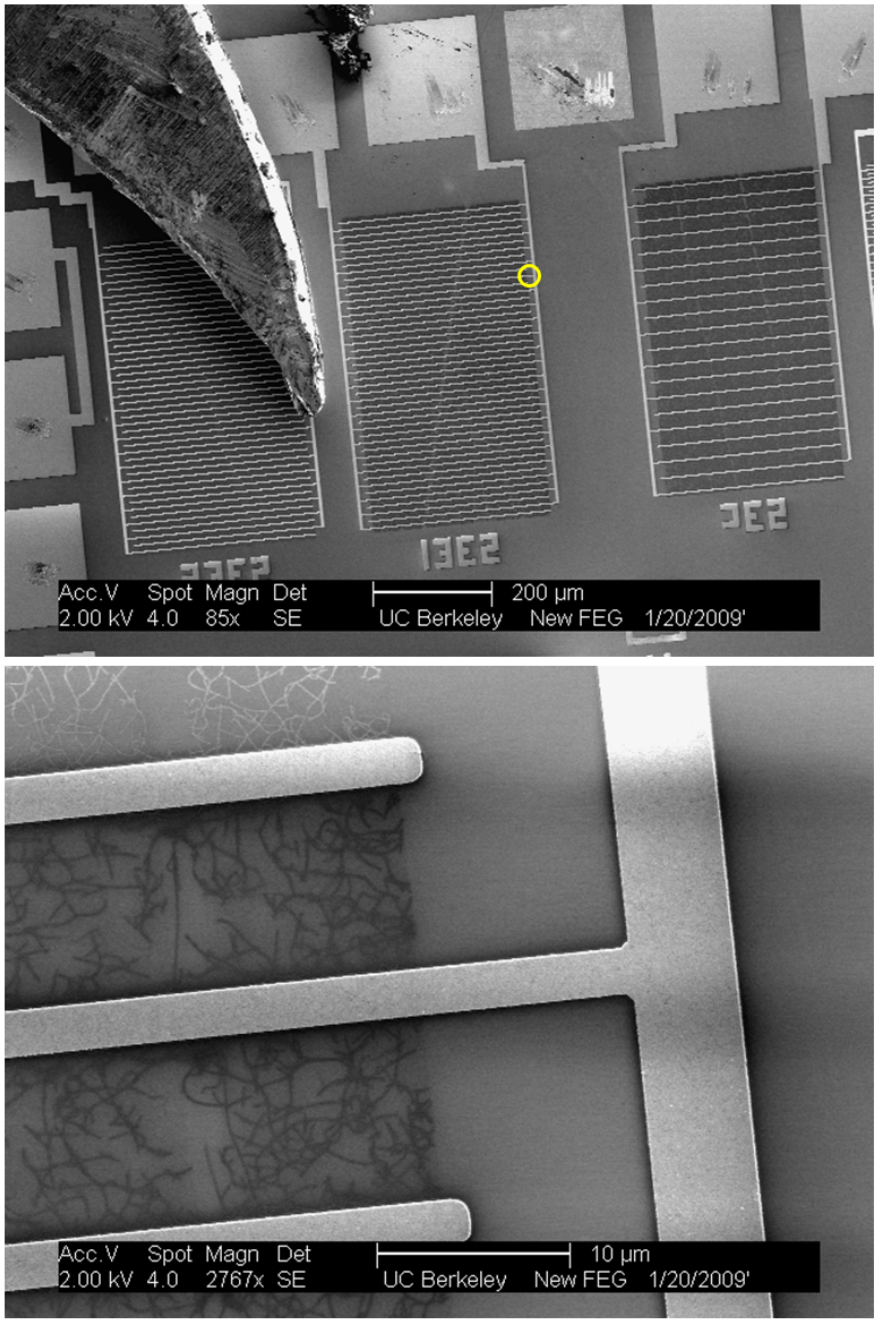

Figure 2.37: A device like that tested. (a) Device 23E1 (labels are upside-down in figure) is a CNT network with IDEs patterned on top of it. (b) A close up of the circled area in (a).

2.5.8.3 Results

We gated the device, and, with the electrodes at a constant voltage difference, swept the gate voltage, recording the current across the device at various gate voltages, obtaining the curves shown in Fig. 2.38a. The red curve was recorded before exposure to H_2S, the blue curve just after exposure to H_2S. Notice that the during-exposure curve seems to be shifted left with respect to the pre-exposure curve, which indicates that the number of charge carriers in the CNT network decreased upon exposure to H_2S. Since SWCNTs are p-type in air, the H_2S is donating electrons to the CNTs. This makes sense since H_2S tends to be electron-donating.

We also tested the response to humidified air, at approximately 90% relative humidity at 70°C, as shown in Fig. 2.38b. Notice that the presence of water vapor shifts the IVg downward and increases hysteresis. The increase of hysteresis by the presence of water vapor is commonly reported.[122]

2.5.9 Bare Graphene

As discussed previously, graphene is a single-atom-thick sheet of carbon atoms in a hexagonal lattice. Much research has been devoted to graphene in recent years due to its many interesting fundamental properties and potential applications.[6, 24, 52, 53, 108, 142, 146, 207] An understanding of graphene's response to various gases is interesting as a study of fundamental physics, and is also relevant to its potential use in various applications, particularly sensing, one of the many exciting fields of graphene research.[37, 64, 157, 162, 209]

Graphene was grown by chemical vapor deposition (CVD) on copper film and transfered onto a silicon chip (with a 300-nm thick layer of silicon dioxide on it) using standard techniques.[156] 30-nm-thick gold electrodes were electron-beam evaporated using a simple shadow mask of aluminum foil to mask the chip edges and 5 mil wire to create the electrode gap (see Fig. 2.39). The device was wirebonded and placed in the gas delivery system.

50 mV was placed across the device and it was placed at 70°C and exposed to dry, filtered air, then various concentrations of H_2S for one minute, as shown in Fig. 2.40. As shown, the conductance decreased when exposed to H_2S. Similar to the carbon nanotubes, this is probably due to charge donation from the H_2S to the graphene.

2.5.10 Graphene with Au Nanoparticles Deposited by Electroless Deposition

This work was discussed in large part in Gutes, et al.[64] I performed gas sensing experiments.

In many cases, to fabricate graphene-based sensors, graphene is initially decorated with metal nanoparticles to increase its sensitivity, selectivity, limit of detection, or

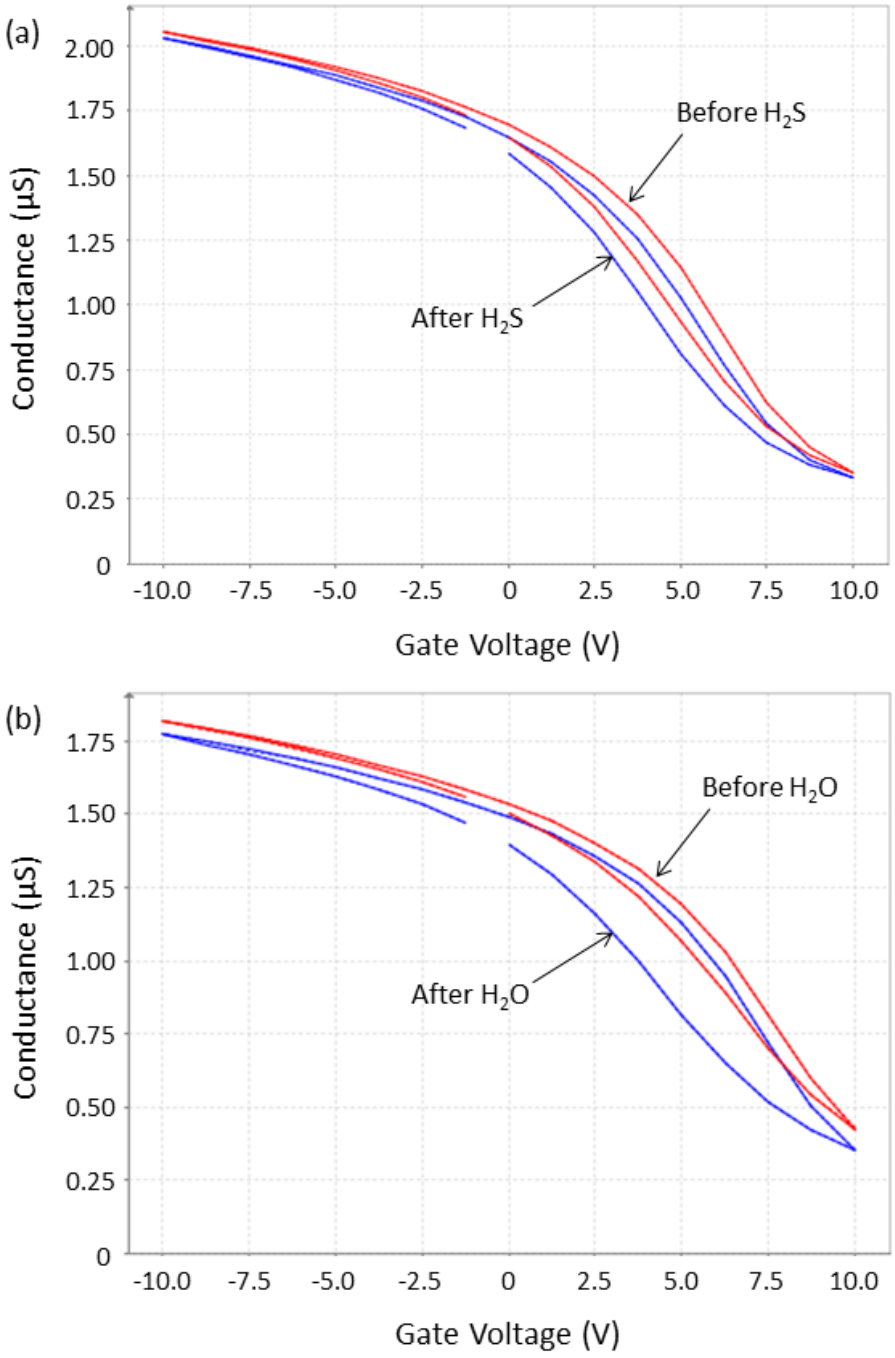

Figure 2.38: Current vs. gate voltage curves of CNT network before and directly after exposure to (a) 200 ppm H_2S and (b) 90% relative humidity.

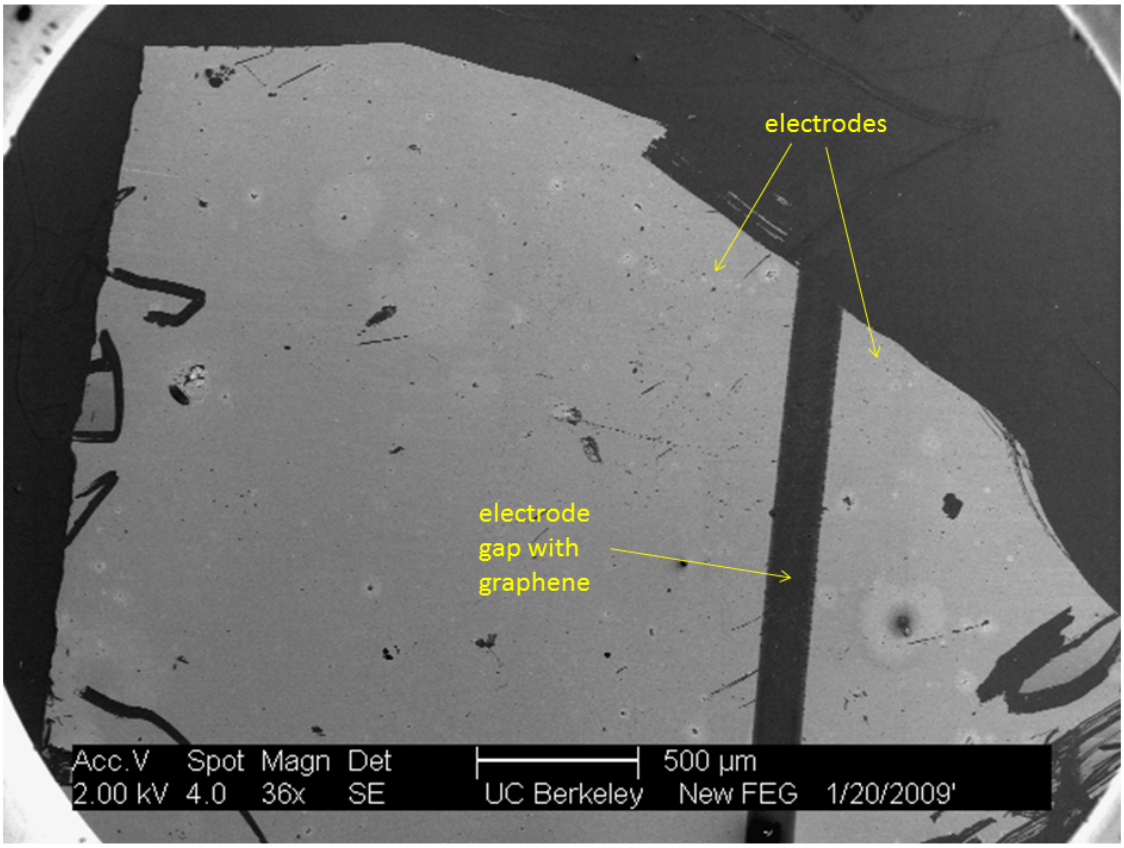

Figure 2.39: SEM image of CVD-grown graphene with electron-beam evaporated electrodes.

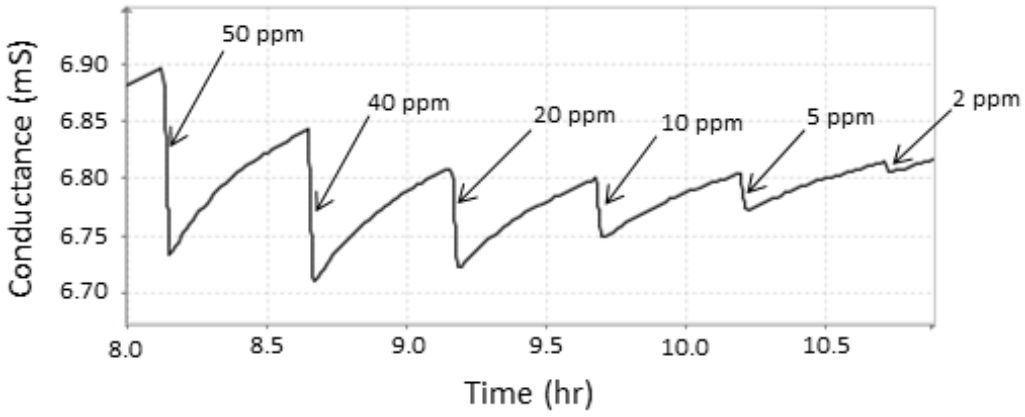

Figure 2.40: Response of CVD-grown graphene to various concentrations of H_2S.

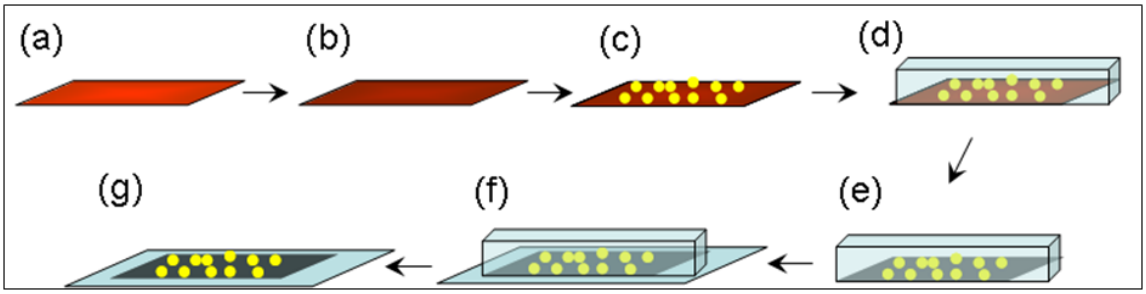

Figure 2.41: Schematic diagram of the graphene growth, decoration and transfer processes. From a copper foil (a) graphene is grown by CVD (b). Electroless deposition of a noble metal is performed (c) and PMMA is applied by spin-coating (d). Copper is etched by a $FeCl_3$ dissolution (e) and after rinsing PMMA/graphene is transferred onto the sensing transducer (f) with a final PMMA dissolution in acetone (g). (Courtesy of Ben Hsia.)

a combination of these properties. In most cases the decoration process is performed by electrochemical reduction of metal salts with the help of external power sources for the reduction of the metal ions using graphene flakes obtained from graphene oxide.[121, 175] The transfer process is then performed by drop-casting of the dispersed graphene flakes on top of the transducer platform, a method that does not allow control over the complete coverage of the surface, homogeneous layer formation or reproducibility of the coverage from sensor to sensor.

We developed a simple and easy-to-implement method to decorate graphene, grown via CVD on copper substrate,[113] by electroless deposition of the metal using the copper as the oxidizing agent. Various metals, including gold, palladium, and platinum were deposited in this way. After the electroless deposition, the decorated graphene was transferred by spin coating with polymethylmethacrylate (PMMA) and copper etching process similar to the one described previously by Reina et al.[156] Figure 2.41 shows the complete process, including the graphene growth, decoration, and transfer.

Figure 2.42 shows SEM images of graphene on Cu substrate before (a) and after the electroless deposition of gold (b), platinum (c) and palladium (d). The particular conditions for the three depositions were in all cases a 1mM dissolution of the corresponding metal salts ($KAuCl_4$, K_2PtCl_4 and K_2PdCl_4 respectively, Sigma Aldrich) and an immersion time of 60 seconds. It is interesting that under the same experimental conditions, the three metals behave differently. Platinum forms smaller nanoparticles with a lower density while gold and palladium tend to present similar reactivities with higher nanoparticle densities and diameters when compared to platinum.

Raman spectroscopy was also preformed on the metal nanoparticles and graphene. Figure 2.43 shows the Raman spectra of graphene on copper before the electroless

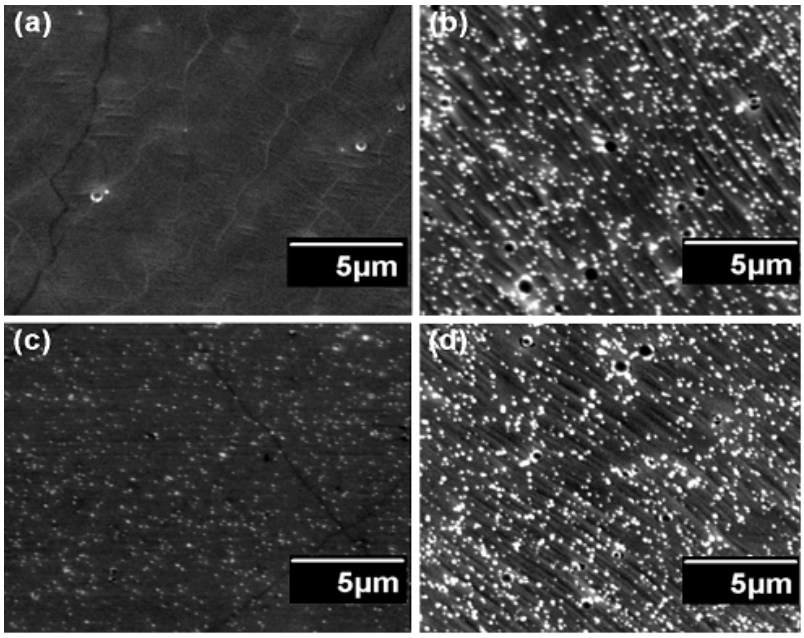

Figure 2.42: SEM images of graphene on copper before (a) and after a 60 seconds immersion time in a 1mM dissolution of $KAuCl_4$ (b), K_2PtCl_4 (c) and K_2PdCl_4 (d). Lines along the surfaces correspond to copper substrate flattening process during manufacturing. (Courtesy of Dr. Albert Gutes.)

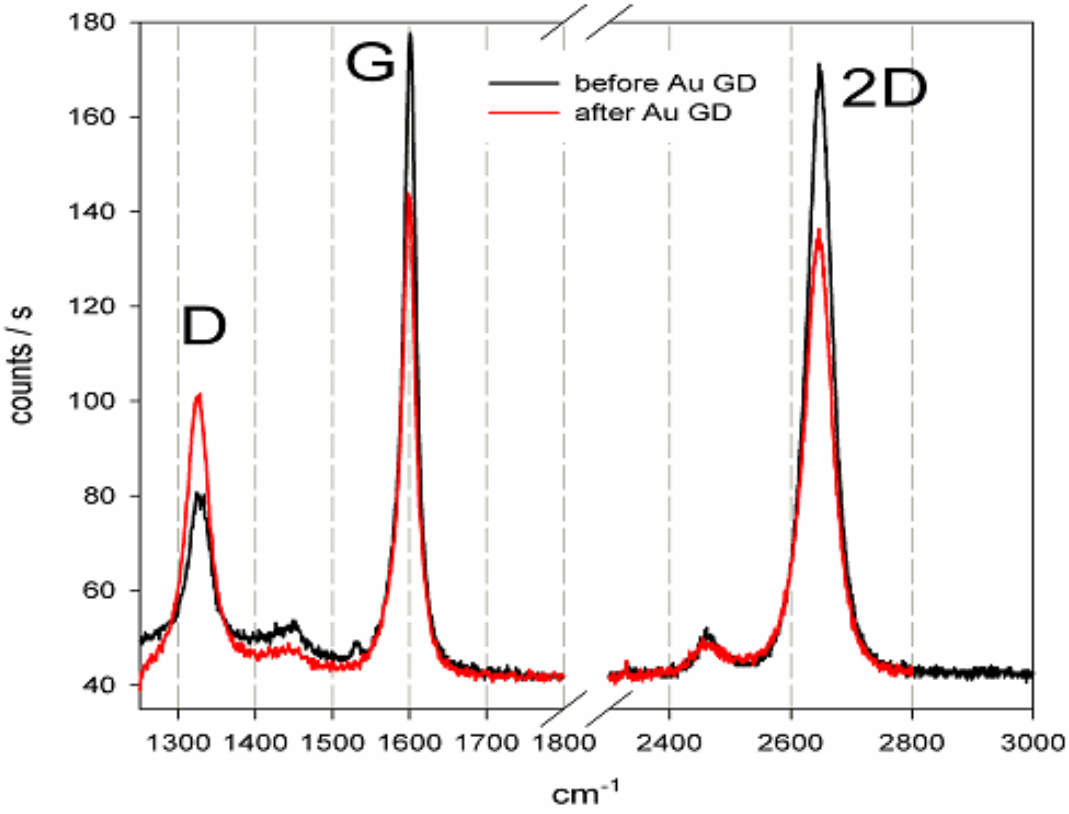

Figure 2.43: Raman spectra obtained on graphene on Cu before (black line) and after an immersion in a 1mM $KAuCl_4$ dissolution for 60 seconds. (Courtesy of Dr. Albert Gutes.)

deposition of gold (black line) and after an immersion of 60 seconds in a 1mM of $KAuCl_4$ (red line). As can be observed the G to D peak ratio decreases substantially, pointing out increased defects in the graphene structure during the metal deposition, caused by the interaction of the metal with the graphene lattice.

We fabricated a device we could use to characterize the graphene/metal nanoparticle system's electrical response to gases. A 5 x 5 mm Au decorated graphene sheet was transferred using the PMMA stamping method onto a transducer consisting of two opposing gold comb-shaped electrodes of 25 m width, separated by a 25 m gap. Figure 2.44a shows the schematic fabrication of the platform while Figure 2.44b shows the SEM image of the obtained electrodes. Raman spectroscopy was performed after the transfer to ensure the complete removal of PMMA and to verify the quality of the transferred graphene. Because of the known interaction of gold with hydrogen sulfide, this gas was used as test molecule.

The device was exposed to varying concentrations of H_2S for 60 seconds every 30 minutes while applying a 50 mV source-drain bias. Figure 2.45 shows the response

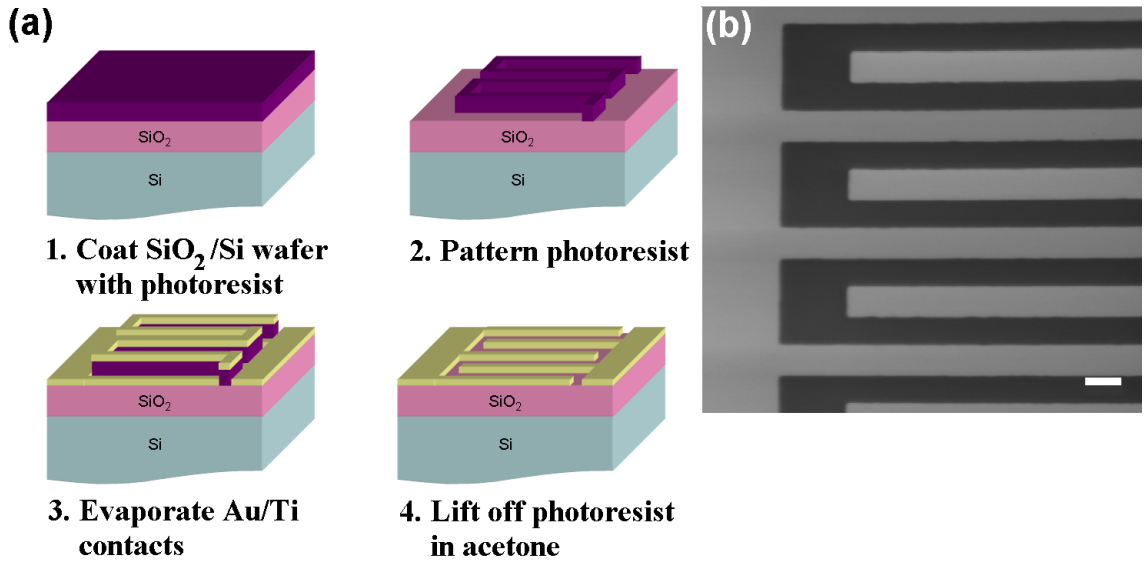

Figure 2.44: (a) Schematic fabrication of the Au-comb electrode. (Courtesy of Ben Hsia.) (b) SEM image of the fabricated device. Scale bar correspond to 25 microns. (Courtesy of Dr. Albert Gutes.)

(in red) in terms of change in conductivity obtained during introduction of varied H_2S concentrations (in black) into the flow cell. As can be observed the response of the device is relatively slow and also not reversible due to the formation of strong S - Au bonds.

These results demonstrate the possibility of using a simple approach to develop new transducing materials for sensing applications. In this particular case, for the determination of H_2S, we believe that the integration of a microheater that could facilitate the desorption of the bonded H_2S-derived species could help in the recovery of the sensor's baseline.

Because of the simplicity in the decoration process we believe that the proposed method could be easily integrated into the already existing roll-to-roll fabrication methods,[5] allowing the mass production of sensing devices. In addition, future works could combine the developed substrates with the integration of biomolecules and biomarkers towards the development of electrochemical biosensors.

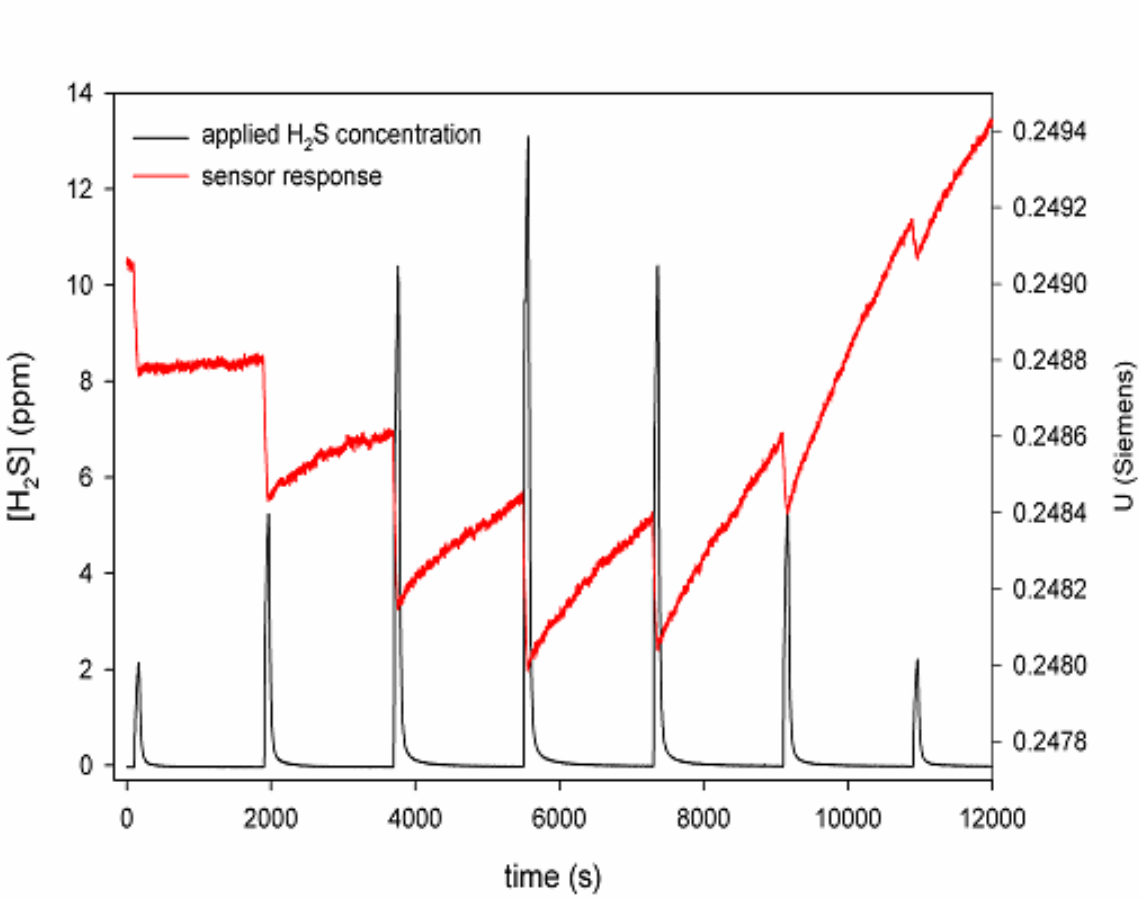

Figure 2.45: Au-decorated graphene sensor response (red line) during an H_2S exposure profile (black line). (Data taken by me. Image constructed by Dr. Albert Gutes.)

Chapter 3

Carbon Nanotube Oscillator

3.1 Introduction

The following work was performed in collaboration with Prof. Jeffrey Weldon, Dr. Benjamin Aleman, and Dr. William Gannett, and was published in large part in Weldon, et al.[195]

Nanoelectromechanical systems[36] (NEMS) which are based on vibrating mechanical elements have demonstrated excellent performance for many applications including chemical sensing,[112, 186, 189] mass sensing,[78] and high frequency signal generation.[48] Although the mechanical element in these systems is nanoscale, large external components, such as high frequency signal sources,[124, 181] amplifiers, and integrated circuits,[48] are necessary to drive the oscillations. To actualize true nanoscale integrated systems, such components need to be mostly eliminated. Here, I report on the achievement of controllable self-oscillations in isolated, singly-clamped field-emitting carbon nanotubes (CNTs) driven only by a single DC bias voltage. A model is developed which correctly predicts the onset of self-oscillations as a function of device geometry and material properties. Using this model, we design and fabricate top-down low voltage self-oscillating NEMS devices which are suitable for large-scale integration.

By definition, passive resonators need high-frequency sources to drive their oscillations. Active oscillators do not require such a source, but they do need active feedback circuitry to achieve oscillations. In the case of resonant NEMS devices, the desired size and power benefits are invariably offset by the bulky control electronics required for oscillation. Some self-oscillation approaches have been explored.[42, 48, 166] Recent observations of oscillations in nanowires[3] are encouraging, but unfortunately there is neither a clear understanding of the underlying drive mechanism nor the required geometry to enable reliable, self-oscillation-based NEMS devices. Here, we elucidate the required geometry for NEMS self-oscillators, and our quantitative model establishes comprehensive design parameters for scalable devices.

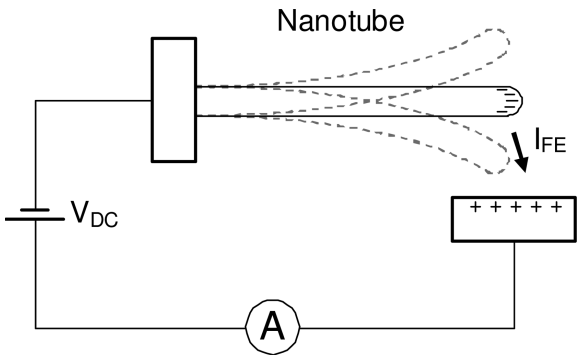

Figure 3.1: Schematic of setup used for testing self-oscillations in carbon nanotubes. We apply a DC bias voltage between the nanotube and counter electrode, which causes field emission from the nanotube to the counter electrode. We use an ammeter to measure the field emission current. (Courtesy of Dr. Jeff Weldon.)

3.2 Observed Phenomenon

We employ a singly-clamped cantilevered field-emitting[3, 78, 79] carbon nanotube as a prototypical oscillator, as shown schematically in Fig. 3.1. When a sufficiently high DC bias is applied between the nanotube and a nearby counter electrode, self-oscillations begin. Of critical importance in achieving reliable self-oscillations is the angle between the longitudinal axis of the nanotube and the counter electrode – a nanotube oriented parallel to the surface can self-oscillate while one oriented perpendicular to the surface cannot. A transmission electron microscope (TEM) image of a multi-walled carbon nanotube (MWCNT) connected to a conducting atomic force microscope tip with orientation parallel to an electrode surface is shown in Fig. 3.2. As the bias voltage is increased from zero the nanotube bends toward the counter electrode (Figs. 3.2a,b) and field emission occurs.[51, 56] Subsequent increases in the bias voltage result in an increase in the field emission current ($\sim 0.1 - 1$ μA) and above a critical, device-specific onset voltage V_o, sustained self-oscillations begin. Fig. 3.2c shows a TEM image of a vibrating nanotube biased past V_o into the continuous self-oscillation mode. Due to the high frequency of the vibrations ($\sim$ 4 MHz), the nanotube is blurred and only the oscillation envelope (highlighted for clarity) is observable. (A movie displaying the onset of sustained self-oscillations can be found in the supplementary information of Weldon, et al.[195]) A plot of field emission current and voltage vs. time for the same device driven through V_o (= 65 V) is shown in Fig. 3.2d. These data illustrate an important and consistent observation in our experiments: the onset of self-oscillations coincides with a spike in current at V_o. Note that the data of Fig. 3.2d were taken at a low sampling rate; the response signal is therefore coarse-grained and does not directly reflect the oscillatory response for $V > Vo$.

First, we examine the fundamental mechanism of self-oscillations in cantilevered,

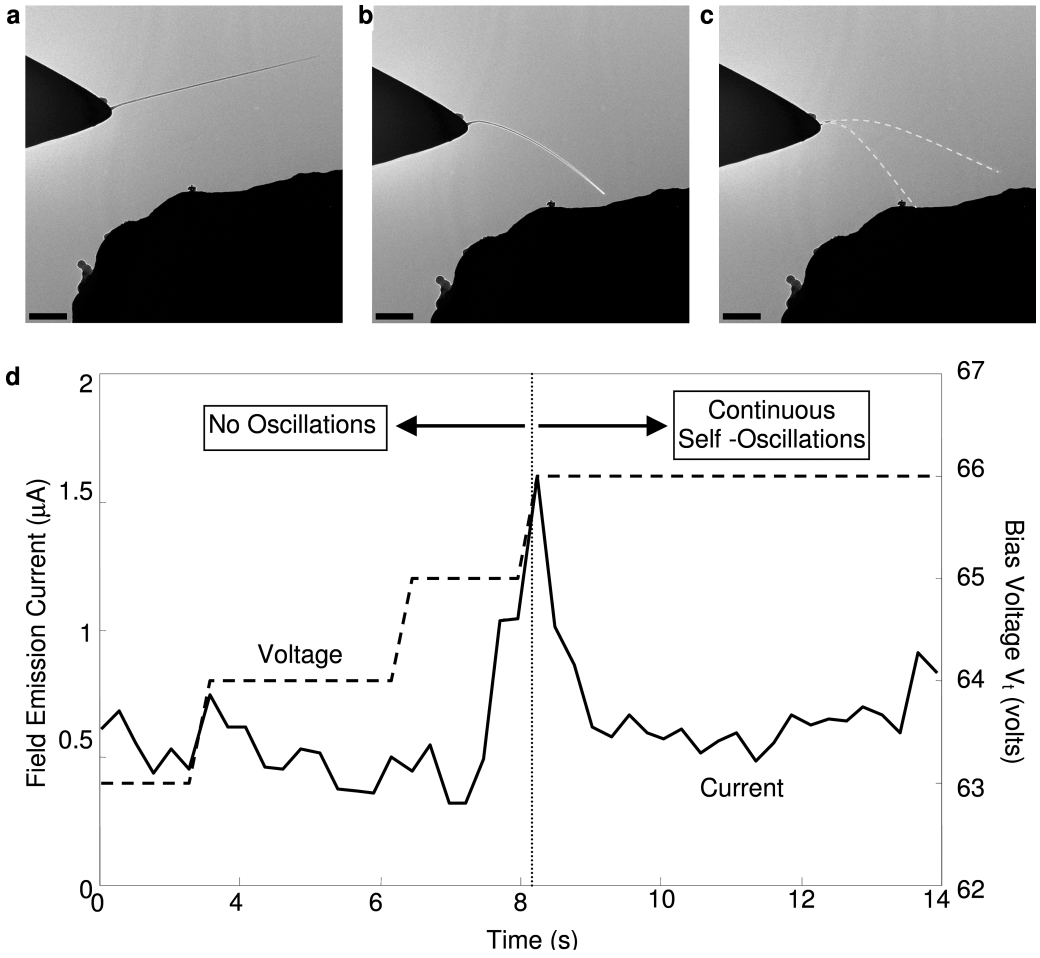

Figure 3.2: TEM images and experimental data during self-oscillation experiments. a) A TEM image of the nanotube at zero bias (scale bar is 0.2 μm). The nanotube is about 2.8 μm long and 2.8 μm from the counter electrode. b) A TEM image of the biased nanotube. The nanotube is charged so the electrostatic force draws the nanotube toward the counter electrode. c) A TEM image of a self-oscillating nanotube. The nanotube is not easily visible while it is vibrating; dashed lines, which delineate the vibration amplitude, have been added for clarity. Though the nanotube seems to contact the counter electrode, it does not. The vibration plane is behind the visible edge of the counter electrode. d) The field emission current and applied bias as a function of time. The nanotube begins sustained self-oscillations at 66 V. The start of continuous self-oscillations coincides with a large current spike. (Courtesy of Dr. Benji Aleman and Dr. Jeff Weldon.)

field-emitting tubular nanostructures. Then we develop a detailed model which accounts for nanotube and electrode geometry. Using the model's predictive power, we design and fabricate, by a top-down approach, scalable NEMS self-oscillation devices with engineered oscillation frequency and turn-on voltage.

3.3 Theoretical Description

3.3.1 Overview

The nature of the self-oscillations can be qualitatively understood by examining the forces on the nanotube and the effect the forces have on the field emission current. When the nanotube bias is below V_0 it is pulled towards the counter electrode by the electrostatic force resulting from charge accumulations on the nanotube and the counterelectrode. This attractive force is balanced by the repulsive mechanical restoring force of the bent nanotube cantilever. As is observed experimentally, vibrations begin when a burst of electrons discharges from the nanotube. The rapid discharge temporarily diminishes the attractive electrostatic force and, as the result, the mechanical restoring force suddenly dominates. Because of the significant resistance and capacitance of the system, there is a time delay in recharging the nanotube, and thus the nanotube is quickly pulled away from the counter electrode. The step-like forcing function initiates nanotube mechanical vibrations. The rapid discharge of electrons is analogous to the plucking of a guitar string. However, in the case of the nanotube, the vibrations are sustained indefinitely because the cycle of rapid discharge and repulsion (i.e. the plucking) repeats itself, much like the continuous strumming of a guitar string.

3.3.2 The Origin of the Current Spike

We now take a closer look at field emission from cantilevered and mechanically flexed nanotubes. This serves to explain the origin of the current spike which initiates self-oscillations and allows us, based on geometrical device parameters alone, to predict the onset voltage for self-oscillations. Field emission occurs when electrons tunnel through the potential barrier near an object's surface into nearby vacuum.[51, 56] The tunneling current is greatly enhanced in one-dimensional structures, such as nanotubes,[39] because of the higher local electric fields found at their tips. Fig. 3.3a shows a finite-element simulation of the field produced by a straight nanotube near a flat, conducting electrode. The electric field is clearly larger at the tip than along the length of the nanotube. Fig. 3.3b shows the field of the same nanotube now bent toward the counter electrode. The field near the tip significantly increases as the distance to the counter electrode is reduced. (This conclusion is not obvious without simulation. As the tube bends towards the electrode, the distance between

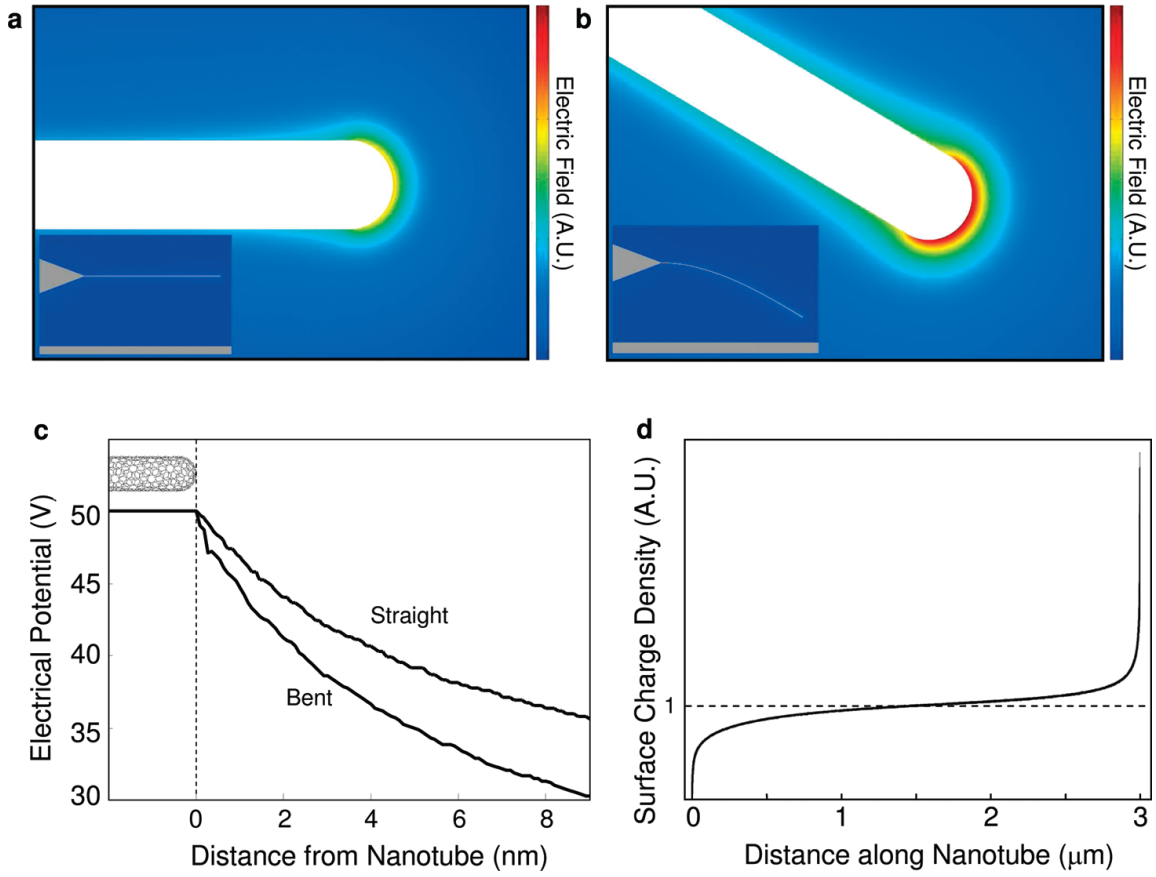

Figure 3.3: Simulations of the electrostatic properties of a 3 μm long, 5 nm radius, carbon nanotube at 50 V. The nanotube is 1.5 μm from the counter electrode, which is shown in gray. a) The electric field near a straight carbon nanotube. The electric field is enhanced at the tip of the nanotube due to the increased curvature there. b) The electric field near the nanotube when it is bent close to the counter electrode. Note that the electric field at the tip is significantly larger than the field at the tip of the straight tube. c) The electrostatic potential energy landscape near the tip of the nanotube. The barrier for field emission is substantially smaller for the bent tube, indicating that the field emission current will be larger. d) The surface charge density distribution over the length of the nanotube. The charge can be approximated as a combination of that of an infinitely long cylinder, shown as the dotted line, and a concentrated charge at the tip. (Parts (a,b,d) created by me. Part (c) courtesy of Dr. Benji Aleman and Dr. Jeff Weldon.)

the tip and the electrode decreases, which tends to increase the field at the tip. However, at the same time, the field enhancement factor of the system decreases. Simulation was needed to determine which effect dominated.) This increased field leads to a reduced potential barrier at the tip, as shown in Fig. 3.3c, which in turn causes the field emission current to increase as the tube nears the counter electrode. The nanotube quickly moving towards the counter electrode causes the current spike associated with the onset of self-oscillations. This rapid movement can be quantified by analyzing in greater detail the total force acting on the nanotube.

3.3.3 Forces on the CNT

The electrostatic forces acting on the nanotube are primarily capacitive in nature. One may suspect that the charge on the nanotube is concentrated at the tip since it has very high curvature relative to the rest of the nanotube, and that the electromagnetic force on the nanotube can therefore be approximated as a force on the tip. A finite element model was important here, because it in fact came to the somewhat counter-intuitive conclusion that the nanotube is long enough that most of the charge lies on the sidewall. (Fig. 3.3d.)

The total charge on the tube is the sum of charge on the sidewall and on the tip. We approximate the sidewall charge as that of an infinitely long cylinder (dashed curve in Fig. 3.3d) and use standard techniques[77] to solve for the capacitive sidewall force,[40, 66]

$$F_s(x, V_t) = \frac{\pi\epsilon_0 L \sin\theta}{\sqrt{(d_0 - x/2)((d_0 - x/2) + 2r)\,\mathrm{arcCosh}^2\left(1 + \dfrac{d_0 - x/2}{r}\right)}} V_t^2. \qquad (3.1)$$

Here x is the displacement of the nanotube tip, d_0 is the initial distance (i.e. when $V_t = 0$) from the tip to the counter electrode, L is the length of the nanotube, r is the nanotube radius, V_t is the voltage of the nanotube with respect to the counterelectrode, θ is the initial angle the longitudinal axis of the tube makes with the normal to the ground plane, and ϵ_0 is the permittivity of vacuum. The tip charge is approximated with a parametrically derived expression for flat-end nanocylinders[86] modified to account for the closed end of the nanotube,[89] resulting in the electrostatic force acting on the tip of the nanotube:

$$F_t(x, V_t) = \frac{0.85\pi\epsilon_0((d_0 + r)^2 r)^{1/3}\sin\theta}{2\sqrt{(d_0 - x)((d_0 - x) + 2r)}\,\mathrm{arcCosh}^2\left(1 + \dfrac{d_0 - x}{r}\right)} \qquad (3.2)$$

The elastic response of the nanotube is given by two components corresponding to the applied sidewall and tip forces. The spring constants associated with the

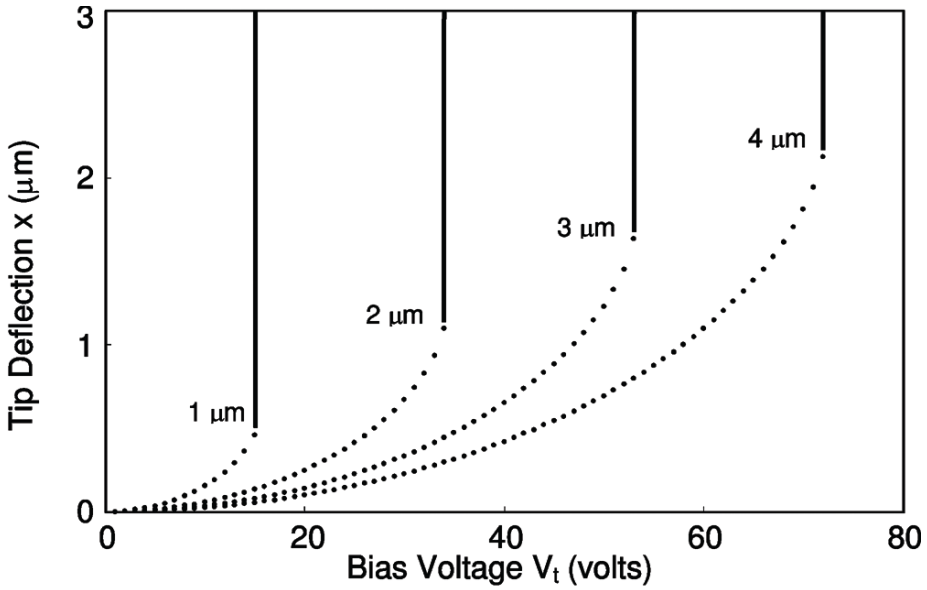

Figure 3.4: Electromechanical modeling of self-oscillating carbon nanotubes. This figure shows the deflection at equilibrium of the tip of a nanotube with a 10 nm radius as a function of bias voltage for a tube of length 3 μm with various initial distances between tube and electrode (1, 2, 3, and 4 μm.) The vertical asymptotes for each curve occur at the voltage at which no equilibrium deflection exists for the tube and the tube becomes unstable. (Courtesy of Dr. Benji Aleman.)

electrostatic forces on the sidewall and tip are $k_s = (8EI)/(L^3) = (8\pi Er^4)/(4L^3)$ and $k_t = (3EI)/(L^3) = (3\pi Er^4)/(4L^3)$, respectively, where E is the Young's modulus (approximately 1 TPa[197] for a carbon nanotube), and $I \approx \pi r^4/4$ is the areal moment of inertial.

3.3.4 Equilibrium Tip Deflection and Self-Oscillation Onset Voltage

Eqs. 3.1 and 3.2 govern the rapid nanotube deflection which initiates the self-oscillations. The equilibrium tip deflection $x = F_s/k_s + F_t/k_t$ is plotted in Fig. 3.4 for selected values of initial tip-counter electrode separation d_0. The plots reveal that the tip position becomes unstable at a critical voltage, identified by the vertical lines in Fig. 3.4. At this critical voltage V_0 the attractive electrostatic force overwhelms the repulsive elastic force and the nanotube is rapidly drawn to the counter electrode. This runaway bending has been seen previously in NEMS switches;[85, 86] here, however, the nanotube is positioned in such a way that it cannot reach the counter electrode.

The critical voltage V_0 at which the nanotube position becomes unstable and self-

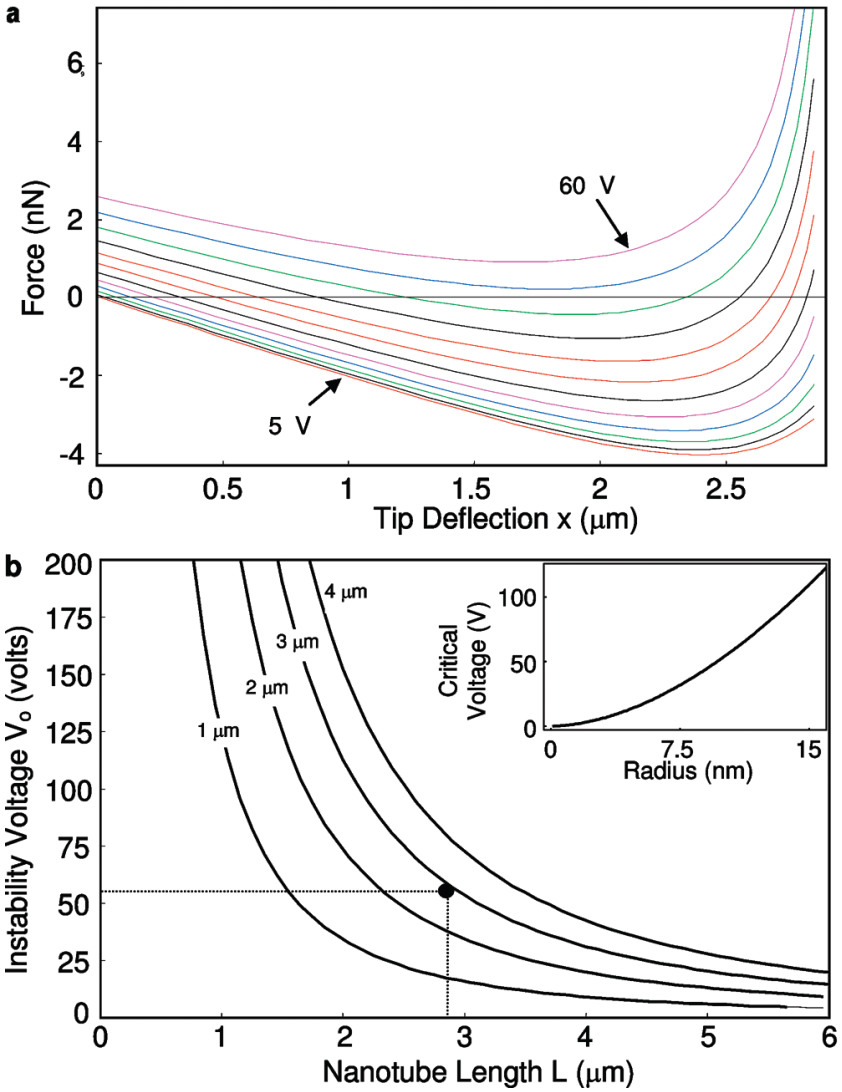

Figure 3.5: Electromechanical modeling of self-oscillating carbon nanotubes. a) The total force on the nanotube as a function of tip position for a selection bias voltages (5–60 V at 5 V intervals). Stable equilibrium positions are at the first zero of each curve and increase, as expected, with increasing voltage, and do not exist for the 55 V and 60 V curves. b) Nanotube instability voltages as a function of tube length for various initial tube–electrode distances (1, 2, 3, and 4 μm). The inset shows how the instability voltage increases with tube radius for a tube of length and initial tube–electrode distance of 3 μm. The tube is initially parallel to the electrode in all cases. (Courtesy of Dr. Benji Aleman.)

oscillations commence can be evaluated directly from geometric device parameters (r, L, d_0, θ). Fig. 3.5a is a plot of the total force (the sum of Eqs. 3.1, 3.2, and an effective spring force based on k_t and k_s) as a function of nanotube length and for bias voltages V_t ranging from 5 to 60 V at 5 V intervals. The first zero of each curve corresponds to the stable equilibrium deflection of the nanotube for a given V_t; this equilibrium deflection increases with increasing voltage. The instability voltage, V_0, of the system is given by the lowest voltage for which no zero exists, and can be calculated by finding a V_t such that $F(x, V_t) > 0$ for all x. These calculations were carried out on a tube of radius 10 nm; the results can be seen in Fig. 3.5b for continuous values of tube length and various fixed initial tip-to-counter-electrode distances. The inset of Fig. 3.5b illustrates the behavior of the instability voltage with varying nanotube radius. In general, the instability voltage, Vo, increases for shorter tubes, larger tube radii, and larger initial tip-to-counter-electrode distances. As an example, for the device geometry shown in Fig. 3.3, the model predicts $V_0 \approx 55V$, which, given the uncertainty in the position of our bottom-up devices and the approximations of the model, is in excellent agreement with the experimentally observed $V_0 = 66$ V.

3.3.5 Criteria for Sustained Self-Oscillations

Sustained self-oscillations occur for applied bias $V_t > V_0$, but only if the decay time for mechanical oscillations, given by $2Q/\omega_0$ where Q is the quality factor and ω_0 is the natural frequency of oscillation, is on the order of or greater than the recharging time, given by the RC time constant of the circuit. For the experiments described above, we estimate $2Q/\omega_0 \approx 10^{-4}$ and $RC \approx 10^{-5}$, consistent with our interpretation of the model. Also, if the bias is very close to, but just under V_0, fluctuations (for example, those associated with field emission current noise) can temporarily kick the system into self-oscillation mode. While such oscillations may last for several seconds, they are not sustainable.

3.4 Model Facilitates Large-Scale Fabrication

Bottom-up fabricated self-oscillating devices such as described above are extremely useful test structures, but their tedious serial assembly process gives them limited practical value. Since our model explicitly outlines the role geometric parameters play in self-oscillations, it facilitates the engineering of self-sustaining NEMS oscillators for large-scale fabrication. Fig. 3.6a summarizes the geometric requirements (assuming $L = d_0$) for designing self-oscillating cantilevered devices that operate within a certain desired dc bias voltage range. For example, the graph indicates that a 10-μm-long carbon nanotube will self-oscillate for an applied bias $Vt \geq 10V$ if $r < 7$ nm, while a 1 μm long tube will oscillate for similar values of V_t if $r < 2.5$

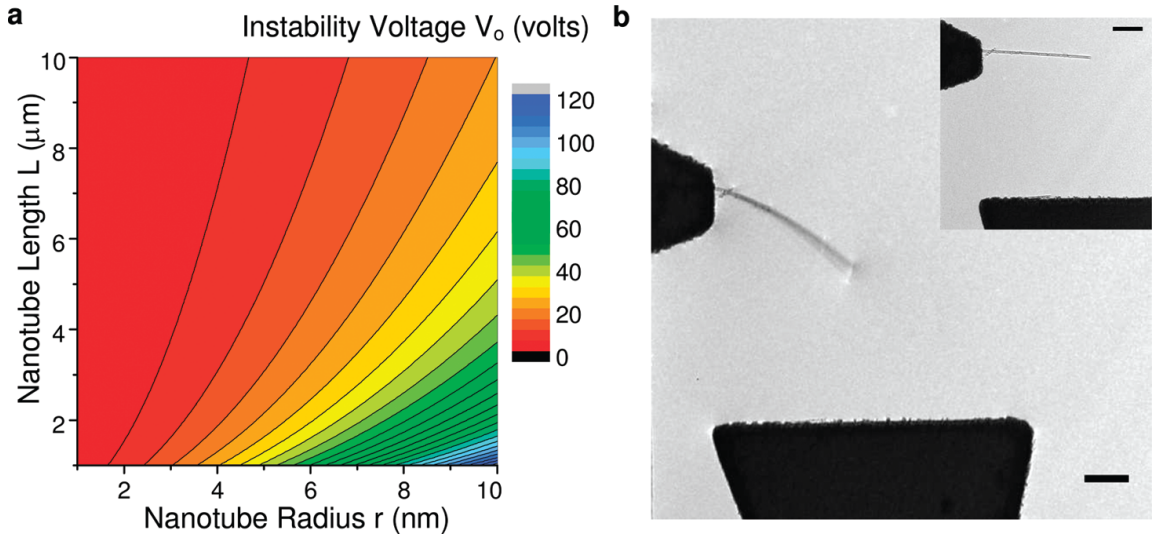

Figure 3.6: Geometric design landscape and fabrication of carbon nanotube NEMS oscillators. a) A contour plot of the self-oscillation onset as a function of nanotube length and radius. Initial tip-electrode distance is always set equal to nanotube length. (Courtesy of Dr. Benji Aleman.) b) A top-down fabricated carbon nanotube NEMS oscillator demonstrating sustained self-oscillations at 40 V; the inset shows the nanotube at 0 V (scale bars are 1 μm). (Courtesy of Dr. Will Gannett, Dr. Benji Aleman, and Dr. Jeff Weldon.)

nm.

3.5 Proof of Concept: Self-Oscillator Fabricated Using Scalable Techniques Agrees with Model

We now employ scalable methods to fabricate fully integrated self-oscillating NEMS structures with predetermined performance characteristics. We use standard optical and electron-beam lithography, microfabrication processing, and simple nanotube deposition techniques (spin casting) to produce fully suspended nanotube-based oscillators with well-defined L, d_0, r, and θ. In the inset of Fig. 3.6b is a TEM image of a suspended MWCNT and a lithographically defined counter-electrode, under no bias. Fig. 3.6b shows the same device biased into self-oscillations. For this device, V_0 was determined experimentally to be 40 V, which agrees within 10% of model predictions. To facilitate TEM characterization, the device architecture shown in Fig. 3.6b was chosen; it was realized by performing all processing on a thin Si_3N_4 membrane that was then etched to produce the suspended structure. Of course, much simpler membrane-free approaches are possible that suspend nanotubes over trenches[153] and that exploit techniques for the controlled placement of highly-aligned SWCNTs[74] or MWCNTs.[204]

3.6 Conclusion

In closing, we have demonstrated controllable, sustained self-oscillations with carbon nanotube NEMS. Additionally, we have used an electromechanical model to develop a full understanding of this behavior and have defined the necessary parameters for proper design of device architectures. Guided by these design parameters, we have fabricated operational top-down devices. The successful top-down fabrication of NEMS self-oscillators has important implications for future highly-integrated, chip-based systems, such as sensors,[78] logic and memory elements,[48] and high-frequency NEMS switches,[87] which can in principle be tailored to operate at dc bias voltages under 10 V.

3.7 Methods

J. Weldon conceived of and designed the experiments. J. Weldon and B. Aleman performed the experiments. I performed finite element simulations. B. Aleman developed the model. J. Weldon and B. Aleman interpreted the model and simulation results. B. Aleman conceived of and fabricated the top-down devices with assistance from J. Weldon and W. Gannett.

All electron transport measurements were performed with a PC-controlled Keithley 2410 using code written in Labview, and all TEM characterization was done using a JEOL 2010 TEM equipped with a Gatan digital Multiscan Camera. Transport measurements on bottom-up devices were performed using a manipulation stage (HS100 STM-Holder™ with SU100 Control System, Nanofactory Instruments AB, Sweden). Transport measurements on top-down devices were performed using a custom-built TEM stage.

Bottom-up devices were fabricated using arc-grown MWCNTs as described by Martinez et al.[127] To attach a nanotube to an AFM or STM tip, a nanomanipulator was utilized inside of a SEM. A sample of nanotubes was prepared on the edge of a piece of a razor blade with the nanotubes protruding from the edge. In the SEM, the AFM tip was moved so that it was touching a single nanotube. A gas injection system was then utilized to weld the nanotube to the AFM tip. Then either the nanotube was burned in half by a high current or the nanomanipulator was retracted, pulling the nanotube off the razor blade. The sample was then positioned in the TEM by a second nanomanipulator.

Top-down devices were fabricated by drop casting arc-grown MWCNT onto TEM transparent Si_3N_4 membranes[206] and then defining an electrode structure using electron beam lithography. After all electrodes had been defined, an SF_6 reactive ion etch was used in order to remove the Si_3N_4 membrane and thus suspend the carbon nanotube.

The electrostatic simulations (results shown in Fig. 3.3) were done with COMSOL Multiphysics, a commercially available finite element modeler. The nanotube was modeled as a 3 μm long, 10 nm wide bendable cylinder with a hemispherical cap. The counter electrode was 1.5 μm from the base of the tube, at a bias of 50 V. In all other directions, electrically insulating walls were placed 1-1.5 μm from the tube.

In the simulations which solved for the field and potential in space (Fig. 3.3a-c), the nanotube was constructed in SolidWorks and then imported into COMSOL. Its shape was approximated by the equation for a beam with a force applied at the tip,

$$d(z) = d_{tip}(\frac{1}{2}u(z)^3 - \frac{3}{2}u(z) + 1), \tag{3.3}$$

where the z axis is the axis of an undeflected beam (with $z = 0$ at the base of the beam), d is the deflection of the beam and

$$u(z) = 1 - z/L \tag{3.4}$$

where L is the length of the beam. The counter electrode was modeled as a plane.

In simulations of the charge density distribution, the tube was straight and the counter electrode was modeled as a cylinder surrounding the tube. This gives the same qualitative result as a model in which the counter electrode is a plane, with the benefit of reduced memory needs and simulation time due to the model's axial symmetry.

Chapter 4

Graphene Nanoribbons Obtained by Electrically Unwrapping Carbon Nanotubes

4.1 Introduction

This work was performed with Dr. Kwanpyo Kim and was published in large part in Kim, et al.[92] I performed all simulation work and Dr. Kim performed all experiments.

Graphene nanoribbons (GNRs) are attractive candidates for nanoelectronics, spintronics and nanoelectromechanical systems (NEMS).[18, 28, 27, 65, 81, 101, 114, 173, 174, 208] Lithographic and chemical methods have been used previously to produce GNRs from layered graphite or suitably prepared graphene.[28, 27, 65, 114] Alternatively, GNRs have been produced from multi-wall carbon nanotubes (MWNTs) using chemical oxidation, argon plasma etching, intercalation, metal particle-assisted unzipping, or high dc current.[18, 45, 81, 94, 101, 172, 208] High-quality (typically arc-grown) MWNTs are attractive starting materials as they display excellent current carrying capacity indicative of low defect concentration.[31, 32] Interestingly, nanoribbons derived from collapsed carbon nanotubes were reported already in 1995.[30] Employing MWNTs or single-wall nanotube (SWNTs) with narrow diameter distributions, unzipping approaches offer the possibility of large-scale production of narrow GNRs with well-controlled widths. Unfortunately, available unzipping methods have serious drawbacks related to surface contamination and introduction of structural defects, resulting in mechanical and electrical degradation.[18, 45, 81, 101, 172, 208] Highly desirable would be a MWNT unwrapping method with no reliance on harsh chemical or other detrimental treatment, with the ability to preserve (or even enhance) the quality of the MWNT fabric. Electrical current-induced unwrapping of MWNTs for GNR production is an interesting approach to this re-

quirement. Recently it was demonstrated that high electrical currents can be used to unwrap MWNTs into GNRs, but the quality of the GNRs derived was not thoroughly examined, thus urging more extensive investigation.[94]

At very high electrical bias, MWNTs can display superplasticity,[73, 72] or undergo structural failure through concentric wall-by-wall breakdown or blow-out with associated staircase-like current drops.[31, 32, 71, 206] In vacuum, this breakdown is believed to be driven by resistive heating and thermal bond breaking (as opposed to oxidation, as might occur during blow-out in air[32]). We here apply the technique of current-induced electrical breakdown of MWNTs to produce GNRs. The key is to avoid the typical catastrophic wall blow-out, but instead promote controlled thermally-induced unwrapping of the outer walls of the nanotube. Using in situ transmission electron microscopy (TEM), we also characterize GNRs structurally and electrically, including situations for which the GNR is severely mechanically flexed. GNRs derived from this method have high current-carrying capacity, which demonstrates that this is a promising technique for obtaining high quality GNRs from MWNTs.

4.2 Results and Discussion

Figure 4.1 shows schematic drawings of the fabrication process of extracting a GNR from a MWNT. Using a movable electrode, a MWNT is contacted and unwrapping of the outer walls is induced via an applied electrical current through the contact and tube. With proper voltage bias control, only part of the MWNT outer wall (upper portion in the schematic) is severed and, as shown in Figure 4.1(c), a precursor GNR is created which clings to the remaining MWNT inner core. The GNR is then systematically removed from the MWNT via sliding between the GNR and the MWNT inner core, as shown in Fig. 4.1(d). The newly formed GNR can easily be completely removed from the MWNT, or, most importantly, the sliding process can be terminated when a desired amount of GNR has been slid off. This leaves a preselected length of GNR fully suspended in vacuum, with each end electrically and mechanically attached to a conducting electrode (the remaining portion of the MWNT serves as one electrode).

Figure 4.2(a) shows a TEM image of a GNR experimentally derived from a MWNT using the electrical-current-induced unwrapping technique. Modeling of the thermally-induced nanotube wall-rupture mechanism is discussed later in this article and the supporting information. The GNR is fully suspended in vacuum, with each end electrically and mechanically attached to a conducting electrode. The original MWNT (30 nm diameter) from which the GNR is derived is located on the right side of the GNR. The length of the GNR is about 300 nm and the width, uniform along the ribbon axis, is 45 nm, suggesting about half (circumferentially) of the MWNT outermost shells were vaporized during the electrical unwrapping process. In Figure

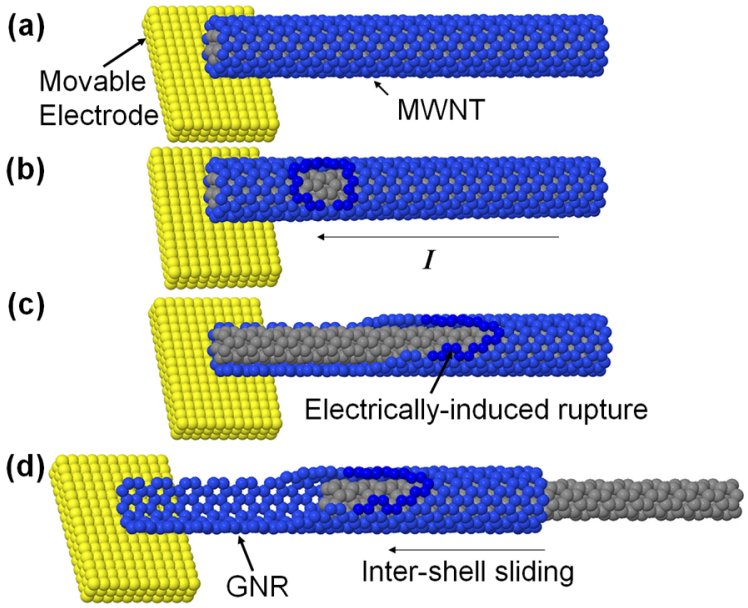

Figure 4.1: Schematic drawings of a graphene nanoribbon (GNR) fabrication from a multi-wall carbon nanotube (MWNT). In the schematic, a double wall carbon nanotube (DWNT) is chosen for simplicity. (a) MWNT before the partial wall rupture. (b) Electrical current induces rupture of the outer wall of a MWNT. (c) Partial outer wall rupture of a MWNT results in a precursor GNR which is under the MWNT inner core. (d) Inter-shell sliding between the GNR and the inner core results in a suspended, electrically contacted GNR. (Courtesy of Dr. Kwanpyo Kim.)

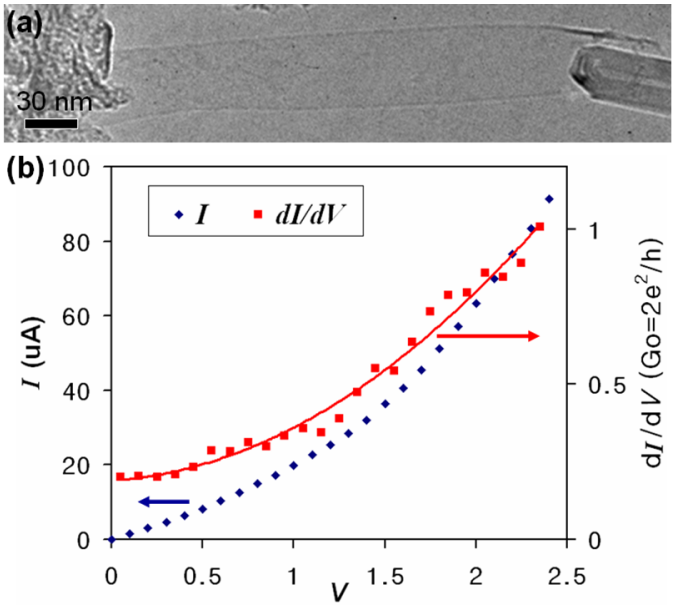

Figure 4.2: TEM images and electrical transport measurement of a GNR derived from a MWNT. (a) TEM image of a GNR derived from a MWNT via the electrical rupture and unwrapping method. The original MWNT from which the GNR is derived is shown on the right side; it continues to serve as a mechanical support and electrical contact for the GNR. (b) Electrical transport measurement of the same GNR. The blue diamond and red square dots are the electrical current and differential conductance at given voltages, respectively. The solid line is a guide to the eye for the differential conductance. At low voltages (< 0.5 V), the resistance is linear. With higher bias, the conductance increase with increasing bias. (Courtesy of Dr. Kwanpyo Kim.)

4.2(b), the two-terminal electrical transport for the same GNR is shown. The blue diamond and red square dots are respectively the electrical current and differential conductance at given bias voltages. At low bias voltages (< 0.5 V), the response is mostly linear, while at higher voltages the conductance increase with increasing bias voltage, similar to the behavior observed in MWNT two-terminal electrical transport measurements.[71]

Graphene and GNRs have remarkable mechanical properties[16, 27, 93, 108] which make them promising materials for NEMS and flexible devices. To exploit graphene and GNRs for electromechanical purposes, it is crucial to characterize electrical transport under mechanical deformation conditions, but there have been few studies on this subject. The conductance of graphene films has been observed to drop reversibly when the films are subjected to bending or stretching.[93] The GNR isolation and mounting configuration described here affords highly controlled reversible flexing and simultaneous electrical measurement of a single GNR. Figures 4.3(a-c) show a series

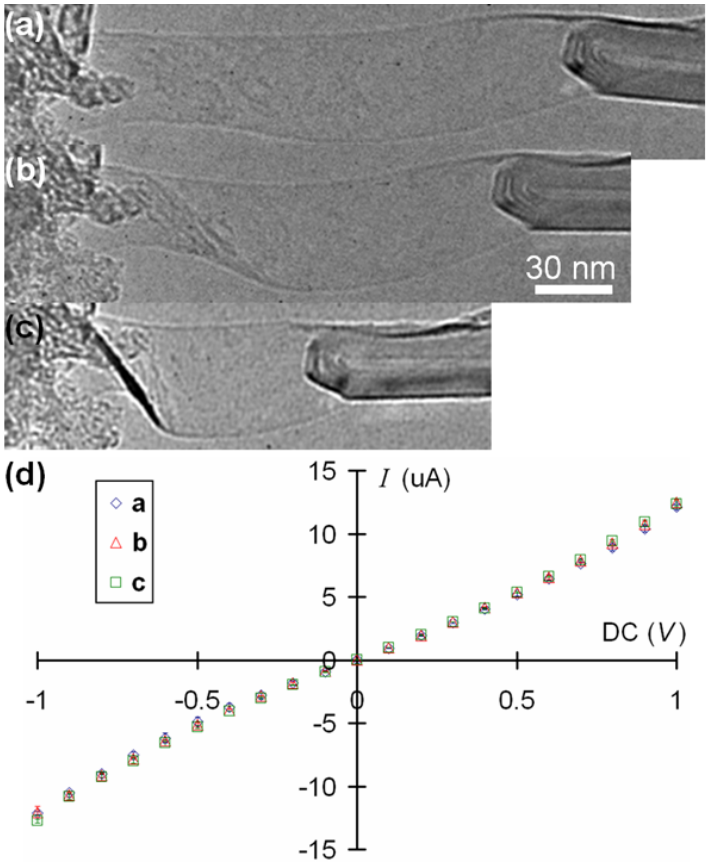

Figure 4.3: Flexing of a GNR and concurrent electrical measurement. (a-c) Sequential TEM images during the flexing process. (d) I-V curves for corresponding flexed states (figures a-c) of the GNR. The two-terminal conductance stays the same even with the dramatic mechanical deformation of the GNR. (Courtesy of Dr. Kwanpyo Kim.)

of TEM images acquired during a mechanical deformation of the GNR. Clearly, the GNR shows dramatic distortions as the MWNT electrode is moved to the left, closing the gap between the electrodes. As the degree of flexing is changed, concurrent two-terminal electrical transport measurements are performed. Figure 4.3(d) shows I-V curves for each deformation state (a-c) of the GNR. The main result is that the two-terminal resistance remains constant even with dramatic flexing of the GNR. This indicates that conductivity of GNRs (and presumably properly mounted graphene) can be maintained even under severe mechanical deformations such as high angle flexing. These results would also imply that rippling, which can occur on suspended graphene,[131] does not substantially modify the intrinsic electrical transport properties of graphene or its derivatives.

The ultimate current-carrying capacity of GNRs, and their failure mode under

extreme bias conditions, is of great interest. We find that suspended GNRs can carry large currents without failure. For the specimen of Figure 4.2, a maximum two-dimensional current density of ∼22 A/cm is obtained, comparable to that found for exfoliated graphene on a substrate.[54, 138] Notably, the GNR is here suspended in vacuum, and thus the central portion is not well thermally anchored and presumably at elevated temperature. This suggests an even higher ultimate current limit is possible for thermally anchored GNRs.

Figure 4.4 shows the results of a suspended GNR intentionally driven to electrical failure. TEM images of the GNR and corresponding transport data are shown. As seen in Figure 4.4(c), the GNR is stable and the current remains constant (∼100 A) for an applied bias of 2.5 V. As the bias is increased to 2.6 V, the current begins to drop and the middle part of the GNR diminishes in width (Figure 4.4(a)). With fixed bias, the current asymptotically approaches ∼65 A as shown in Figure 4.4(c). During the GNR breakdown, no staircase-like current drops are observed, indicating no dramatic "quantized" geometrical configurations; the GNR width gradually and smoothly diminishes. As the electrical bias is increased to ∼3 V, the GNR fails catastrophically at the central part and current drops to zero, as shown in Figure 4.4(b). The breakdown mechanism of the GNR under high bias is likely due to carbon atom sublimation from the GNR edges due to high temperatures,[17, 80] Related current-induced "shrinking" of carbon nanotubes has been reported.[205]

We now examine in more detail the electrically-induced MWNT rupture and unwrapping mechanism that leads to GNR formation. The key is the asymmetric electrode contact at the tip of the MWNT. This side-contacting results in asymmetric electrical and thermal transport conditions near the tip of the MWNT. Most notably, this results a sharp temperature difference between the non-contacted and contact outer surfaces of the MWNT near its tip. The non-contact side of the MWNT tip achieves a higher temperature than the contact side, and this is where the unwrapping (ejection of carbon atoms) is initiated. The asymmetric breakdown process is documented in Figure 4.5. Figures 4.5(a-e) show a series of TEM images for the asymmetric side-contact condition. At the bottom of the MWNT tip, amorphous carbon and MWNT composite serves as an electrode. As the bias on the MWNT is increased, the onset of MWNT shell breakdown occurs, as shown in Figures 4.5(b-c). The non-contact side of the MWNT tip experiences faster electrical breakdown. Along with the breakdown, the inner core shells of the MWNT easily slide with respect to the outer shells as shown in Figure 4.5(d), due to thermal agitation. The contact side of the MWNT tip in Fig. 4.5(d) has more intact layers (eight layers) than the non-contact side (two layers), as indicated by the arrows, which shows clearly that the wall breakdown occurs faster in the non-contact side. MWNT walls at the contact side, which do not have corresponding walls at the other side, readily evolve to low-curvature strips with edges, i.e. GNRs. In Figure 4.5(e), the inner core of the MWNT can be seen displaced left with respect to the outer shells. The GNR structures are now nearly isolated.

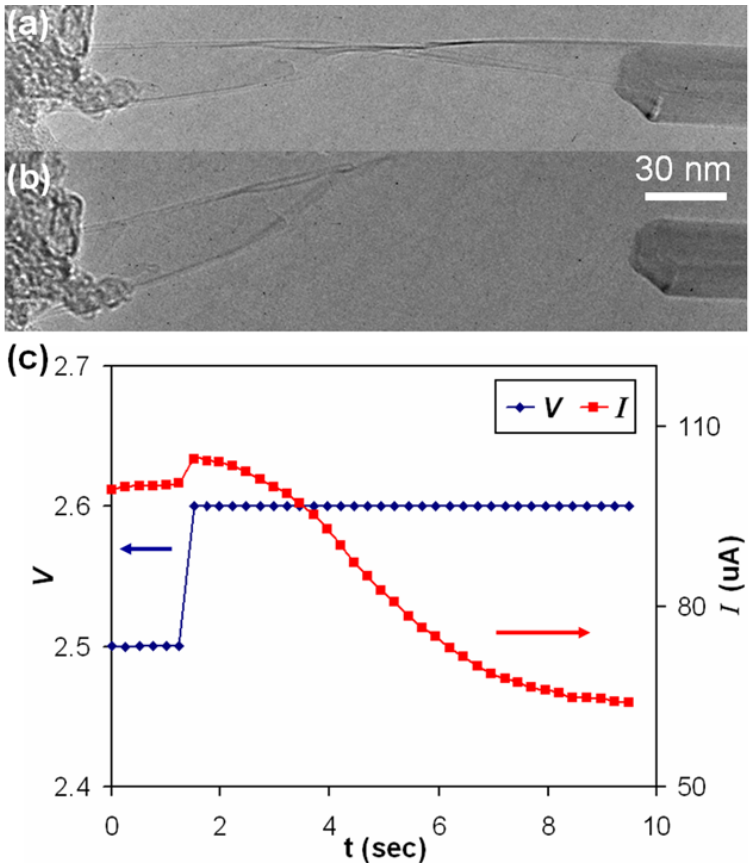

Figure 4.4: Electrical breakdown of a GNR. (a) TEM image of a GNR after partial electrical breakdown. The central part of GNR has shrunk which implies diffusive electrical transport processes along the GNR. (b) TEM image of the GNR after total breakdown. (c) Voltage and current variation in time during the electrical breakdown. Stable two-dimensional maximum electrical current density is about 22 A/cm. The lack of a staircase-like current drop suggests that the GNR undergoes gradual, not quantized, breakdown. (Courtesy of Dr. Kwanpyo Kim.)

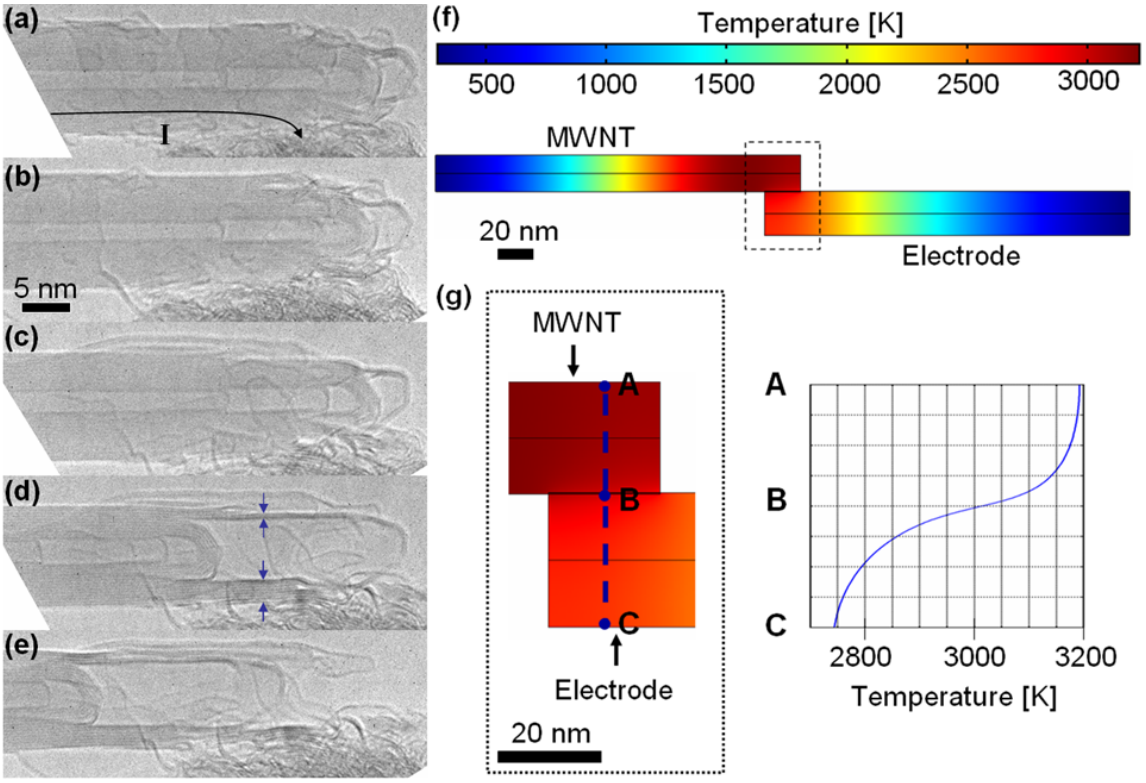

Figure 4.5: Asymmetric rupture of outer shells of a MWNT. (a-e) Sequential TEM images of an asymmetric rupture of MWNT outer shells. (a) Electrical current passes though the MWNT. At the bottom of the MWNT tip, MWNTs and amorphous carbon composite serve as an electrode. (b-c) MWNT walls start to undergo an electrical rupture. The non-contacted side of the MWNT tip ruptures first. (d) The inner core of MWNT slides to the left with respect to the outer shells. In the outer shells, it is clear that the contact side of the tip has more layers (eight layers) than the non-contact side (two layers). (e) The inner core of the MWNT slides farther with respect to the outer shells. Around the MWNT tip, a GNR-like structure appears. (f) Temperature profile of a MWNT and an electrode contacting the side of the tip from finite element analysis. Due to Joule heating, the area near the MWNT-electrode contact generally has a higher temperature than other parts of the system, reaching temperatures above 3000 K. (g) Zoomed-in image and temperature profile of the MWNT tip contact region. Temperature profile along line ABC shows that the non-contact side of the MWNT reaches higher temperatures than the contact side because the electrode acts as a heat sink. (Parts (a-e) courtesy of Dr. Kwanpyo Kim. Parts (f) and (g) are the results of my simulations.)

We carry out finite element analysis on a side-contact MWNT geometry to quantify the asymmetric temperature distribution at the MWNT tip. The detailed analysis procedure is presented in the supporting information. We model the MWNT in the high-bias limit as a single cylinder with uniform, isotropic conductivity.[31, 32, 205, 206] Figure 4.5(f) shows the simulated temperature profile of a MWNT and an electrode contacting the side of the MWNT tip. Due to Joule heating, the area near the MWNT-electrode contact generally has a higher temperature than other parts of the system, reaching temperatures above 3000 K. A close look at the temperature profile of the MWNT tip shows that the non-contact side reaches higher temperatures than the contact side (Figure 4.5(g)). This results from the electrode serving as a heat sink. The width of the MWNT wall segment that is above the critical temperature for carbon sublimation (approximately 3200 K[10]), along with MWNT outer circumference, dictates the final GNR width.

4.3 Methods

4.3.1 TEM Experiments

Experiments are carried out inside a JEOL 2010 transmission electron microscope (TEM) operated at 100 keV, employing a nanomanipulation platform (Nanofactory Instruments AB). We choose this low acceleration voltage to minimize electron beam damages to MWNTs and GNRs. Arc-grown MWNTs are attached to an aluminum wire using conductive epoxy and the wire is then mounted to the stationary side of the holder. An etched tungsten probe is mounted to the opposite mobile side of the holder. A bundle of MWNTs or amorphous carbon-MWNT composite on the tungsten probe serves as a mobile electrode The probe is moved such that the mobile electrode touches the tip of a MWNT on the wire, creating a MWNT-MWNT contact. A stable electrical and mechanical contact at the inter-MWNT junction is established by annealing with high electrical current. The sliding process between MWNT core and shell/GNR is maintained at a rate of 1-10 nm/sec. A Keithley 2400 SourceMeter is used for electrical bias and current readout across the MWNT. Five nanotubes have been unwrapped using this electrical breakdown method.

4.3.2 Finite Element Analysis

To obtain the simulation results shown in Figure 4.5, we have used COMSOL Multiphysics, a commercially available finite element modeler. To simulate the side contact to a MWNT, we have used two MWNTs touching each other's tips as shown in Figure S1. The MWNT with a bigger diameter (24 nm) is serving as an electrode in the simulation. The heat equation incorporating the Joule heating component, $\nabla \cdot (\kappa(T)\nabla T) + \rho J^2 = 0$, has been employed in the simulation, where $\kappa(T)$ is the

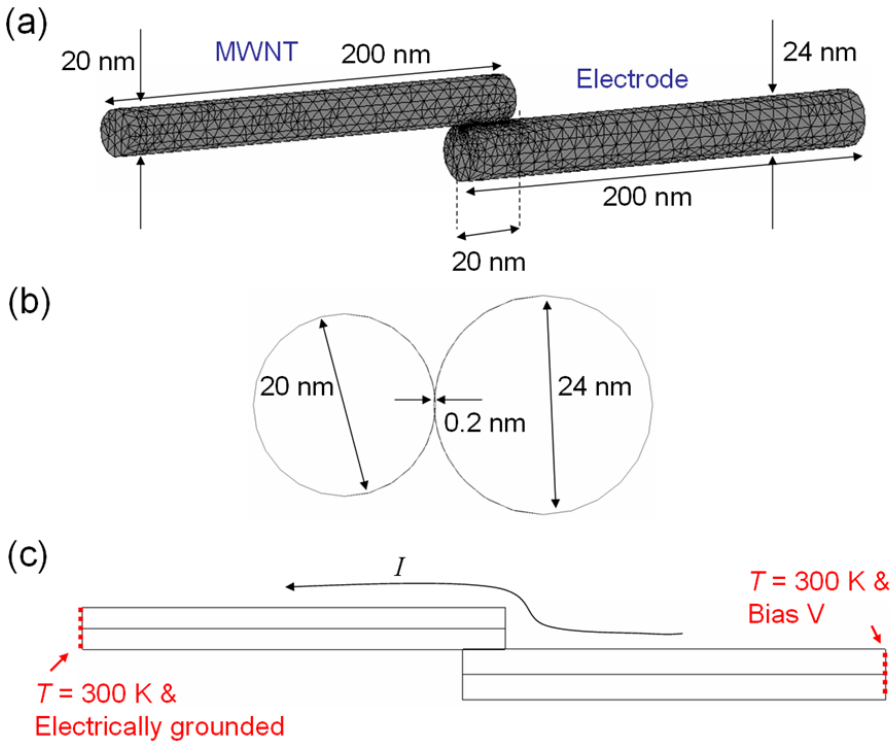

Figure 4.6: Geometry of finite element analysis simulation. (a) The geometry of two MWNTs (with 200 nm length) touching each other's tips. A MWNT with bigger diameter (24 nm) is serving as an electrode. There is a 20 nm overlap along the length between the MWNT and the electrode. (b) The side view of the geometry. The overlap between the MWNT and the electrode is 0.2 nm in the simulation. (c) The boundary conditions of the simulation. At the left and right edges, the temperatures are maintained at room temperature, 300 K. And an electrical bias is applied between these two edges. (Simulations performed by me. Image courtesy of Kwanpyo Kim.)

temperature-dependent isotropic thermal conductivity, T is temperature, ρ is resistivity, and J is current density. High temperature thermal conductivity $\kappa(T)$ of a MWNT is assumed to be $\kappa(T) = 1/(\alpha T + \beta T^2)$ with $\alpha = 4.8 \times 10^{-6}$ m/W and $\beta = 4.3 \times 10^{-10}$ m/WK (values adapted from G.E. Begtrup, et al.)[10]. Isotropic resistivity ρ=2×10^{-6} Ωm of a MWNT is adapted from T. D. Yuzvinsky, et al.[206]

As a boundary condition, the temperatures on the left and right edges of the system are maintained at room temperature (300 K). And an electrical bias V is applied between these two edges. On the other surfaces, a boundary condition with radiation heat exchange and electrical insulation is incorporated. For a given electrical bias V, we can solve the electrostatic equation and get the current density J in the system. Using the heat equation and boundary conditions, we obtain a temperature profile in

the system. To establish the highest temperatures in the system at 3200 K, which is the proposed breakdown temperature of a MWNT[10], we adjust the electrical bias V to the proper value.

Chapter 5

Enhancement of Optical Near Field by Nanostructures

5.1 Introduction

It is a well known effect that at surfaces of very high curvature, the electromagnetic fields can be greatly enhanced [154]. When light is incident on a particle and the wavelength of that light is close to the natural electromagnetic eigenmodes of that particle, large local field enhancements can occur [90]. This kind of local optical field enhancement has been exploited in a number of applications [13], including increased light absorption in solar cells [20, 134], high-resolution optical microscopy [129], and light emission [119]. Recent computational work [21] and experiments [19, 20, 22, 141] have shown that silicon nanowires in particular exhibit a large near field optical enhancement at certain resonant frequencies. This work serves as a further exploration of this phenomenon, and the resonant and off-resonant frequencies for particular nanowires, using computational modeling tools.

5.2 Modeling

I use COMSOL to model the local field of a Si nanowire in free space. A plane wave of infrared light approaches perpendicularly to the nanowire axis, with wavelength 785 nm. To simplify the simulation, I consider two cases: the case in which the electric field of the plane wave is parallel to the nanowire axis, and the case in which the magnetic field of the plane wave is parallel to the nanowire axis.

To perform simulations involving electromagnetic waves, it is generally best to use COMSOL's RF module.

If we approximate the nanowire as infinitely long, we can exploit the symmetry of the problem along the nanowire axis to perform a two-dimensional simulation. The solution along one cross-section (perpendicular to the nanowire axis) of the system

will be the solution along all cross-sections of the system. Since the light approaches in this same plane, we can use COMSOL's In-Plane Waves Application Mode to simulate the system.

We first consider the case in which the electric field is parallel to the nanowire axis. This corresponds to the TE (transverse electric field) Waves Application Mode.

In cases in which the solution will be time-harmonic, COMSOL has a special Analysis Type called Harmonic Propagation which makes use of the fact that the solution is harmonic to simply its calculations. In cases of scattered waves, COMSOL has an even more specialized Analysis Type called Scattered Harmonic Propagation which only solves for the scattered field. This analysis type has a number of benefits over Harmonic Propagation, and I use it here.

I draw the cross section of the nanowire and the free space around it in the usual way. We set the refractive index of the nanowire to $n_{Si} = 3.691 - 0.005i$.

In electromagnetic wave simulations, special things must be done to account for the fact that the scattered electromagnetic wave will normally reflect off the boundary of the bounding box. To account for this, we place additional subdomains around the bounding box with "perfectly matched layer" properties. These domains perfectly absorb certain kinds of plane waves. We set each domain to be of the type to perfectly absorb a plane wave coming from the nanowire center. For example, for the left subdomain, in the Subdomain Settings, under the PML tab, we set "Type of PML" to Cartesian, check "absorbing in the x direction," and make sure that Center Point is (0,0). For the top subdomain, we do the same but check "absorbing the y direction." For the bottom/right corner subdomain, we do the same but check both.

To further attempt to absorb any additional scattered wave, we set the outer boundaries to "Scattering Boundary Condition", with wave type Cylindrical Wave, coming from the center.

We set the incoming plane wavelength by changing "Specify Wave Using" in Properties under the Physics menu to "free space wavelength," then in Scalar Variables under the Physics menu we set the free space wavelength to $785e-9$.

We are only interested in the solution in the free space subdomain (not the Si or the perfectly matched layers), so we can plot using Domain Plot Parameters under the Postprocessing Menu. It can be useful to get the solution at different phases with respect to the incoming plane wave; this can be done by changing the "Solution at angle (phase)" text box in the Domain Plot Parameters window. In my case I choose to look at the solution a half phase (180°) out of sync with the incoming plane wave. Fig. 5.1a shows the square of the electric field of this system. Fig. 5.1b is the result of the exact same analysis but for a 179.8 nm radius nanowire.

Repeating the steps above with 208.7 and 180.2 nm radius nanowires, and using COMSOL's TM wave Application Mode, I get Figs. 5.1c and 5.1d. These figures reproduce those in Cao, et al. As discussed in Cao, et al., Figs. 5.1a and 5.1c show excitations at resonance, and Figs. 5.1b and 5.1d show off-resonance excitations.

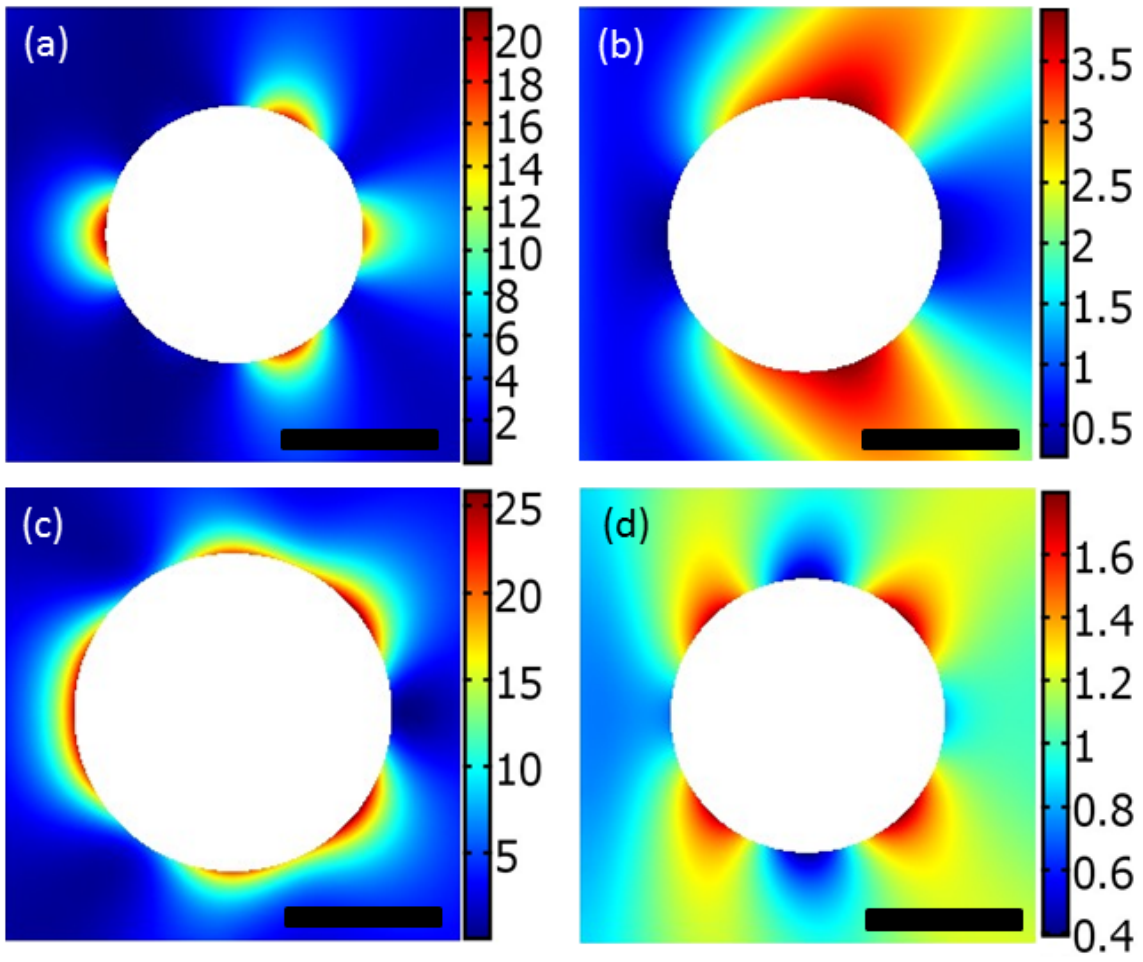

Figure 5.1: Cross sectional view of the average squared electric field near silicon nanowires excited by light of wavelength 785 nm, traveling from left to right. Scale bar is 200 nm. Color bar is arbitrary units. (a) and (b) are TE-mode excitation of 169.3 nm and 179.8 nm diameter silicon nanowires, respectively. (c) and (d) are TM-mode excitations of 208.7 nm and 180.2 nm diameter silicon nanowires, respectively. Notice that (a) and (c), which are on-resonance, have quite large field enhancements, and (b) and (d), which are off-resonance, have much smaller enhancements.

Bibliography

[1] N. Acacia, F. Barreca, E. Barletta, D. Spadaro, G. Curr, and F. Neri. Laser ablation synthesis of indium oxide nanoparticles in water. *Applied Surface Science*, 256(22):6918–6922, 2010.

[2] G. An, N. Na, X. Zhang, Z. Miao, S. Miao, K. Ding, and Z. Liu. SnO_2/carbon nanotube nanocomposites synthesized in supercritical fluids: highly efficient materials for use as a chemical sensor and as the anode of a lithium-ion battery. *Nanotechnology*, 18(43):435707, 2007.

[3] A. Ayari, P. Vincent, S. Perisanu, M. Choueib, V. Gouttenoire, M. Bechelany, D. Cornu, and S. Purcell. Self-oscillations in field emission nanowire mechanical resonators: A nanometric dc-ac conversion. *Nano Letters*, 7(8):2252–2257, 2007.

[4] A. M. Azad, S. A. Akbar, S. G. Mhaisalkar, L. D. Birkefeld, and K. S. Goto. Solid state gas sensors: A review. *Journal of the Electrochemical Society*, 139(12):3690–3704, 1992.

[5] S. Bae, H. Kim, Y. Lee, X. Xu, J.-S. Park, Y. Zheng, J. Balakrishnan, T. Lei, H. R. Kim, Y. I. Song, Y.-J. Kim, K. S. Kim, B. Ozyilmaz, J.-H. Ahn, B. H. Hong, and S. Iijima. Roll-to-roll production of 30-inch graphene films for transparent electrodes. *Nature Nanotechnology*, 5(8):574–578, 2010.

[6] A. A. Balandin, S. Ghosh, W. Bao, I. Calizo, D. Teweldebrhan, F. Miao, and C. N. Lau. Superior thermal conductivity of single-layer graphene. *Nano Letters*, 8(3):902–907, 2008.

[7] F. G. Banica. *Chemical Sensors and Biosensors: Fundamentals and Applications*. Wiley, Chichester, 2012.

[8] W. Bao, F. Miao, Z. Chen, H. Zhang, W. Jang, C. Dames, and C. N. Lau. Controlled ripple texturing of suspended graphene and ultrathin graphite membranes. *Nature Nanotechnology*, 4(9):562–566, 2009.

[9] E. P. S. Barrett, G. C. Georgiades, and P. A. Sermon. The mechanism of operation of WO_3-based H_2S sensors. *Sensors and Actuators B: Chemical*, 1(16):116–120, 1990.

[10] G. E. Begtrup, K. G. Ray, B. M. Kessler, T. D. Yuzvinsky, H. Garcia, and A. Zettl. Probing nanoscale solids at thermal extremes. *Physical Review Letters*, 99(15):155901, 2007.

[11] T. V. Belysheva, E. A. Kazachkov, and E. E. Gutman. Gas sensing properties of In_2O_3 and Au-doped In_2O_3 films for detecting carbon monoxide in air. *Journal of Analytical Chemistry*, 56(7):676–678, 2001.

[12] O. Berger, T. Hoffmann, W. J. Fischer, and V. Melev. Tungsten-oxide thin films as novel materials with high sensitivity and selectivity to NO_2, O_3, and H_2S. Part II: Application as gas sensors. *Journal of Materials Science: Materials in Electronics*, 15(7):483–493, 2004.

[13] P. Bharadwaj, B. Deutsch, and L. Novotny. Optical antennas. *Advances in Optics and Photonics*, 1(3):438–483, 2009.

[14] P. Bhattacharya, R. R. Das, and R. S. Katiyar. Fabrication of stable wide-band-gap ZnO/MgO multilayer thin films. *Applied Physics Letters*, 83(10):2010–2012, 2003.

[15] K. I. Bolotin, K. J. Sikes, Z. Jiang, M. Klima, G. Fudenberg, J. Hone, P. Kim, and H. L. Stormer. Ultrahigh electron mobility in suspended graphene. *Solid State Communications*, 146(9):351–355, 2008.

[16] J. S. Bunch, A. M. van der Zande, S. S. Verbridge, I. W. Frank, D. M. Tanenbaum, J. M. Parpia, H. G. Craighead, and P. L. McEuen. Electromechanical resonators from graphene sheets. *Science*, 315(5811):490–493, 2007.

[17] J. Campos-Delgado, J. M. Romo-Herrera, X. Jia, D. A. Cullen, H. Muramatsu, Y. A. Kim, T. Hayashi, Z. Ren, D. J. Smith, Y. Okuno, T. Ohba, H. Kanoh, K. Kaneko, M. Endo, H. Terrones, M. S. Dresselhaus, and M. Terrones. Bulk production of a new form of sp^2 carbon: Crystalline graphene nanoribbons. *Nano Letters*, 8(9):2773–2778, 2008.

[18] A. G. Cano-Márquez, F. J. Rodríguez-Macías, J. Campos-Delgado, C. G. Espinosa-González, F. Tristán-López, D. Ramírez-González, D. A. Cullen, D. J. Smith, M. Terrones, and Y. I. Vega-Cantú. Ex-MWNTs: Graphene sheets and ribbons produced by lithium intercalation and exfoliation of carbon nanotubes. *Nano Letters*, 9(4):1527–1533, 2009.

[19] L. Cao, P. Fan, E. S. Barnard, A. M. Brown, and M. L. Brongersma. Tuning the color of silicon nanostructures. *Nano Letters*, 10(7):2649–2654, 2010.

[20] L. Cao, P. Fan, A. P. Vasudev, J. S. White, Z. F. Yu, W. S. Cai, J. A. Schuller, S. H. Fan, and M. L. Brongersma. Semiconductor nanowire optical antenna solar absorbers. *Nano Letters*, 10(2):439–445, 2010.

[21] L. Cao, B. Garipcan, E. M. Gallo, S. S. Nonnenmann, B. Nabet, and J. E. Spanier. Excitation of local field enhancement on silicon nanowires. *Nano Letters*, 8(2):601–605, 2008.

[22] L. Cao, J. S. White, J.-S. Park, J. A. Schuller, B. M. Clemens, and M. L. Brongersma. Engineering light absorption in semiconductor nanowire devices. *Nature Materials*, 8(8):643–647, 2009.

[23] M. A. Carpenter, S. Mathur, and A. Kolmakov. *Metal Oxide Nanomaterials for Chemical Sensors*. Springer, New York, 2012.

[24] A. H. Castro Neto, F. Guinea, N. M. R. Peres, K. S. Novoselov, and A. K. Geim. The electronic properties of graphene. *Reviews of Modern Physics*, 81(1):109–162, 2009.

[25] J.-C. Charlier, X. Blase, and S. Roche. Electronic and transport properties of nanotubes. *Reviews of Modern Physics*, 79(2):677–732, 2007.

[26] A. P. Chatterjee, P. Mitra, and A. K. Mukhopadhyay. Chemically deposited zinc oxide thin film gas sensor. *Journal of Materials Science*, 34(17):4225–4231, 1999.

[27] C. Chen, S. Rosenblatt, K. I. Bolotin, W. Kalb, P. Kim, I. Kymissis, H. L. Stormer, T. F. Heinz, and J. Hone. Performance of monolayer graphene nanomechanical resonators with electrical readout. *Nature Nanotechnology*, 4(12):861–867, 2009.

[28] Z. Chen, Y.-M. Lin, M. J. Rooks, and P. Avouris. Graphene nano-ribbon electronics. *Physica E-Low-Dimensional Systems and Nanostructures*, 40(2):228–232, 2007.

[29] S. Choopun, R. D. Vispute, W. Yang, R. P. Sharma, T. Venkatesan, and H. Shen. Realization of band gap above 5.0 eV in metastable cubic-phase $Mg_xZn_{(1-x)}O$ alloy films. *Applied Physics Letters*, 80(9):1529–1531, 2002.

[30] N. G. Chopra, L. X. Benedict, V. H. Crespi, M. L. Cohen, S. G. Louie, and A. Zettl. Fully collapsed carbon nanotubes. *Nature*, 377(6545):135–138, 1995.

[31] P. G. Collins, M. S. Arnold, and P. Avouris. Engineering carbon nanotubes and nanotube circuits using electrical breakdown. *Science*, 292(5517):706–709, 2001.

[32] P. G. Collins, M. Hersam, M. S. Arnold, R. Martel, and P. Avouris. Current saturation and electrical breakdown in multiwalled carbon nanotubes. *Physical Review Letters*, 86(14):3128–3131, 2001.

[33] E. Comini. Metal oxide nano-crystals for gas sensing. *Analytica Chimica Acta*, 568(1):28–40, 2006.

[34] E. Comini, G. Faglia, and G. Sberveglieri. *Electrical-Based Gas Sensing*. Solid State Gas Sensing. Springer, New York, 2009.

[35] R. M. Cornell and U. Schwertmann. *The Iron Oxides: Structure, Properties, Reactions, Occurences and Uses*. Wiley, Weinheim, 2003.

[36] H. Craighead. Nanoelectromechanical systems. *Science*, 290(5496):1532–1535, 2000.

[37] T. V. Cuong, V. H. Pham, J. S. Chung, E. W. Shin, D. H. Yoo, S. H. Hahn, J. S. Huh, G. H. Rue, E. J. Kim, S. H. Hur, and P. A. Kohl. Solution-processed ZnO-chemically converted graphene gas sensor. *Materials Letters*, 64(22):2479–2482, 2010.

[38] S. K. Deb. Opportunities and challenges in science and technology of WO_3 for electrochromic and related applications. *Solar Energy Materials and Solar Cells*, 92(2):245–258, 2008.

[39] W. A. Deheer, A. Chatelain, and D. Ugarte. A carbon nanotube field-emission electron source. *Science*, 270(5239):1179, 1995.

[40] M. Dequesnes, S. Rotkin, and N. Aluru. Calculation of pull-in voltages for carbon-nanotube-based nanoelectromechanical switches. *Nanotechnology*, 13(1):120–131, 2002.

[41] R. Dronskowski. The little maghemite story: A classic functional material. *Advanced Functional Materials*, 11(1):27–29, 2001.

[42] C. Durand, F. Casset, P. Renaux, N. Abele, B. Legrand, D. Renaud, E. Ollier, P. Ancey, A. Ionescu, and L. Buchaillot. In-plane silicon-on-nothing nanometer-scale resonant suspended gate MOSFET for in-IC integration perspectives. *IEEE Electron Device Letters*, 29(5):494, 2008.

[43] S. Dutta and S. K. Pati. Novel properties of graphene nanoribbons: a review. *Journal of Materials Chemistry*, 20(38):8207–8223, 2010.

[44] D. J. Dwyer. Surface chemistry of gas sensors: H_2S on WO_3 films. *Sensors and Actuators B: Chemical*, 5(14):155–159, 1991.

[45] A. L. Elías, A. R. Botello-Méndez, D. Meneses-Rodríguez, V. Jehová González, D. Ramírez-González, L. Ci, E. Muñoz Sandoval, P. M. Ajayan, H. Terrones, and M. Terrones. Longitudinal cutting of pure and doped carbon nanotubes to form graphitic nanoribbons using metal clusters as nanoscalpels. *Nano Letters*, 10(2):366–372, 2009.

[46] G. Eranna. *Metal Oxide Nanostructures as Gas Sensing Devices*. Taylor, Boca Raton, 2011.

[47] D. W. H. Fam, A. I. Y. Tok, A. Palaniappan, P. Nopphawan, A. Lohani, and S. G. Mhaisalkar. Selective sensing of hydrogen sulphide using silver nanoparticle decorated carbon nanotubes. *Sensors and Actuators B: Chemical*, 138(1):189–192, 2009.

[48] X. L. Feng, C. J. White, A. Hajimiri, and M. L. Roukes. A self-sustaining ultrahigh-frequency nanoelectromechanical oscillator. *Nature Nanotechnology*, 3(6):342, 2008.

[49] B. Frühberger, M. Grunze, and D. J. Dwyer. Surface chemistry of H_2S-sensitive tungsten oxide films. *Sensors and Actuators B: Chemical*, 31(3):167–174, 1996.

[50] M. Fujita, K. Wakabayashi, K. Nakada, and K. Kusakabe. Peculiar localized state at zigzag graphite edge. *Journal of the Physical Society of Japan*, 65(7):1920–1923, 1996.

[51] G. Fursey, I. Brodie, and P. Shwoebel. *Field Emission in Vacuum Microelectronics*. Plenum, New York, 2005.

[52] A. K. Geim. Graphene: Status and prospects. *Science*, 324(5934):1530–1534, 2009.

[53] A. K. Geim and K. S. Novoselov. The rise of graphene. *Nature Materials*, 6(3):183–191, 2007.

[54] Ç. Ö. Girit and A. Zettl. Soldering to a single atomic layer. *Applied Physics Letters*, 91(19):193512, 2007.

[55] A. Goldoni, R. Larciprete, L. Petaccia, and S. Lizzit. Single-wall carbon nanotube interaction with gases: Sample contaminants and environmental monitoring. *Journal of the American Chemical Society*, 125(37):11329–33, 2003.

[56] R. Gomer. *Field Emission and Field Ionization*. Harvard, Cambridge, 1961.

[57] P. I. Gouma. *Nanomaterials for Chemical Sensors and Biotechnology*. Pan Stanford, Singapore, 2009.

[58] A. Gramm and A. Schtze. High performance solvent vapor identification with a two sensor array using temperature cycling and pattern classification. *Sensors and Actuators B: Chemical*, 95(1):58–65, 2003.

[59] C.-C. Granqvist. Electrochromic materials: Microstructure, electronic bands, and optical properties. *Applied Physics A*, 57(1):3–12, 1993.

[60] C.-C. Granqvist. Electrochromic materials: Out of a niche. *Nature Materials*, 5(2):89–90, 2006.

[61] P. Gründler. *Chemical Sensors: An Introduction for Scientists and Engineers*. Springer, Berlin, 2007.

[62] S. K. Gupta, A. Joshi, and M. Kaur. Development of gas sensors using ZnO nanostructures. *Journal of Chemical Sciences*, 122(1):57–62, 2010.

[63] A. Gurlo and R. Riedel. In situ and operando spectroscopy for assessing mechanisms of gas sensing. *Angewandte Chemie International Edition*, 46(21):3826–3848, 2007.

[64] A. Gutés, B. Hsia, A. Sussman, W. Mickelson, A. Zettl, C. Carraro, and R. Maboudian. Graphene decoration with metal nanoparticles: Towards easy integration for sensing applications. *Nanoscale*, 4(2):438–440, 2012.

[65] M. Y. Han, B. Oezyilmaz, Y. Zhang, and P. Kim. Energy band-gap engineering of graphene nanoribbons. *Physical Review Letters*, 98(20):206805, 2007.

[66] W. H. Hayt and J. A. Buck. *Engineering Electromagnetics*. McGraw-Hill, Boston, 2006.

[67] T. He and J. Yao. Photochromic materials based on tungsten oxide. *Journal of Materials Chemistry*, 17(43):4547–4557, 2007.

[68] S. Hofmann. *Auger- and X-Ray Photoelectron Spectroscopy in Materials Science: A User-Oriented Guide*. Springer, Berlin, 2012.

[69] M. Hosokawa, K. Nogi, M. Naito, and T. Yokoyama. *Nanoparticle Technology Handbook*. Elsevier, Amsterdam, 2007.

[70] Y. Hu, O. K. Tan, and W. Zhu. *Solid-State Gas Sensors*, pages 1–42. CRC, Boca Raton, 2010.

[71] J. Y. Huang, S. Chen, S. H. Jo, Z. Wang, D. X. Han, G. Chen, M. S. Dresselhaus, and Z. F. Ren. Atomic-scale imaging of wall-by-wall breakdown and concurrent transport measurements in multiwall carbon nanotubes. *Physical Review Letters*, 94(23):236802, 2005.

[72] J. Y. Huang, S. Chen, Z. F. Ren, Z. Wang, K. Kempa, M. J. Naughton, G. Chen, and M. S. Dresselhaus. Enhanced ductile behavior of tensile-elongated individual double-walled and triple-walled carbon nanotubes at high temperatures. *Physical Review Letters*, 98(18):185501, 2007.

[73] J. Y. Huang, S. Chen, Z. Q. Wang, K. Kempa, Y. M. Wang, S. H. Jo, G. Chen, M. S. Dresselhaus, and Z. F. Ren. Superplastic carbon nanotubes - conditions have been discovered that allow extensive deformation of rigid single-walled nanotubes. *Nature*, 439(7074):281–281, 2006.

[74] L. M. Huang, B. White, M. Y. Sfeir, M. Y. Huang, H. X. Huang, S. Wind, J. Hone, and S. O'Brien. Cobalt ultrathin film catalyzed ethanol chemical vapor deposition of single-walled carbon nanotubes. *Journal of Physical Chemistry B*, 110(23):11103–11109, 2006.

[75] X. Huang, F. Meng, Z. Pi, W. Xu, and J. Liu. Gas sensing behavior of a single tin dioxide sensor under dynamic temperature modulation. *Sensors and Actuators B: Chemical*, 99(2):444–450, 2004.

[76] M. Ivanovskaya, D. Kotsikau, G. Faglia, and P. Nelli. Influence of chemical composition and structural factors of Fe_2O_3/In_2O_3 sensors on their selectivity and sensitivity to ethanol. *Sensors and Actuators B: Chemical*, 96(3):498–503, 2003.

[77] J. D. Jackson. *Classical Electrodynamics*. Wiley, New York, 1999.

[78] K. Jensen, K. Kim, and A. Zettl. An atomic-resolution nanomechanical mass sensor. *Nature Nanotechnology*, 3(9):533–537, 2008.

[79] K. Jensen, J. Weldon, H. Garcia, and A. Zettl. Nanotube radio. *Nano Letters*, 8(1):374, 2008.

[80] X. Jia, M. Hofmann, V. Meunier, B. G. Sumpter, J. Campos-Delgado, J. M. Romo-Herrera, H. Son, Y.-P. Hsieh, A. Reina, J. Kong, M. Terrones, and M. S. Dresselhaus. Controlled formation of sharp zigzag and armchair edges in graphitic nanoribbons. *Science*, 323(5922):1701–1705, 2009.

[81] L. Jiao, L. Zhang, X. Wang, G. Diankov, and H. Dai. Narrow graphene nanoribbons from carbon nanotubes. *Nature*, 458(7240):877–880, 2009.

[82] G. Jiménez-Cadena, J. Riu, and F. X. Rius. Gas sensors based on nanostructured materials. *Analyst*, 132(11):1083–1099, 2007.

[83] Z. Jing, Y. Wang, and S. Wu. Preparation and gas sensing properties of pure and doped γ-Fe_2O_3 by an anhydrous solvent method. *Sensors and Actuators B: Chemical*, 113(1):177–181, 2006.

[84] K. Kalantar-zadeh and B. Fry. *Nanotechnology-Enabled Sensors*. Springer, New York, 2008.

[85] C. H. Ke and H. D. Espinosa. Feedback controlled nanocantilever device. *Applied Physics Letters*, 85(4):681–683, 2004.

[86] C. H. Ke and H. D. Espinosa. Numerical analysis of nanotube-based NEMS devices - Part I: Electrostatic charge distribution on multiwalled nanotubes. *Journal of Applied Mechanics*, 72(5):721–725, 2005.

[87] C. H. Ke and H. D. Espinosa. In situ electron microscopy electromechanical characterization of a bistable nems device. *Small*, 2(12):1484–1489, 2006.

[88] M. Kebaili. KMHP-100 MEMS Micro-Hotplate. *Kebaili Corporation Website.* Retrieved September 15, 2013, from http://www.kebaili.com/files/MHP-100-RevA.pdf.

[89] P. Keblinski, S. K. Nayak, P. Zapol, and P. M. Ajayan. Charge distribution and stability of charged carbon nanotubes. *Physics Review Letters*, 89(25):255503, 2002.

[90] M. Kerker. *The Scattering of Light and Other Electromagnetic Radiation*. Academic, New York, 1969.

[91] J. Kim and K. Yong. Mechanism study of ZnO nanorod-bundle sensors for H_2S gas sensing. *Journal of Physical Chemistry C*, 115(15):7218–7224, 2011.

[92] K. Kim, A. Sussman, and A. Zettl. Graphene nanoribbons obtained by electrically unwrapping carbon nanotubes. *ACS Nano*, 4(3):1362–1366, 2010.

[93] K. S. Kim, Y. Zhao, H. Jang, S. Y. Lee, J. M. Kim, K. S. Kim, J.-H. Ahn, P. Kim, J.-Y. Choi, and B. H. Hong. Large-scale pattern growth of graphene films for stretchable transparent electrodes. *Nature*, 457(7230):706–710, 2009.

[94] W. S. Kim, S. Y. Moon, S. Y. Bang, B. G. Choi, H. Ham, T. Sekino, and K. B. Shim. Fabrication of graphene layers from multiwalled carbon nanotubes using high dc pulse. *Applied Physics Letters*, 95(8):083103, 2009.

[95] P. D. C. King, T. D. Veal, F. Fuchs, C. Y. Wang, D. J. Payne, A. Bourlange, H. Zhang, G. R. Bell, V. Cimalla, O. Ambacher, R. G. Egdell, F. Bechstedt, and C. F. McConville. Band gap, electronic structure, and surface electron accumulation of cubic and rhombohedral In_2O_3. *Physical Review B*, 79(20):205211, 2009. PRB.

[96] C. F. Klingshirn and A. Waag. *Zinc Oxide: From Fundamental Properties Towards Novel Applications*. Springer, Berlin, 2010.

[97] D. Kohl. Function and applications of gas sensors. *Journal of Physics D: Applied Physics*, 34(19):R125–R149, 2001.

[98] E. Kolawa, C. Garland, L. Tran, C. W. Nieh, J. M. Molarius, W. Flick, M. Nicolet, and J. Wei. Indium oxide diffusion barriers for Al/Si metallizations. *Applied Physics Letters*, 53(26):2644–2646, 1988.

[99] E. Kolawa, C. W. Nieh, J. M. Molarius, L. Tran, C. Garland, W. Flick, M.-A. Nicolet, F. C. T. So, and J. C. Wei. Reactively sputtered indium oxide diffusion barrier. *Thin Solid Films*, 166:15–20, 1988.

[100] G. Korotcenkov. *Chemical Sensors: Comprehensive Sensor Technologies. Volume 5: Electrochemical and Optical Sensors*. Sensor Technology. Momentum, New York, 2011.

[101] D. V. Kosynkin, A. L. Higginbotham, A. Sinitskii, J. R. Lomeda, A. Dimiev, B. K. Price, and J. M. Tour. Longitudinal unzipping of carbon nanotubes to form graphene nanoribbons. *Nature*, 458(7240):872–876, 2009.

[102] J. Lakowicz. *Principles of Fluorescence Spectroscopy*. Kluwer, New York, 1999.

[103] R. Lalauze. *Chemical Sensors and Biosensors*. Wiley, Hoboken, 2012.

[104] U. T. Lam, R. Mammucari, K. Suzuki, and N. R. Foster. Processing of iron oxide nanoparticles by supercritical fluids. *Industrial & Engineering Chemistry Research*, 47(3):599–614, 2008.

[105] C. M. Lampert. *Sol. Electron. Mater.*, 6:1, 1981.

[106] E. Lassner and W.-D. Schubert. *Tungsten: Properties, Chemistry, Technology of the Element, Alloys and Chemical Compounds*. Kluwer, New York, 1999.

[107] A. P. Lee and B. J. Reedy. Temperature modulation in semiconductor gas sensing. *Sensors and Actuators B: Chemical*, 60(1):35–42, 1999.

[108] C. Lee, X. Wei, J. W. Kysar, and J. Hone. Measurement of the elastic properties and intrinsic strength of monolayer graphene. *Science*, 321(5887):385–388, 2008.

[109] C. J. Lee, T. J. Lee, S. C. Lyu, Y. Zhang, H. Ruh, and H. J. Lee. Field emission from well-aligned zinc oxide nanowires grown at low temperature. *Applied Physics Letters*, 81(19):3648–3650, 2002.

[110] H. Lee, Y. W. Son, N. Park, S. Han, and J. Yu. Magnetic ordering at the edges of graphitic fragments: Magnetic tail interactions between the edge-localized states. *Physical Review B*, 72(17):174431, 2005.

[111] J. Li, Y. Lu, Q. Ye, M. Cinke, J. Han, and M. Meyyappan. Carbon nanotube sensors for gas and organic vapor detection. *Nano Letters*, 3(7):929–933, 2003.

[112] M. Li, H. Tang, and M. Roukes. Ultra-sensitive NEMS-based cantilevers for sensing, scanned probe and very high-frequency applications. *Nature Nanotechnology*, 2(2):114–120, 2007.

[113] X. Li, W. Cai, J. An, S. Kim, J. Nah, D. Yang, R. Piner, A. Velamakanni, I. Jung, E. Tutuc, S. K. Banerjee, L. Colombo, and R. S. Ruoff. Large-area synthesis of high-quality and uniform graphene films on copper foils. *Science*, 324(5932):1312–1314, 2009.

[114] X. Li, X. Wang, L. Zhang, S. Lee, and H. Dai. Chemically derived, ultrasmooth graphene nanoribbon semiconductors. *Science*, 319(5867):1229–1232, 2008.

[115] L. Liao, H. B. Lu, J. C. Li, C. Liu, D. J. Fu, and Y. L. Liu. The sensitivity of gas sensor based on single ZnO nanowire modulated by helium ion radiation. *Applied Physics Letters*, 91(17):173110–173110–3, 2007.

[116] J.-H. Lim, N. Phiboolsirichit, S. Mubeen, M. A. Deshusses, A. Mulchandani, and N. V. Myung. Electrical and gas sensing properties of polyaniline functionalized single-walled carbon nanotubes. *Nanotechnology*, 21(7):075502, 2010.

[117] T. C. Lim. *Nanosensors: Theory and Applications in Industry, Healthcare, and Defense*. CRC, Boca Raton, 2011.

[118] H.-M. Lin, C.-M. Hsu, H.-Y. Yang, P.-Y. Lee, and C.-C. Yang. Nanocrystalline WO_3-based H_2S sensors. *Sensors and Actuators B: Chemical*, 22(1):63–68, 1994.

[119] C. Liu, V. Kamaev, and Z. V. Vardeny. Efficiency enhancement of an organic light-emitting diode with a cathode forming two-dimensional periodic hole array. *Applied Physics Letters*, 86(14):143501, 2005.

[120] X. Liu, S. Cheng, H. Liu, S. Hu, D. Zhang, and H. Ning. A survey on gas sensing technology. *Sensors and Actuators B Chemical*, 12(7):9635–9665, 2012.

[121] X.-W. Liu, J.-J. Mao, P.-D. Liu, and X.-W. Wei. Fabrication of metal-graphene hybrid materials by electroless deposition. *Carbon*, 49(2):477–483, 2011.

[122] E. Llobet. Gas sensors using carbon nanomaterials: A review. *Sensors and Actuators B: Chemical*, 179:32–45, 2013.

[123] M. J. Madou and S. R. Morrison. *Chemical sensing with solid state devices*. Academic, New York, 1989.

[124] I. Mahboob and H. Yamaguchi. Bit storage and bit flip operations in an electromechanical oscillator. *Nature Nanotechnology*, 3(5):275–279, 2008.

[125] P. Majewski and B. Thierry. Functionalized magnetite nanoparticles – synthesis, properties, and bio-applications. *Critical Reviews in Solid State and Materials Sciences*, 32(3-4):203–215, 2007.

[126] M. Marezio. Refinement of the crystal structure of In_2O_3 at two wavelengths. *Acta Crystallographica*, 20(6):723–728, 1966.

[127] J. Martinez, T. D. Yuzvinsky, A. M. Fennimore, A. Zettl, R. Garca, and C. Bustamante. Length control and sharpening of atomic force microscope carbon nanotube tips assisted by an electron beam. *Nanotechnology*, 16(11):2493–2496, 2005.

[128] MatWeb. Indium Corp. In_2O_3 type B indium oxide, fine powder, 2013.

[129] N. Mauser and A. Hartschuh. Tip-enhanced near-field optical microscopy. *Chemical Society Reviews*, 2014. Advanced online publication. doi:10.1039/C3CS60258C.

[130] J. F. McAleer, P. T. Moseley, J. O. W. Norris, D. E. Williams, and B. C. Tofield. Tin dioxide gas sensors. Part 2.– The role of surface additives. *Journal of the Chemical Society-Faraday Transactions I*, 84(2):441–457, 1988.

[131] J. C. Meyer, A. K. Geim, M. I. Katsnelson, K. S. Novoselov, T. J. Booth, and S. Roth. The structure of suspended graphene sheets. *Nature*, 446(7131):60–63, 2007.

[132] W. Mickelson, A. Sussman, and A. Zettl. Low-power, fast, selective nanoparticle-based hydrogen sulfide gas sensor. *Applied Physics Letters*, 100(17):173110, 2012.

[133] T. Minami, H. Sato, H. Nanto, and S. Takata. Group III impurity doped zinc oxide thin films prepared by RF magnetron sputtering. *Japanese Journal of Applied Physics*, 24(10):L781–L784, 1985.

[134] V. Mlinar. Engineered nanomaterials for solar energy conversion. *Nanotechnology*, 24(4):042001, 2013.

[135] S. R. Morrison. *The Chemical Physics of Surfaces*. Plenum, New York, 1977.

[136] S. R. Morrison. Semiconductor gas sensors. *Sensors and Actuators*, 2:329–341, 1981.

[137] P. T. Moseley. Solid state gas sensors. *Measurement Science and Technology*, 8(3):223–237, 1997.

[138] J. Moser, A. Barreiro, and A. Bachtold. Current-induced cleaning of graphene. *Applied Physics Letters*, 91(16):163513, 2007.

[139] S. Mubeen, T. Zhang, N. Chartuprayoon, Y. Rheem, A. Mulchandani, N. V. Myung, and M. A. Deshusses. Sensitive detection of H_2S using gold nanoparticle decorated single-walled carbon nanotubes. *Analytical Chemistry*, 82(1):250–257, 2009.

[140] H. K. Muller. *Phys. Mater. Soc.*, 24:723, 1968.

[141] O. L. Muskens, J. G. Rivas, R. E. Algra, E. P. A. M. Bakkers, and A. Lagendijk. Design of light scattering in nanowire materials for photovoltaic applications. *Nano Letters*, 8(9):2638–2642, 2008.

[142] R. R. Nair, P. Blake, A. N. Grigorenko, K. S. Novoselov, T. J. Booth, T. Stauber, N. M. R. Peres, and A. K. Geim. Fine structure constant defines visual transparency of graphene. *Science*, 320(5881):1308, 2008.

[143] H. Nanto, T. Minami, S. Shooji, and S. Takata. Electrical and optical properties of zinc oxide thin films prepared by rf magnetron sputtering for transparent electrode applications. *Journal of Applied Physics*, 55(4):1029–1034, 1984.

[144] H. Nanto, T. Minami, and S. Takata. Zinc-oxide thin-film ammonia gas sensors with high sensitivity and excellent selectivity. *Journal of Applied Physics*, 60(2):482–484, 1986.

[145] T. Neuberger, B. Schöpf, H. Hofmann, M. Hofmann, and B. von Rechenberg. Superparamagnetic nanoparticles for biomedical applications: Possibilities and limitations of a new drug delivery system. *Journal of Magnetism and Magnetic Materials*, 293(1):483–496, 2005.

[146] K. S. Novoselov, A. K. Geim, S. V. Morozov, D. Jiang, I. V. Grigorieva, M. I. Katsnelson, S. V. Dubonos, and A. A. Firsov. Two-dimensional gas of massless dirac fermions in graphene. *Nature*, 438(7065):197–200, 2005.

[147] K. S. Novoselov, A. K. Geim, S. V. Morozov, D. Jiang, Y. Zhang, S. V. Dubonos, I. V. Grigorieva, and A. A. Firsov. Electric field effect in atomically thin carbon films. *Science*, 306(5696):666–669, 2004.

[148] H. Ogawa, M. Nishikawa, and A. Abe. Hall measurement studies and an electrical conduction model of tin oxide ultrafine particle films. *Journal of Applied Physics*, 53(6):4448–4455, 1982.

[149] S. Okada and A. Oshiyama. Magnetic ordering in hexagonally bonded sheets with first-row elements. *Physics Review Letters*, 87(14):146803, 2001.

[150] A. Ortega, S. Marco, A. Perera, T. Šundic, A. Pardo, and J. Samitier. An intelligent detector based on temperature modulation of a gas sensor with a digital signal processor. *Sensors and Actuators B: Chemical*, 78(1):32–39, 2001.

[151] U. Özgür, Y. I. Alivov, C. Liu, A. Teke, M. A. Reshchikov, S. Doğan, V. Avrutin, S.-J. Cho, and H. Morkoç. A comprehensive review of ZnO materials and devices. *Journal of Applied Physics*, 98(4):041301, 2005.

[152] P. Patnaik. *Handbook of Inorganic Chemicals*. McGraw-Hill, New York, 2003.

[153] H. B. Peng, C. W. Chang, S. Aloni, T. D. Yuzvinsky, and A. Zettl. Microwave electromechanical resonator consisting of clamped carbon nanotubes in an abacus arrangement. *Physical Review B*, 76(3):035405, 2007.

[154] E. M. Purcell. *Electricity and Magnetism*. Cambridge, Cambridge, 1984.

[155] L.-C. Qin, X. Zhao, K. Hirahara, Y. Miyamoto, Y. Ando, and S. Iijima. Materials science: The smallest carbon nanotube. *Nature*, 408(6808):50–50, 2000. 10.1038/35040699.

[156] A. Reina, H. Son, L. Jiao, B. Fan, M. S. Dresselhaus, Z. Liu, and J. Kong. Transferring and identification of single- and few-layer graphene on arbitrary substrates. *Journal of Physical Chemistry C*, 112(46):17741–17744, 2008.

[157] J. T. Robinson, F. K. Perkins, E. S. Snow, Z. Wei, and P. E. Sheehan. Reduced graphene oxide molecular sensors. *Nano letters*, 8(10):3137–3140, 2008.

[158] E. Rossinyol, A. Prim, E. Pellicer, J. Arbiol, F. Hernndez-Ramrez, F. Peir, A. Cornet, J. R. Morante, L. A. Solovyov, B. Tian, T. Bo, and D. Zhao. Synthesis and characterization of chromium-doped mesoporous tungsten oxide for gas sensing applications. *Advanced Functional Materials*, 17(11):1801–1806, 2007.

[159] S. Roy and S. Basu. Improved zinc oxide film for gas sensor applications. *Bulletin of Materials Science*, 25(6):513–515, 2002.

[160] E. K. H. Salje, S. Rehmann, F. Pobell, D. Morris, K. S. Knight, T. Herrmannsdrfer, and M. T. Dove. Crystal structure and paramagnetic behaviour of ϵ-$WO_{(3-x)}$. *Journal of Physics: Condensed Matter*, 9(31):6563, 1997.

[161] J. Sawai, H. Igarashi, A. Hashimoto, T. Kokugan, and M. Shimizu. Effect of particle size and heating temperature of ceramic powders on antibacterial activity of their slurries. *Journal of Chemical Engineering of Japan*, 29(2):251–256, 1996.

[162] F. Schedin, A. K. Geim, S. V. Morozov, E. Hill, P. Blake, M. I. Katsnelson, and K. S. Novoselov. Detection of individual gas molecules adsorbed on graphene. *Nature Materials*, 6(9):652–655, 2007.

[163] G. Schmid. *Nanoparticles: From Theory to Application*. Wiley, Weinheim, 2010.

[164] R. E. I. Schropp and A. Madan. Properties of conductive zinc oxide films for transparent electrode applications prepared by rf magnetron sputtering. *Journal of Applied Physics*, 66(5):2027–2031, 1989.

[165] K. Schwab, E. A. Henriksen, J. M. Worlock, and M. L. Roukes. Measurement of the quantum of thermal conductance. *Nature*, 404(6781):974–977, 2000.

[166] L. Sekaric, M. Zalalutdinov, S. Turner, A. Zehnder, J. Parpia, and H. Craighead. Nanomechanical resonant structures as tunable passive modulators of light. *Appliec Physics Letters*, 80(19):3617–3619, 2002.

[167] S. Semancik, R. E. Cavicchi, M. C. Wheeler, J. E. Tiffany, G. E. Poirier, R. M. Walton, J. S. Suehle, B. Panchapakesan, and D. L. DeVoe. Microhotplate platforms for chemical sensor research. *Sensors and Actuators B: Chemical*, 77(12):579–591, 2001.

[168] S. Sharma and M. Madou. A new approach to gas sensing with nanotechnology. *Philosophical Transactions of the Royal Society A: Mathematical, Physical and Engineering Sciences*, 370(1967):2448–2473, 2012.

[169] M. P. Sharrock and R. E. Bodnar. Magnetic materials for recording: An overview with special emphasis on particles (invited). *Journal of Applied Physics*, 57(8):3919–3924, 1985.

[170] I. Simon, N. Bârsan, M. Bauer, and U. Weimar. Micromachined metal oxide gas sensors: opportunities to improve sensor performance. *Sensors and Actuators B: Chemical*, 73(1):1–26, 2001.

[171] S. Sinha, S. Barjami, G. Iannacchione, A. Schwab, and G. Muench. Off-axis thermal properties of carbon nanotube films. *Journal of Nanoparticle Research*, 7(6):651–657, 2005.

[172] A. Sinitskii, A. A. Fursina, D. V. Kosynkin, A. L. Higginbotham, D. Natelson, and J. M. Tour. Electronic transport in monolayer graphene nanoribbons produced by chemical unzipping of carbon nanotubes. *Applied Physics Letters*, 95(25):253108, 2009.

[173] Y.-W. Son, M. L. Cohen, and S. G. Louie. Energy gaps in graphene nanoribbons. *Physical Review Letters*, 97(21):216803, 2006.

[174] Y.-W. Son, M. L. Cohen, and S. G. Louie. Half-metallic graphene nanoribbons. *Nature*, 444(7117):347–349, 2006.

[175] R. S. Sundaram, C. Gómez-Navarro, K. Balasubramanian, M. Burghard, and K. Kern. Electrochemical modification of graphene. *Advanced Materials*, 20(16):3050–3053, 2008.

[176] J. Tamaki, C. Naruo, Y. Yamamoto, and M. Matsuoka. Sensing properties to dilute chlorine gas of indium oxide based thin film sensors prepared by electron beam evaporation. *Sensors and Actuators B: Chemical*, 83(1):190–194, 2002.

[177] S. Tao, X. Liu, X. Chu, and Y. Shen. Preparation and properties of γ-Fe_2O_3 and Y_2O_3 doped γ-Fe_2O_3 by a solgel process. *Sensors and Actuators B: Chemical*, 61(13):33–38, 1999.

[178] P. Tartaj, M. d. P. Morales, S. Veintemillas-Verdaguer, T. González-Carreo, and C. J. Serna. The preparation of magnetic nanoparticles for applications in biomedicine. *Journal of Physics D: Applied Physics*, 36(13):R182–R197, 2003.

[179] A. S. Teja and P.-Y. Koh. Synthesis, properties, and applications of magnetic iron oxide nanoparticles. *Progress in Crystal Growth and Characterization of Materials*, 55(1-2):22–45, 2009.

[180] A. Tricoli, M. Righettoni, and A. Teleki. Semiconductor gas sensors: Dry synthesis and application. *Angewandte Chemie International Edition*, 49(42):7632–7659, 2010.

[181] Q. Unterreithmeier, E. Weig, and J. Kotthaus. Universal transduction scheme for nanomechanical systems based on dielectric forces. *Nature*, 458(7241):1001–1004, 2009.

[182] P. van der Heide. *X-ray Photoelectron Spectroscopy: An introduction to Principles and Practices*. Wiley, Hoboken, 2011.

[183] G. A. van Ewijk, G. J. Vroege, and A. P. Philipse. Convenient preparation methods for magnetic colloids. *Journal of Magnetism and Magnetic Materials*, 201(1-3):31–33, 1999.

[184] O. K. Varghese, P. D. Kimchambre, D. Gong, K. G. Ong, E. C. Dickey, and C. A. Grimes. Gas sensing characteristics of multi-wall carbon nanotubes. *Sensors and Actuators B: Chemical*, 81(1):32–41, 2001.

[185] Y. L. Vossen. *Phys. Thin Films*, 9:1, 1976.

[186] P. Waggoner and H. Craighead. Micro- and nanomechanical sensors for environmental, chemical, and biological detection. *Lab Chip*, 7(10):1238–1255, 2007.

[187] P. R. Wallace. The band theory of graphite. *Physical Review*, 71(9):622–634, 1947.

[188] A. Walsh, J. L. da Silva, S. H. Wei, C. Körber, A. Klein, L. F. Piper, A. DeMasi, K. E. Smith, G. Panaccione, P. Torelli, D. J. Payne, A. Bourlange, and R. G. Egdell. Nature of the band gap of In_2O_3 revealed by first-principles calculations and x-ray spectroscopy. *Physics Review Letters*, 100(16):167402, 2008.

[189] Q. Wan, Q. Li, Y. Chen, T. Wang, X. He, J. Li, and C. Lin. Fabrication and ethanol sensing characteristics of ZnO nanowire gas sensors. *Applied Physics Letters*, 84(18):3654–3656, 2004.

[190] C. Wang, X. Chu, and M. Wu. Detection of H_2S down to ppb levels at room temperature using sensors based on ZnO nanorods. *Sensors and Actuators B: Chemical*, 113(1):320–323, 2006.

[191] J. Wang, M. Tong, X. Wang, Y. Ma, D. Liu, J. Wu, D. Gao, and G. Du. Preparation of H_2 and LPG gas sensor. *Sensors and Actuators B: Chemical*, 84(23):95–97, 2002.

[192] X. Wang, Q. Li, J. Xie, Z. Jin, J. Wang, Y. Li, K. Jiang, and S. Fan. Fabrication of ultralong and electrically uniform single-walled carbon nanotubes on clean substrates. *Nano Letters*, 9(9):3137–3141, 2009.

[193] Z. L. Wang. Zinc oxide nanostructures: growth, properties and applications. *Journal of Physics: Condensed Matter*, 16(25):R829–R858, 2004.

[194] Z. L. Wang and J. Song. Piezoelectric nanogenerators based on zinc oxide nanowire arrays. *Science*, 312(5771):242–246, 2006.

[195] J. A. Weldon, B. Aleman, A. Sussman, W. Gannett, and A. K. Zettl. Sustained mechanical self-oscillations in carbon nanotubes. *Nano Letters*, 10(5):1728–1733, 2010.

[196] D. D. B. Williams and C. B. Carter. *Transmission Electron Microscopy 4 Vol Set: A Textbook for Materials Science*. Plenum, New York, 1996.

[197] E. W. Wong, P. E. Sheehan, and C. M. Lieber. Nanobeam mechanics: Elasticity, strength, and toughness of nanorods and nanotubes. *Science*, 277(5334):1971–1975, 1997.

[198] Y. Wu, M. Huang, F. Wang, X. M. H. Huang, S. Rosenblatt, L. Huang, H. Yan, S. P. O'Brien, J. Hone, and T. F. Heinz. Determination of the Young's modulus of structurally defined carbon nanotubes. *Nano Letters*, 8(12):4158–4161, 2008.

[199] J. Xu, X. Wang, and J. Shen. Hydrothermal synthesis of In_2O_3 for detecting H_2S in air. *Sensors and Actuators. B, Chemical*, 115(2):642–646, 2006.

[200] J. Yang, C. Lin, Z. Wang, and J. Lin. $In(OH)_3$ and In_2O_3 nanorod bundles and spheres: microemulsion-mediated hydrothermal synthesis and luminescence properties. *Inorganic Chemistry*, 45(22):8973–8979, 2006.

[201] L. Yang, C.-H. Park, Y.-W. Son, M. L. Cohen, and S. G. Louie. Quasiparticle energies and band gaps in graphene nanoribbons. *Physical Review Letters*, 99(18):186801, 2007.

[202] W. Yin, M. Cao, S. Luo, C. Hu, and B. Wei. Controllable synthesis of various In_2O_3 submicron/nanostructures using chemical vapor deposition. *Crystal Growth and Design*, 9(5):2173–2178, 2009.

[203] K. S. Yoo, I. W. Sorensen, and W. S. Glaunsinger. Adhesion, surface morphology, and gas sensing characteristics of thin-gold-film chemical sensors. *Journal of Vacuum Science and Technology A: Vacuum, Surfaces, and Films*, 12(1):192–198, 1994.

[204] T. D. Yuzvinsky, A. M. Fennimore, A. Kis, and A. Zettl. Controlled placement of highly aligned carbon nanotubes for the manufacture of arrays of nanoscale torsional actuators. *Nanotechnology*, 17(2):434–438, 2006.

[205] T. D. Yuzvinsky, W. Mickelson, S. Aloni, G. E. Begtrup, A. Kis, and A. Zettl. Shrinking a carbon nanotube. *Nano Letters*, 6(12):2718–2722, 2006.

[206] T. D. Yuzvinsky, W. Mickelson, S. Aloni, S. L. Konsek, A. M. Fennimore, G. E. Begtrup, A. Kis, B. C. Regan, and A. Zettl. Imaging the life story of nanotube devices. *Applied Physics Letters*, 87(8), 2005.

[207] Y. Zhang, Y.-W. Tan, H. L. Stormer, and P. Kim. Experimental observation of the quantum Hall effect and Berry's phase in graphene. *Nature*, 438(7065):201–204, 2005.

[208] Z. Zhang, Z. Sun, J. Yao, D. V. Kosynkin, and J. M. Tour. Transforming carbon nanotube devices into nanoribbon devices. *Journal of the American Chemical Society*, 131(37):13460–13463, 2009.

[209] Z. Zhang, R. Zou, G. Song, L. Yu, Z. Chen, and J. Hu. Highly aligned SnO_2 nanorods on graphene sheets for gas sensors. *Journal of Materials Chemistry*, 21(43):17360–17365, 2011.

[210] Q. Zhou and L. Lin. Synthesis of graphene using micro chemical vapor deposition. In *Micro Electro Mechanical Systems (MEMS), 2010 IEEE 23rd International Conference on*, pages 43–46, 2010.